6-6-94
E8692

NASA Contractor Report 195300

# A Qualitative and Quantitative Laser-Based Computer-Aided Flow Visualization Method

Victor A. Canacci and M. Jack Braun
*University of Akron*
*Department of Mechanical Engineering*
*Akron, Ohio*

May 1994

Prepared for
Lewis Research Center
Under Cooperative Agreements NCC3–93 and NCC3–165




National Aeronautics and
Space Administration

# A QUALITATIVE AND QUANTITATIVE LASER-BASED COMPUTER-AIDED FLOW VISUALIZATION METHOD

Victor A. Canacci* and M. Jack Braun†
University of Akron
Department of Mechanical Engineering
Akron, Ohio

## ABSTRACT

The experimental approach presented here offers a nonintrusive, qualitative and quantitative evaluation of full field flow patterns applicable in various geometries in a variety of fluids. This Full Flow Field Tracking (FFFT) Particle Image Velocimetry (PIV) technique, by means of particle tracers illuminated by a laser light sheet, offers an alternative to Laser Doppler Velocimetry (LDV), and intrusive systems such as Hot Wire/Film Anemometry. The method makes obtainable the flow patterns, and allows quantitative determination of the velocities, accelerations, and mass flows of an entire flow field. The method uses a computer based digitizing system attached through an imaging board to a low luminosity camera. A customized optical train allows the system to become a long distance microscope (LDM), allowing magnifications of areas of interest ranging up to 100 times.

Presented in addition to the method itself, are studies in which the flow patterns and velocities were observed and evaluated in three distinct geometries, with three different working fluids. The first study involved pressure and flow analysis of a brush seal in oil. The next application involved studying the velocity and flow patterns in a cowl lip cooling passage of an air breathing aircraft engine using water as the working fluid. Finally, the method was extended to a study in air to examine the flows in a staggered pin arrangement located on one side of a branched duct.

*Graduate student, Department of Mechanical Engineering.
†Professor, Department of Mechanical Engineering.

Preceding Page Blank

TABLE OF CONTENTS

Page

LIST OF TABLES.....vii

LIST OF FIGURES.....ix

CHAPTER

I. INTRODUCTION.....1

1.1 Flows Across Brush Seals.....1

1.2 Flows in Cowl Lip Cooling Passages.....2

1.3 Flows Through Staggered Pins in a Branched Duct.....2

II. SURVEY OF PREVIOUS EXPERIMENTAL WORK.....4

2.1 Flow Visualization Methods Using a Light Sheet.....5

2.2 Previous Work Concerning Flat Plates, Cylinders, and Air Foils...13

2.3 Previous Work Concerning Brush Seals.....15

2.4 Previous Work Concerning Cowl Lips.....17

2.5 Previous Work Concerning Staggered Pin Arrays.....18

III. DESCRIPTIONS OF THE EXPERIMENTAL TEST FACILITIES.....22

3.1 The Oil Tunnel For Brush Seal Experiments.....22

3.2 The Water Tunnel For Cowl Lip Experiments.....26

3.3 The Wind Tunnel For Staggered Pin Experiments.....32

3.4 The Laser and Optical Train.....32

3.5 The Tracer Particles.....37

3.6 The Image Acquisition System.....38

IV. COMPUTER PROGRAMS USED FOR IMAGE QUANTIFICATION.....41

4.1 The Computer Program 'FACT'.....41

4.2 The Computer Program 'SNAP'.....43

4.3 The Computer Program 'VADT'.....48

V. RESULTS AND DISCUSSION.....67

5.1 Visualization Studies of Flat Plates, Cylinders, and Airfoils.....67

5.1.1 Visualization of Flow Over a Flat Plate.....67

5.1.2 Visualization of Flow Around a Cylinder.....69

5.1.3 Visualization of Flow Over Airfoils.....72

5.2 Visualization Studies of Flow Through Brush Seals.....77

5.3 Visualization of Flows Through Cowl Lip 180° Cooling Channels....96

5.4 Visualization of Flows Through Staggered Pins in a Branched Duct....115

VI. ERROR ANALYSIS....130

6.1 Introduction....130

6.2 Particle Response Equation....131

6.3 Particle Sizing....136

6.4 Coefficient of Restitution....148

6.5 Operator Introduced Uncertainly Analysis....149

6.6 Statistical Analysis....150

6.7 Total Error in the System....153

6.7.1 Total Error for the Cowl Lip 180° Cooling Passage Experiments....153

6.7.2 Total Error for the Staggered Pin Array Experiments....154

VII. RECOMMENDATIONS FOR FUTURE EXPERIMENTAL WORK..156

7.1 Recommendations for Future Experimental Work....156

7.2 Recommendations for Improvements to the CIIQ System....158

VII. SUMMARY AND CONCLUSIONS.....163

8.1 The FFFT/CIIQ Method.....163

8.2 Applications.....164

REFERENCES.....165

APPENDICES.....172

A. EXAMPLES OF THE FILES CREATED BY THE COMPUTER PROGRAMS.....173

B. TIME CONSTANTS AND RESPONSE TIMES FOR CABOSIL AND LATEX PARTICLES.....180

LIST OF TABLES

Page

Table 6.1: Calculated Diametric Size Distribution for Heated Ethanol-Latex Mixture Droplets (Data Taken February 20, 1991)..... 145

Table 6.2: Calculated Diametric Size Distribution for Heated Ethanol-Latex Mixture Droplets (Data Taken March 1, 1991).....146

Preceding Page Blank

## LIST OF FIGURES

Page

1. Typical Linear Brush Insert Seal Insert....23

2. Oil Tunnel Located at the University of Akron....24

3. Typical Static Pressure Tap Arrangement on Oil Tunnel Side Wall....25

4. Schematic of the Oil Tunnel....27

5. Gravity Fed Water Tunnel Located at NASA Lewis Research Center....28

6. Overhead View of Water Tunnel Test Section....29

7. Typical Inserts Capable of Study in the Water Tunnel....30

8. Schematic of the Water Tunnel....31

9. Vacuum Wind Tunnel at NASA Lewis Research Center....33

10. Schematic of Wind Tunnel....34

11. Close-Up Schematic of Staggered Pin Array Geometry....35

12. Lens System Used to Create Light Sheet....36

13. FFFT Image Acquisition System....39

Page

14. FFFT/CIIQ Operational Flowchart....42

15. Typical Grid Used for Scaling in FACT program....44

16. Input Screen for SNAP Program....45

17. Operational Screen for SNAP Program....46

18. Digitizing Puck and Pad Used to Trace Trajectories....47

19. Digitized Tracings Shown on TV Monitor....49

20. Screen Showing Naming and Storage Menu....50

21. Digitized Tracings Shown on Computer Monitor....51

22. Input Screen for VADT Program....53

23. Selection Describing Curve Fitting Prcedure....54

24. Text Describing Polynomial Curve Fitting Function....55

25. Polynomial Curve Fitting Selection Menu....56

26. Screen Showing Numerical Check of 3rd Order Curve Fit....57

27. Screen Showing Graphical Check of 3rd Order Curve Fit....58

28. VADT Menu # 3....59

29. Screen Showing Digitized (Actual) Flow Trajectories....60

30. Screen Comparing Digitized (Actual) and Fitted Flow Trajectories....61

Page

31. VADT Menu # 5 (Cross Sectional Velocity Menu)....63

32. VADT-Generated X-Direction Velocity Vectors....64

33. VADT-Generated Y-Direction Velocity Vectors....65

34. Geometry of Flat Plate Used in Experiments....68

35. Digitized Flat Plate Velocity Profile....70

36. Vortical Flow Behind a Cylinder in Water....71

37. Stagnation Region of a Cylinder in Water....73

38. Geometries of Airfoils Tested in Water....74

39. Photograph of Flow Over a Clean Airfoil....75

40. Photograph of Flow Over Iced Air Foil....76

41. Mass Flow vs Head Pressure Curve....78

42. Photographic Sequence Illustrating Bristle Motion at Brush Seal Inlet....80

43. Photographic Sequence Illustrating Bristle Motion at Brush Seal Exit....81

44. Digitized Bristle Motion at Conditions A & B (see Figure 41)....82

45. Pressure Profile for Flow Through One Brush Seal....83
(1 mm Diameter Bristles)

46. Pressure Profile for Flow Through Two Brush Seals in Series....84
(1 mm Diameter Bristles)

Page

47. Pressure Profile for Flow Through Three Brush Seals in Series..... 85
(1 mm Diameter Bristles)

48. Pressure Profile for Flow Through Four Brush Seals in Series.....86
(1 mm Diameter Bristles)

49. Pressure Profile for Flow Through One Brush Seal..... 88
(2 mm Diameter Bristles)

50. Pressure Profile for Flow Through Two Brush Seals in Series.....89
(2 mm Diameter Bristles-Leading/1 mm Diameter Bristles-Trailing)

51. Qualitative and Quantitative Flow Assessment in the Inlet Section.....90
of a Brush Seal (2 mm Diameter Bristles) in Oil
A) Map of the Upper Region of the Brush
B) Flow Visualization of Window C
C) Flow Visualization of Window A
D) Quantification of Flow Trajectories in Window D

52. Qualitative and Quantitative Flow Assessment in Window B.....92
(see Figure 51)
A) Flow Visualization at Brush Inlet Adjacent to Upper Wall
B) Flow Trajectories and Velocities Around Inner Bristle 3
C) Flow Trajectories and Velocities of Upstream Free Stream
Entering Spatial Void Between Bristles 2 and 4

53. Visualized Flows at Inlet of Linear Brush Seal in Water.....93
A) Photograph
B) Overlay

54. Visualized Flows at Exit of Linear Brush Seal in Water.....94
A) Photograph of Flow Near Wall
B) Photograph of Exit Lateral Flow
C) Overlay of Flow Near Wall (see Figure 53A)
D) Overlay of Exit Lateral Flow (see Figure 53B)

55. Sketches of Typical Flow Formations Found in Brush Seals.....95

56. Geometry of Flow Path Using Lip # 1.....97

57. Flow Trajectories for Region 1.....98
A) Quantified Flow Trajectories
B) Visualized Flow Trajectories

Page

58. Additional Quantified Flow Trajectories and Velocities for Region 1..... 99

59. Quantified Flow Trajectories and Velocities for Region 2.....101

60. Additional Quantified Flow Trajectories and Velocities for Region 2.....102

61. Photographic Sequence Illustrating Flow Occurring in Region 3.....103

62. Photographic Sequence Illustrating Flow Occurring in Region 4.....104

63. Quantified Flow Trajectories and Velocities for Region 5.....106

64. Quantified Flow Trajectories and Velocities for Region 6.....107

65. Composite Image of Flow Trajectories Around Lip #1 (Regions 1-6).....108

66. Geometry of Flow Path Using Lip #2.....109

67. Composite Image of Flow Trajectories Around Lip #2 (Regions 1-6).....111

68. Quantified Flow Trajectories and Velocities.....112
    A) for Region 2
    B) for Region 5

69. Geometry of Flow Path Using Lip #3.....113

70. Composite Images of Flow Trajectories Around Sharp Edged Lip #3.....114
    A) Visualized Image of Low Flow Rate Around Lip #3 Apex
    B) Visualized Image of High Flow Rate Around Lip #3 Apex
    C) Digitized Flow Trajectories for High Flow Rate (Figure 70B)
    D) Quantified Flow Trajectories and Velocity Around Lip #3 Apex for High Flow Rate (Figure 70B)

71. Typical Internally Cooled Turbine Blade.....116

Page

72. Digitized Flow Trajectories for First Two Rows of the Staggered..... 118
Pin Geometry Using Cabosil as the Seed Particles

73. Quantified Trajectories and Velocities for Flow Around..... 119
Pins 1,3, and 5 Using Cabosil as the Seed Particles

74. Photograph Illustrating Impacting and Rebounding Cabosil Particles..... 121

75. Photograph Illustrating Flow Through the Staggered Pin Geometry..... 122
Using Latex Spheres as the Seed Particles

76. Photographs Illustrating Flow Around the Partition Using Latex..... 123
Spheres as the Seed Particles (note lack of bouncing)

77. Photographic Montage of Flow Through the First Row of the..... 124
Staggered Pin Geometry Using Latex Spheres as the Seed Particles

78. Digitized Flow Trajectories for First Two Rows and Upstream..... 126
of the Staggered Pin Geometry Using Latex Spheres as the Seed Particles

79. Quantified Trajectories and Velocities for Flow Around and Upstream..... 127
of Pins 1,3, and 5 Using Latex Spheres as the Seed Particles

80. Visualization of the Flow Trajectories in the Wake of Pin 5 Using..... 128
Latex Spheres as the Seed Particles

81. Time Response Curves for Seed Particles Entrained in Water..... 134

82. Time Response Curves for Particles Entrained in Air..... 135

83. Time Response Curves for Cabosil Particles Entrained in Air..... 137

84. Time Response Curves for Latex Particles Entrained in Air..... 138

85. Schematic of TSI Aerodynamic Particle Sizing System..... 140

86. Diametric Size Spectrum (Distribution) for Cabosil Particles (APS)..... 141

Page

87. Diametric Size Spectrum (Distribution) for Latex Spheres (APS)..... 142

88. Ethanol-Latex Mixture Droplet Size vs. Distance Graph..... 144

89. Standard Error Estimate (SEE) Curves for a Typical Trajectory..... 151
Polynomial Fit and Respective Velocities (in Water)

90. Standard Error Estimate (SEE) Curves for a Typical Trajectory..... 152
Polynomial Fit and Respective Velocities (in Air)

91. Schematic of Cowl Lip Cooling Passage with Brush Insert..... 157

92. Photograph of a Linear Lucite Brush Seal with a Canopy Top..... 159

93. Photograph of Circular Brush Seal..... 160

Preceding Page Blank

# CHAPTER 1

# INTRODUCTION

A nonintrusive qualitative and quantitative experimental technique has been developed that allows the evaluation of fluid flow patterns, including velocities and accelerations. The technique employs a laser light sheet to illuminate particle tracers entrained in a fluid. A customized lens system functions as a long distance microscope (LDM) making magnification factors of up to 100 possible. Images are captured by a low luminosity camera, recorded on video tape, and processed using a computer algorithm. Files are created that store the particle trajectories, velocities, and accelerations for each local region that is investigated. These results can then be assembled using a commercial CAD package to describe the flow field at a global level. In addition to the description of this Full Flow Field Tracking (FFFT) method, the results of applying the FFFT method to three specific experiments are discussed. These applications are introduced below.

## 1.1 Flows Across Brush Seals

A turbomachine seal is the interface between the fluid power stream and the structure itself. The seal controls both leakage and dynamics which in turn affect engine performance. Current trends toward high performance engines require compliant contacting seals and bearing configurations that accommodate a flexible interface. The labyrinth seal, containing a series of walls, is commonly used in this application. The brush seal, however, has demonstrated that its performance exceeds that of the labyrinth seal. A brush seal can replace a series

of labyrinth seals and provide reduced leakages, a longer life expectancy, reduced maintenance costs, and better response to boundary variations caused by pressure, temperature, or rotation. The FFFT method described above was employed to examine the flow patterns upstream, through, and downstream of several brush configurations in oil. The method allows definition of flow structures within the bristles of the brush at the local level, and across the brush seal at the global level. Additionally, fluid pressure values at locations across the brush are measured as part of a search for efficient brush seal designs.

## 1.2 Flows in Cowl Lip Cooling Passages

Air breathing aircraft engines are subject to high temperatures under high performance operating conditions. Hypersonic aircraft of the future will require cowl lip cooling to combat the high temperature affects that result at the leading edge when traveling at high speeds. The cowl lips must be cooled by either air or recirculated fuel to avoid overheating and the high risk situations of structural failure. The FFFT method was applied to study the flows in some cooling passage configurations designed to facilitate heat transfer in the cowl lips. The method was used to examine the flow of water through rectilinear sections containing rounded or sharp 180 degree turns. The goal of the study was to examine three geometries, determine the flow characteristics of each, and recommend the configuration best suited for cooling based on these flows.

## 1.3 Flows Through Staggered Pins in a Branched Duct

Many analytic codes and procedures are being developed to assist in the design of high temperature engine components. Components such as modern turbo-machinery radial rotors are currently being designed and tested. These advanced radial turbines feature air cooled passages inside the blades to control the blade temperature. Experimental flow visualization and temperature analysis is needed to validate these codes under development. As part of an effort to

establish some of this baseline information, the FFFT method was applied to a geometry similar to those found within one type of internally cooled turbine blades. This geometry was represented by a branched duct containing a staggered pin arrangement on one side. By extending the FFFT method from liquids to air, the flow patterns through the staggered pins and around the partition separating the branches of the duct were determined.

# CHAPTER 2

## SURVEY OF PREVIOUS EXPERIMENTAL METHODS

The use of intrusive methods have been widely used to determine the velocities of internal flows in various configurations. These methods include the use of turbine flow meters [1], where the rotational speed of the turbine is proportional to the velocity of the fluid, and Pitot tubes [1], where the velocity is determined as a function of the dynamic pressure. Other intrusive methods used are hot wire or hot film anemometry [1,2,3]. These heated devices measure fluid velocity at a point in gases and liquids respectively by relating the heat transfer from the sensors to the environment as a function of the power supplied. Although these methods mentioned above are commonly used, all are intrusive and therefore introduce a disturbance into vicinity of the flow that they are measuring.

One method of nonintrusive velocity measurement is Laser Doppler Velocimetry (LDV) [1,4,5], based on the Doppler effect of wave propagation. Laser Doppler Velocimetry involves splitting a laser into two parallel beams focussed to a point, creating a fringe pattern in an ellipsoid shaped volume at the location the velocity is desired. A receiver lens focusses on this volume, and collects the light reflected from the seed particles crossing the fringes. The velocity of the entrained particles passing through that point can be found as a function of this frequency, the half-angle between the two beams, and the wavelength of the laser light. The particles used for these experiments are considered small enough [range of 1-5 microns ($\mu$m)] that their flow velocity accurately represents that of fluid [5]. Although this method can yield accurate velocity measurements, it is limited in that only the velocity of the fluid at a

single point at any given time can be determined. This fact makes the determination of entire flow fields tedious. With these geometric limitations in mind, additional non-intrusive flow measurement methods have been developed.

## 2.1 Flow Visualization Methods Using a Light Sheet

In the past, non-intrusive flow analysis methods using smoke or dyes have been used to visualize flow patterns. The ability of alternative non-intrusive methods to determine accurately the characteristics of flow fields has improved dramatically within the last decade with the arrival of faster and more affordable personal computers and imaging equipment. These improved techniques use light sheets, reflective particles, and computer integrated systems to determine flow patterns, velocities, accelerations, and mass flows. Discussed below are several quantitative methods possessing the ability to determine these flow characteristics. Additional qualitative flow visualization methods, that combine smoke flow visualization techniques with recent advances in optics and imaging technologies, also allow flow visualization patterns to be determined.

Veret [6] used planer laser light sheets to qualitatively study flows in wind tunnels. Using at different times a Continuous Wave (CW) Argon or a YAG laser, the author created sheets of light using a glass rod as a cylindrical lens. The method consisted of seeding the air flow with smoke streams, which upon becoming illuminated revealed separation and stagnation zones, vortex formations, and the onset of turbulence. The author examined flows in the wake of a model delta-wing aircraft, as well as the flows over triangular plates. The position of the light sheet could be moved to allow flow patterns in both parallel and perpendicular planes relative to the flow to be examined. Gennero and Mathe [7] injected steam in the stilling chamber of a wind tunnel and illuminated the test section by a planar laser sheet of light. The authors recorded the images on photographs, and video (VHS) tape. Images from the video tape were loaded into their computer system through an imaging board to software created to perform specific image processing tasks. The final qualitative results exhibiting vortex

edges and flow cores were shown on a computer monitor, and the information was stored in computer memory. Additional operations include a statistical analysis of the results, and allow the calculation of the vortex global velocity to be determined. The system, however, cannot calculate the velocity of the flow within the vortex.

Some flow visualization methods do not use a light sheet, but do nonetheless describe flow patterns by taking advantage of the recent advances in imaging technology. Hiller and Kowalewski [8] discuss using a charge coupled device (CCD) camera to record stroboscopically (shuttering at high frequency) illuminated images of a disintegrating water jet moving at 1.5 m/s. The strobing frequency used was 30 kHz, while the exposure time was 200 nanoseconds (nsecs). The video signal from the camera is stored in an 8-bit image processor having the storage capacity to examine sixteen images simultaneously. The information is loaded to an image processing program that can enhance the images so that more detail can be extracted from each image. The method is limited in its ability to study objects with high velocities, and no true quantitative analysis is possible. Although this system does not employ the use of a light sheet, it does merit mention because of its ability to rapidly record consecutive images using commercial cameras and a strobing device. Garcia and Hesselink [9] utilized cross sectional images of smoke flow visualization to produce a three-dimensional reconstruction of vortical structures present in a gas co-flowing jet. A series of cross sectional images were obtained by seeding the jet with smoke, and placing a laser light sheet at various perpendicular positions to the jet. The images were recorded on movie film, digitized and stored in a computer. A series of image processing operations, including noise filtering and contrast enhancement, allow a perspective view of the jet structure to be constructed. As with the three previous methods, the purpose is qualitative in nature and lends no quantitative results of fluid velocity. The method does exemplify using software to create a full flow field image through the assemby of a series of related images, and is therefore worth describing.

Flow visualization techniques are sometimes used as a part of a larger research effort with other forms of engineering analysis. Safi [10] examined cavity flow both experimentally and numerically. The geometry under investigation consisted of a square cross section cavity with a jet entering at the upper left corner through a thin slit, and a drain of the same size at the lower right corner. Experiments were conducted in water for various Reynolds numbers. The fluid entering the cavity was seeded with aluminum particles, while a thin sheet of laser light, created using a cylindrical lens, illuminated the test section. The author photographed the flow at given time intervals and compared streamlines, generated using a numeric computer code, to these experimental results. Jezek and Reznicek [11] studied the flow of a backward facing step. A laser light sheet was used to illuminate a plane in both air and water, while dyes, polystyrene balls, or hydrogen bubbles were used to visualize the flow. Surface flow visualization on the lateral walls and on the bottom of the channel downstream of the step was done by coating the channel walls with a kerosene and magnesium mixture, and documented by continuous and discrete film records. The authors were able to determine the reattachment location by observing the length of the residual (surface dye) and filmed recirculation regions. The method is effective in determining flow characteristics, but is limited in qualitative applications. Onhari et al. [12] investigated coherent structures in the near-wall region of turbulent channel flow by simultaneously coupling Laser Doppler Velocimetry (LDV) [1,4,5] and flow visualization techniques. The flow visualization was achieved by using fluorescent dye illuminated by a sheet of either laser or halogen light. A digital timing signal was used to synchronize the video taped visualization images, and the LDV signals that were recorded on magnetic tape. The velocities determined by the LDV system were then matched to the respective video image of the flow to form a complete analysis. Although this system can determine flow pattens and velocities, its drawback is the need to operate two synchronized methods of analysis to achieve both visual and quantified results.

Porcar et al. [13] used a light sheet to visualize the flow patterns of a supersonic free jet. Two cylindrical lenses are used to form a small sheet of light. This sheet is improved by periodically oscillating a prism at a specified high

frequency creating a wider sheet of light. A slit located between the prism and the object of interest thins the light sheet to a uniform plane, and a 35mm camera located perpendicular to the sheet is used to record the flow patterns. This slit can be shuttered to create a strobing effect, thus increasing the information recorded by the camera. This shuttering can be varied from a few microseconds to continuous illumination. Falco [14] used a laser volume, formed by intersecting two orthogonal laser planes to represent the motion turbulence near walls of a wind tunnel. The lasers providing the illumination were either an 8 Watt Argon-Ion or a 40 Watt Copper-Vapor laser. An oil fog was created (by mixing 0.5 to 5 micron oil droplets into air) using a smoke generator. Side and plan views could be observed and recorded simultaneously on 35mm film. Although the author could visualize the flow from two normal positions, a three dimensional representation of the flow was not discussed.

Two methods have applied flow visualization techniques to specific aviation and automotive industry needs. Werle [15] studied the flow phenomena of aircraft air intakes by illuminating fine air bubbles in water using a thin light sheet. The author was able to define stream lines and velocity fields of some flows by taking short term exposure photographs. Internal flows of the intakes were studied by illuminating transparent models with sheets of light. Separation patterns were determined for both round and sharp air intake lips at various angles of attack. Additionally, observations of separations were made with a fixed board near the floor of the wind tunnel. For this experiment, a continuous belt moving at the flow velocity was used to eliminate non-realistic flow patterns. Although the method described is limited to low Reynolds numbers, and inlet flow velocity measurements are not discussed, it does provide a better qualitative understanding of inlet flows. Hentschel and Stoffregen [16] have employed laser light sheet techniques for flow visualization in automotive research to optimize air flows around various car bodies to produce lower drag coefficients. In the past, spotlights were used to illuminate trails of smoke to visualize the air flow around vehicles. However this method failed as the streams of smoke widened at the onset of turbulence making individual flow patterns difficult to distinguish. The authors solved this problem by illuminating vaporized crystal oil smoke in either

perpendicular or parallel planes with sheets of laser light. Qualitative still images were recorded with both 35mm film, while high speed movie cameras recorded the motion of the flow.

Adrian [17] reviewed the state of the art in flow visualization and quantification. The author discussed principles, illumination sources, trajectory coding methods, optical recording media, and the accuracy of several methods of multi-point velocimetry. Two multi-point methodologies described are Laser Speckle Velocimetry (LSV) and Particle Image Velocimetry (PIV). While Laser Speckle Velocimetry uses speckle patterns as markers, and PIV uses light reflecting seed particles to define the fluid trajectories, both methods are capable of qualitative and quantitative results. Vysogorets et al. [18] discuss a method using a CCD camera-based method to acquire, and enhance qualitative flow information. An integrated software imaging system, created by the authors, allows the user to directly process a live camera signal through the use of an imaging board. The processed data is stored in a spreadsheet-style fashion making the manipulation of data less tedious. Image processing functions include thresholding, filtering, integration, and intensity scaling. Although the paper is explains the image acquisition system and the ability of the software, it does not include any experimental results. The paper warrants mention however using a personal computer to improve video images acquired for flow characterization.

Methods exist that possess the ability to determine the instantaneous velocity at many points in a flow regime. A PIV double pulsed experimental technique was used by Goss et al. [19] to characterize two dimensional flow fields in a turbine cascade test section. The novel aspect of the experiment resides in the color coding of the particle's initial (green) and final (red) positions, with the green particle image occurring slightly before the red particle image by a predetermined time increment. The illumination occurred by means of two synchronized Nd:Yag lasers and the successive particle positions were recorded on 35mm color film. The analysis consists of separating the green and red images with color filters, digitizing each, and then processing the separated images with customized software. The advantage of this two color method is that it allows the

determination of the the flow direction, sometimes difficult to determine in chaotic flow environments, as well as the flow velocity. Gharib and Willert [20] described a pulsed laser technique which allowed tracking of particles across two consecutive pulses of a light sheet using a Charge Integrating Device (CID) camera. The authors used the CID camera because its variant exposure time could be stepped past the 1/30th of a second exposure time into millisecond ranges. This increased recording step, when coupled with a strobed light source, allowed streaks to be generated that describe the particle motion within one video frame. Although instantaneous velocity values were calculated, the analysis was limited by the fact that the system analyzes only two sequential pulses.

Strobatic devices with patterned pulses are used by some methods to determine the direction of flows. Walter and Chen [21] applied the Particle Image Velocimetry (PIV) technique using a CCD based TV camera to study flows in an offset water channel. The authors created a 1 mm thick sheet of light using a Helium-Neon (He-Ne) laser, and seeded the fluid with Piliolite VTL particles. The authors strobed the laser sheet using an encoded (dot-dash-dot-dot) rotating disk to determine flow direction. A single dot of light represented the beginning, a streak the middle, and double dots the end of trajectories. Flow images were obtained from a CCD camera, stored on a MacIntosh computer, and processed with image enhancing techniques such as filtering. The study resulted in comprehensive flow pattern images which included detailed descriptions of the recirculation regions and points of separation. Khalighi and Lee [22] describe a similar velocity measurement technique that uses a similar directional coding (dot-dot-dash-dot) as the one described above, to study the intake port of a simulated internal combustion engine cylinder. In these experiments, a trajectory trace began with a pair of dots, was followed by a light streak, and concluded with a single dot, allowing the flow direction to be determined in the same manner. The authors recorded the cylinder swirl flows using both CCD and 35mm cameras. The velocity of points on the trajectories was determined by dividing the distance between two dots on the arc by the time step between them. A field of velocity vectors was generated by plotting these velocity values tangent to the midpoint of the light streak. Khalighi [23] improved the system by automating

some of the functions, and continued analyzing swirling flows in the simulated internal combustion engines.

Some methods are able to non-intrusively determine velocity vectors of flow particles in three directions. Chang and Tatterson [24] have developed a computer based automated method for the analysis of complex three dimensional flows in an agitated tank using a stereoscopic technique. A motion picture camera is mounted with a custom Bolex lens [25] system that records a stereo pair of fluid flow scenes. Images are then digitized using a software package that matches the stereo pairs, and identifies, tracks, and evaluates the particles trajectories. Velocities in the X and Y directions can be calculated across a series of up to three frames. An additional photogrammetric analysis of stereo pairs permits the determination of the Z coordinate and therefore the velocity in the third dimension. Doi and Miyake [26] studied the three dimensional characteristics of flow using three CCD cameras to track a single particle traveling in a large glass vessel. A light source was placed behind the flow field to illuminate the 1.0-3.2 mm polystyrene particles used as tracers. Simultaneous images of a particle were observed on three distinct view planes, and transferred to a computer where successive groups of three images were processed into three dimensional trajectories. By tracking consecutive images of a particle over a known time step, velocities and accelerations could be calculated. The limitations of this method are that it can follow only one particle at a time, and that the particle sizes necessary limit the types of flows that can be studied.

Velocity vectors of the same particle can be determined at various points along its trajectory by some methods. Hassin and Blanchat [27] have developed an automated, full field, two dimensional quantitative Digital Pulsed Laser Velocimetry system to study two phase dispersed bubble flows. The authors used a Nd:YAG high energy pulsed laser as the light source, and a novel optical system containing a frequency doubling crystal to create a light sheet. The doubling crystal converts the near infrared 1064 nanometer (nm) wavelength light generated by the YAG laser, to a 532 nm green light to take advantage of the camera's increased sensitivity at lower wavelengths. A high resolution camera

and image processing software were utilized to determine the path of the bubble particles in the flow. The computer algorithm, based on a statistical technique, processes up to ten consecutive images and determines the magnitudes and directions of velocity vectors. The average bubble sizes studied were found to be 258 $\mu$m, with average velocities of approximately 4.74 mm/sec. Schaffer et al. [28] describe the concept of Pulsed Laser Velocimetry (PLV) using photoelectric imaging sensors. The authors discuss the advantages of using photoelectric sensors, such as a CCD camera, as opposed to film-type photochemical sensors. The significant advantages were the ability of these sensors to operate at low light conditions, and the ability to record and view images in real time. Additionally, as the images are recorded digitally, they are suitable for image processing and automated image analysis. The disadvantage of using a photoelectric system, however, lies in the fact that the resolution of the images are not as high. This can be corrected by studying smaller areas at one time, although this too has drawbacks. The authors also discussed the criteria for the selection of the PLV system components, and performed an analysis of the each of these requirements. Components discussed were the image sensing device and its sensitivity, the data storage system, the scattered light collection optics, the laser-based illumination system, and the pulse generator. A pulsed laser velocimetry system using a high magnification optical train (Katoptaron Long Distance Microscope) and a CCD high speed camera was also discussed by the authors.

Methods possessing the ability to determine two dimensional velocities of many particles along the entire trajectory, and throughout the flow field are discussed below. Measurements of two velocity components in turbulent boundary layers were recorded by Cenedese et al. [29] using a PIV system. Multiple images of the flow were illuminated by an argon laser, attached to an appropriate optical train, and recorded with a video camera. The images were stored on a personal computer, and processed by an automated software package. A series of imaging functions such as low pass filtering, and thresholding enhance the images facilitating the ability to determine the velocity components from the tracings. A statistical method guarantees high digitizing accuracy in the tracing process, and the results included compared well to previous experimental results.

Adrian et al. [30] studied turbulent flows in channels using a PIV system. The authors illuminated the channels using a ruby laser and a sheet generating optical system. The flow was seeded with reflective 5-10 $\mu$m particles which allowed the observation of turbulent vortices. A camera mounted normal to the light sheet allowed photographs of the illuminated planes to be taken. The developed photographs were interrogated by image processing software that featured fast Fourier transforms (FFT) to improve the clarity of the images. The software package allowed the determination of the instantaneous velocity at almost any point in the flow.

Braun et al. [31,32] developed a Full Field Flow Tracking (FFFT) technique which used a computer based digitizing system attached through an image grabbing board to a low luminosity television camera. A customized optical train transforms the system into a long distance microscope (LDM) that can magnify up to 100 times flows in gaps as narrow as 0.127 mm (.005 in). The method has been applied to study the flow of oil lubricants in hydrodynamic and hydrostatic bearing configurations. The work details the formation and the development of boundary layers, separation and reattachment zones, and velocity and acceleration magnitudes for the flows between the narrow gaps separating the rotating eccentric cylinders. Additional flows in the pockets of the hydrostatic journal bearings were studied allowing the formation of the entire velocity fields. This thesis extends the FFFT method originated in this work to other environments and applications.

## 2.2 Previous Work Concerning Flat Plates, Cylinders, and Air Foils

Classical subjects of flow visualization experiments have often been simplified geometries that have existing numerical or exact solutions. Flows over geometries including the cylinder, the flat plate, and the airfoil have been studied. Some work in this area using the FFFT has been performed, and is described in Section 5.1. Others have performed experiments using these geometries, and their findings are described in detail below. As early as 1927, Prandtl [33-34] used

smoke streams to visualize the developing flow past a circular cylinder. He continued his work in 1930 by photographing flow past an airfoil [33-34] and as a pioneer of flow visualization by studying steady flow past a circular cylinder, the streamlines of flow past a flat plate, the stages in the growth of the boundary layer behind bluff bodies, and the streamlines past a rotating cylinder [33-34]. In recent years, Kobayashi et al. [35] used a computer with image storing capability to derive the two dimensional velocity distribution around a cylinder in water by digitizing photographs of trace particles. A slit was used to create a thin sheet of light to illuminate 2 mm polystyrene beads, and thus visualize and quantify the flow. The optical system contained two 35mm cameras placed above the test section perpendicular to the flow. The first camera was set with a short exposure time to determine the initial point of a particle streak, while the second was set with a long exposure time to record the length of the streak. The two cameras allow the direction of the trajectory to be determined.

Kimura and Takamori [36] have developed an image processing system that utilizes a correlation technique to obtain the instantaneous velocity vector distribution in a two dimensional flow field. They applied their method to an unsteady flow around a circular cylinder. Using sawdust with an average diameter of 80 $\mu$m as their tracer particles, the authors were able to determine the velocity distribution of most of the flow field. The authors were also able to observe the vortex regions of the flow, their fluctuations, and flow directions. The tracer images were obtained by a TV camera, recorded on VCR tape, and stored in computer memory. A software package processed this image data and calculated the velocity vector values of the flow around the cylinder. Coutanceau and Menard [37] studied two dimensional wakes behind rotating and translating cylinders. The photographic technique described by the authors utilized a camera that accompanies the cylinder in its translational motion. Solid tracers were suspended in an oil and water mixture, and are illuminated by an arc projector as they travel through a thin cross sectional plane. Video images and photographs were taken from perpendicular locations. A commercial image analyzer allowed the determination of stagnation points, centers of vortices, and the measurement of significant velocity profiles. Flow streamlines have also been deduced from the

data recorded by the images. Additional work by Monnet and Coutanceau [38] utilized this method to study the formation and shedding process of the initial vortices induced in the wake of a thin cylinder, and an airfoil subjected to translational motion. Again the camera was mounted to an apparatus tracing the airfoil's motion. For both the air foil and the cylinder, the results were compared favorably to those found numerically.

## 2.3 Previous Work Concerning Brush Seals

As mentioned in the Introduction section of this thesis, the brush seal is an attractive alternative to existing turbomachine seals. Fergusson [39] describes the advantages of brush seals over labyrinth seals (the current industry standard) after performing tests at Rolls-Royce with both types of seals. The author explains that the brush seal has a sealing capacity equal to five to ten labyrinth fins, depending on the flow conditions and the clearance of the seal and the outer structure. Another advantage described is the self compliance ability of the brush seal that allows it to maintain its sealing performance during and after transient radial movements and deflections. Additionally, the author noticed that the brush seal could be used as a bearing chamber seal, and that brush seals could maintain a much higher pressure difference resulting in better sealing, and decreasing the likelihood of bearing system unbalance. According to Flower [40], one circular configuration manufactured by Cross Manufacturing Ltd. has successfully operated for over fifty thousand hours on jet engines in Europe, with 80% of these hours occurring in flight. The author states that additional ground testing is being performed in the United States, and that brush seals are being used extensively in the designs of modern military engines. The author details the manufacturing process of the brush seals, and reaffirms their advantages over labyrinth seals regarding leakage. The ability of the brush seal to effectively continue operating when the system is disturbed, due to the flexibility of the thin bristles comprising the brush, is again discussed, and its advantages in wear and performance over labyrinth seals are documented.

Gorelov et al. [41] examined the effect of geometrical parameters of brush seals on the leakage flow rate of air and compared them with data available from labyrinth seals. The experimental facility allowed testing to occur with shaft speeds of up to 55,000 rpm's, which corresponded to a 200 m/s circumferential velocity at the brush interface region. The authors determined that the brush seals reduced leakages by 5-6 times that of a labyrinth containing eight fins. The authors also learned that the clearance could be doubled and the leakage in the brush seal would still be 3-4 times that of the labyrinth. Additionally, stability tests of the flow characteristics were conducted that found in a 25 hour service period that there was no significant increase in flow rate, that there were no thermal overheat failure problems with the bristles, and that the wear of the shaft was less the 0.06 mm on a shaft surface that had no special coating. Chupp and Nelson [42] replaced labyrinth seals with brush seals in limited-life engines. The authors tested labyrinth and brush seals over a range of subsonic conditions. The authors considered experimental parameters such as bristle length and material, operating temperature, and the number of seals. The authors determined that the brush seal configurations studied reduced leakage by more than three times when compared under similar conditions to the labyrinth seal. The ability of the seal to react to initial wear-in conditions and speed changes were also studied. The brush seals outperformed the labyrinth seals in both of these situations, and although larger leakages were found to occur as the brush was adjusting to its new position, the leakage rate remained significantly less than that of labyrinth seals. It was also concluded that the brush seal can survive dynamic shaft excurions of more than 0.025 inches. This shaft displacement is common for hard landings, while this situation results in a significant wear situation and failure for the labyrinth seal, the brush seal suffers no loss in performance.

Flows through brush configurations can be considered very analogous to flow through a fluid saturated porous medium. Ergun [43], Poulikakos and Kazmierczek [44], Renken [45], and Vafia [46] have all examined flow through porous media while arriving at the same conclusion that flow through these mediums is highly dependent on the permeability and thickness of the porous material. These reports concentrated on the gross flow properties of total mass

flow and total pressure drop. The flow visualization method used by Braun and Canacci et al. [47,48,49,50] on the other hand, allows definition of local flow structures inside the porous matrix (the brush) as well as the global flow representation across the brush. This visualization and quantification was achieved by applying the FFFT method [31,32] described in the previous section. In these papers, the authors studied the effectiveness, as well as the fluid velocities and accompanying flow patterns inside a series of various brush configurations.

## 2.4 Previous Work Concerning Cowl Lips

The leading edge of a hypersonic aircraft in flight encounters high heat flux due to shock interference heating. Aircraft traveling in hypersonic conditions at speeds greatere than Mach 4 could be subject to temperatures of 2000° F or more at the leading edge. These high temperatures cause material and structural failure unless cooled by internal flows, such as recirculated fuel (liquid hydrogen). Studies of flows in various internal passages with different geometries to determine optimal designs continue. In the design of high speed experimental aircraft such as the National Aerospace Plane (NASP), internal cooling was found to be necessary to combat the high leading edge temperatures. Gladden et al. [51] studied numerically three approaches to enhance the cooling of the heated leading edges. The authors studied both the heat transfer and thermal stresses occurring on three models. The impingement pin fin cooled model consists of a series of channels which bring coolant to the leading edge. Jets from these channels impinge the semicylinder of the leading edge and then split and flow in a reverse direction through the pin fins incorporated in both the lower and upper surfaces. The impingement/convection model is similar to the previously discussed model. However, instead of pin fins in the outer channels, these passages are continuous rectangular channels. The coolant path for the convection-cooled model is a continuous loop past the leading edge in the axial direction. Heat transfer in the leading edge is enhanced by the curvature effect on the fluid as it reversed direction around the leading edge. Gladden et al. [52] verified the computational results by comparing the analytical results of the impingement pin fin

configuration with experimental results. The experimental results were obtained by monitoring the temperatures of a leading edge model exposed to high temperature gas exhausted from an oxygen/hydrogen rocket engine, while the nickel test model was cooled with a cryogenic hydrogen coolant that was recirculated through the impingement pin fin configuration. Surface temperatures and heat transfer coefficients determined through experimentation compared well with the analytical results previously documented.

Braun and Canacci et al. [53], used a long distance microscope (LDM) low luminosity television system to study the flow of water in a wide channel with a 180° bend similar to the convection-cooled model discussed above. While this LDM allowed detailed investigations of small regions, an image processing and graphical data reduction algorithm permitted the assemblage of these local regions yielding a composite image of the entire flow field. This Full Flow Field Tracking (FFFT) technique [31,32,47-50] allowed information regarding vortex formations, impingement zones, and flow recirculation regions to be determined. The existence of flow patterns that negatively influence heat transfer (such as recirculating flow) showed that the effectiveness of this geometry was not high enough, leading to additional work being performed in variant cowl lips. This flow analysis is discussed in greater detail in Section 5.2 of this report.

## 2.5 Previous Work Concerning Staggered Pin Arrays

The positioning of bluff bodies in a channel to disrupt the flow from the center to the walls to enhance heat transfer characteristics is commonly found in the designs of heat exchangers, air cooled passages of electronic equipment, and internally cooled turbomachinary. This is usually accomplished by positioning an array of pins, ribs, or tubes in the crossflow. Schaefer and Reamer [54] developed a pulsed laser imaging velocimetry technique to study particle motion in two phase flows. The authors developed an algorithm which analyzes the data, and determines the particle trajectories. The authors applied their light sheet system to visualize the collision of 100 $\mu$m ash particles with heat transfer tubes in a coal

fired boiler. The authors simulated the ash collisions with the tube banks by studying the collisions in air of glass particles on a flat plate at different angles. The authors were able to determine the trajectories of the particles before as well as after impact. These trajectories provide the information necessary to determine the particle velocities, the points of impact, and the angles of incidence and rebound of the impacting particles. The authors also discuss the advantages of the imaging technique over other previously used techniques such as laser Doppler velocimetry and intrusive methods.

Treidler et al. [55] studied the flow past a normal array of staggered ribs in a channel. Although the flow characterization was performed with laser Doppler anemometry, the results of the study are informative due to the similarity in geometry to the staggered pin arrangement studied in this thesis. The authors varied the Reynolds number of the flow, the pitch between the ribs, and the positioning of the ribs in the channel relative to the wall. Two component velocity values were obtained revealing flow patterns for different rib configurations. The study revealed that the flow around the ribs became more unsteady in the configurations in which the ribs were located in the center of the channel, some distance from the wall. These unsteady flow configurations eliminated the stagnant recirculation regions that formed behind ribs mounted on walls, and created shed vortices in the wakes of the ribs located away from the walls. These unsteady flow conditions and shedding process greatly enhance the heat transfer. Several studies contributed information regarding arrays in channel flows. Kawagachi et al. [56] and determined the existence of a critical gap thickness between a cylinder in the channel and the wall where vortex shedding occurs. It was determined that this critical gap between the pins and the wall was 0.3 cylinder diameters. For other objects such as squares and triangles, Kamemoto et al. [57] found this critical gap to be larger. This was due to the fact that separation points on these bluff bodies were fixed, unlike the separation point of a cylinder which can change depending on the flow angularity. Yao et al [58] examined the heat transfer characteristics of staggered arrays of cylinders of various sizes. The authors concurred that the highest heat transfer occurs downstream of the cylinders where shed vortices impinge on channel walls, and

stated that higher heat transfer would be obtained by using smaller cylinders. It has also been discussed by White [59], Chapman [60], and Zhukauskas [61] that staggered arrangements produce more heat flux due to the interaction of wakes on adjacent pins of following rows.

Snyder and Roelke [62] have designed small air cooled radial turbines that utilize internal blade coolant passages containing pin fins to incite turbulent vortices, and spread the flow to the outer sides of the blade to enhance heat transfer. These advances in radial turbine technology have allowed cooled metallic radial turbines to be designed that are capable of withstanding turbine inlet temperatures of 2500° F, without loss of efficiency. The increased inlet turbine temperature and increased cycle pressure ratios result in an increased specific power and improved specific fuel consumption (SFC). The internal coolant flow passages were designed and tailored to simultaneously meet rotor cooling needs, counter coolant pumping effects, and meet geometrical fabrication constraints. The coolant air flow enters from the attach point of the blade (rotating shaft), and exits through the trailing edge into the power stream. The blades can eventually be made of ceramic materials, but that technology is not ready, so air cooled metallic radial turbines will continue to be studied. Recent advances in cooled radial turbine technology were also reviewed, in addition to presenting work performed recently on the design of an air cooled radial turbine. Kumar et al. [63] developed a computer code for calculating the flow characteristics in these passages.

As these are newly developed codes, they require experimental verification to prove that they are indeed viable tools tools for design analysis and prediciton of performance. Braun and Canacci et al. [64] studied the flow trajectories through a staggered pin arrangement on one side of a branched wind tunnel that served as a simplified geometry of a designed cooled turbine blade. The FFFT method described earlier [31,32,47-50,53] was extended from liquids to air in a vacuum tunnel. The method permitted identification and tracking of the same particle, allowing the construction of time dependent trajectories to be made, and the velocities and accelerations to be calculated. The initial results of this study,

and subsequent information determined from further experiments in the wind tunnel are discussed in Section 5.4.

# CHAPTER 3

# DESCRIPTIONS OF THE EXPERIMENTAL TEST FACILITIES

## 3.1 The Oil Tunnel For Brush Seal Experiments

The oil tunnel located at the University of Akron was designed to study the behavior of one or more linear brush seals arranged in series in a pressurized environment. The brushes used in these experiments were fabricated out of lucite, and a typical brush insert is shown in Figure 1. The tunnel (Figure 2) was fabricated out of aluminum and is 1.524 m (5 ft) long with a cross-sectional area of 76.2 mm x 76.2 mm (3 in. x 3 in.) Both upstream and downstream ends of the channel are outfitted with flow straightener sections (see Figure 2) while sloped inserts precede and follow the test section housing the brushes that simulate approaching and sealing dam conditions.

The test section contains two lucite viewing windows located on the top and on one side of the test section. The windows are 25.4 cm (1 ft.) long and 33.3 mm (1.3 in.) thick, and provide illumination and viewing access to the test section. Typically, the light sheet is aligned parallel to the channel and directed through the top window, while a camera views the flow patterns through the side window. This visualization method is discussed in detail below. The side window can be interchanged with another window that contains static pressure taps (Figure 3) to determine the pressure drop across brush systems. Forty-five Ashcroft precision pressure (range of 1-100 psi) transducers were used to determine the pressure values. These transducers are connected to a NEFF data acquisition system allowing instantaneous recording of the pressures.

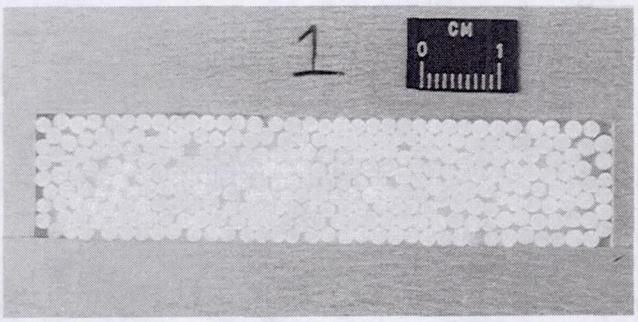



Figure 1: Typical Linear Brush Seal Insert

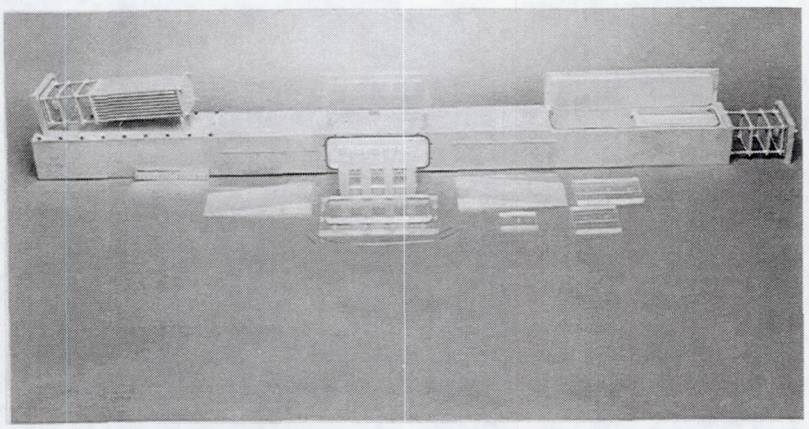


Figure 2: Oil Tunnel Located at the University of Akron

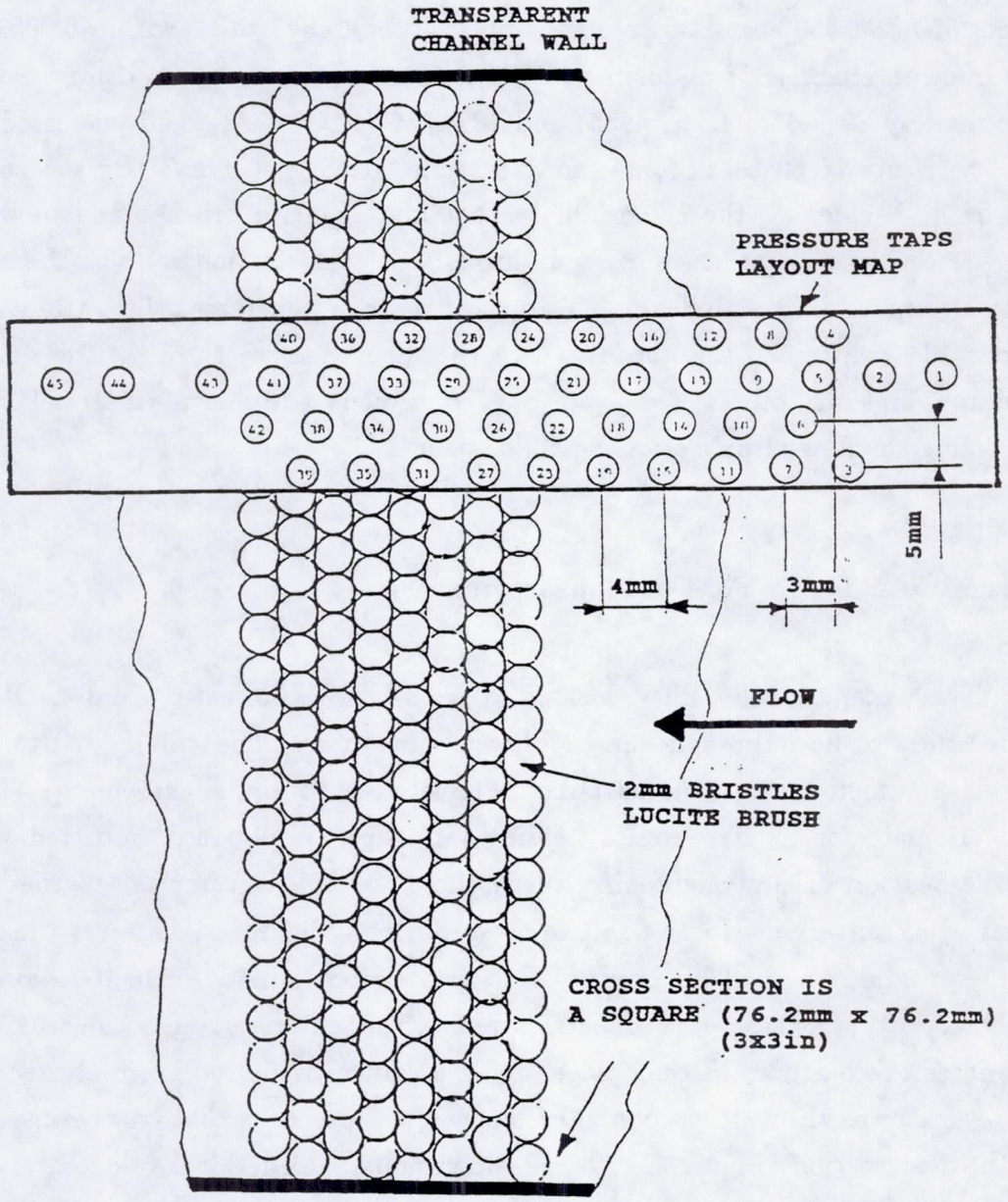



Figure 3: Typical Static Pressure Tap Arrangement on Oil Tunnel Side Wall

The channel is part of a closed loop circuit (Figure 4) containing a variable speed pump that controls the inlet pressure to the brush section as well as the mass flow. Additional components of the circuit include an elevated vertical reservoir, a 10 $\mu$m filter, a 0.5 gpm flowmeter, and an oil pressure gauge. The oil used as the working fluid in the experiments is a mixture of silicone based Dow Corning 550 and 556 cosmetic grade oils optically matched to be within 0.0001 of the refractive index (RI) of lucite (1.4905). The oil mixture was comprised of approximately 82% 550 (RI=1.4965) and 18% 556 (RI=1.4632), and possessed an overall viscosity of 60 centiStokes, and a specific gravity of 0.887. By matching the refractive index of the silicon oil to that of the lucite brushes and viewing windows, the laser light sheet passed through the test section for visualization purposes remains thin and clear. This optical matching increases the visibility of the particles entrained in the flow as the light passes through the lucite boundaries and the oil as if it were one continuous translucent material thus maximizing the flow visualization capabilities.

## 3.2 The Water Tunnel For Cowl Lip Experiments

The water tunnel facility, located at NASA Lewis Research Center, allows for the study of flow through various channels in water. The gravity fed tunnel (Figures 5) functions in a closed circuit activated by a centrifugal pump. The pump circulates the water from a holding tank to a supply tank outfitted with wire meshes for fluid straightening. This holding tank is attached to the test section by a converging duct of square cross section. Figure 6 illustrates the test section containing a cowl lip insert. The test section is made of lucite allowing visual access. For these experiments, a light sheet enters through the side and illuminates the particles in that plane, while a camera mounted normally records the flow patterns through various interchangeable geometries that can be inserted into the test section (Figure 7). Three dimensional translational freedom allows the visualize of flow at many areas of the test section at various magnifications. A schematic of the tunnel (Figure 8) summarizes the circuit.

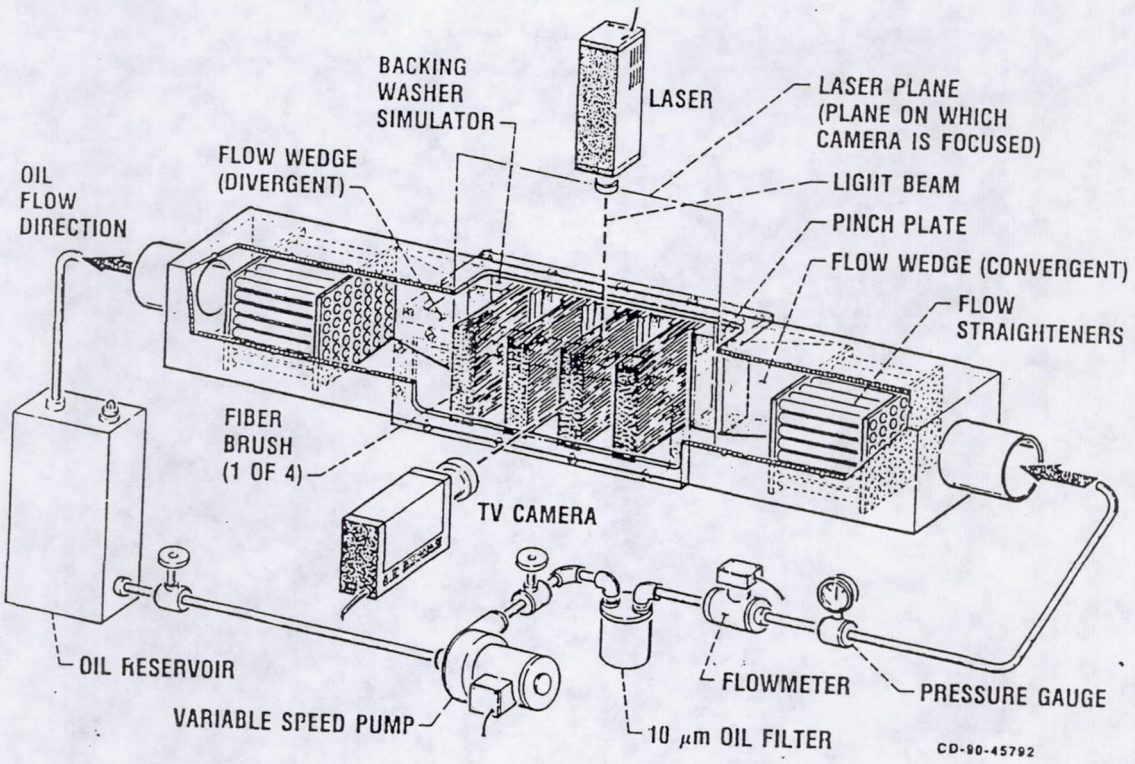



Figure 4: Schematic of the Oil Tunnel

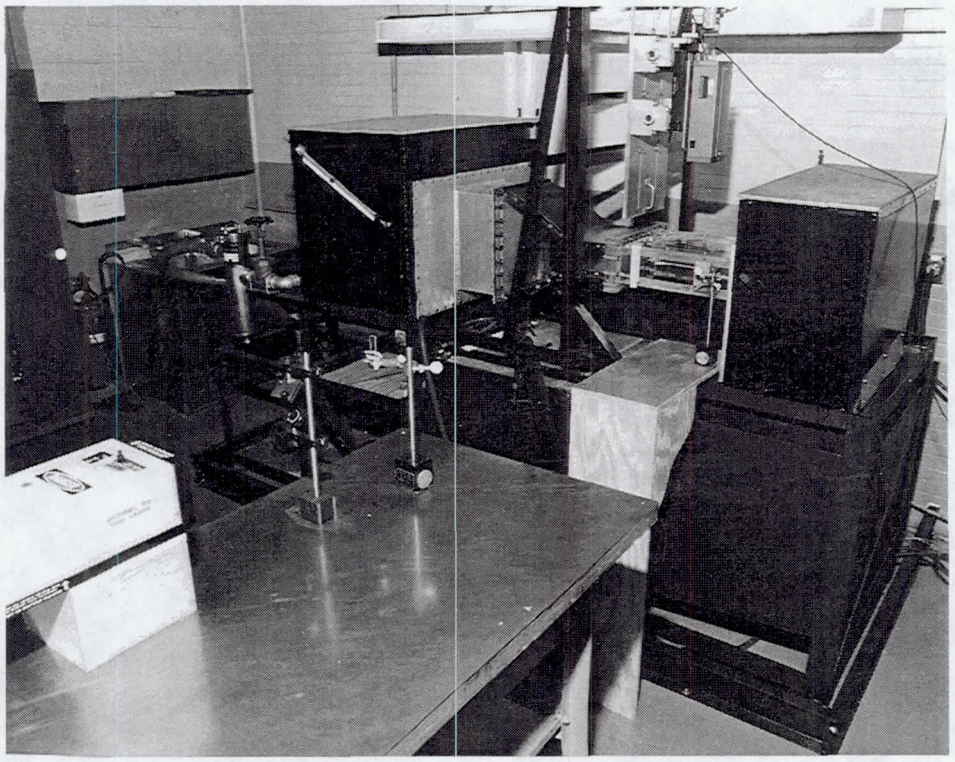


Figure 5: Gravity Fed Water Tunnel Located at NASA Lewis Research Center

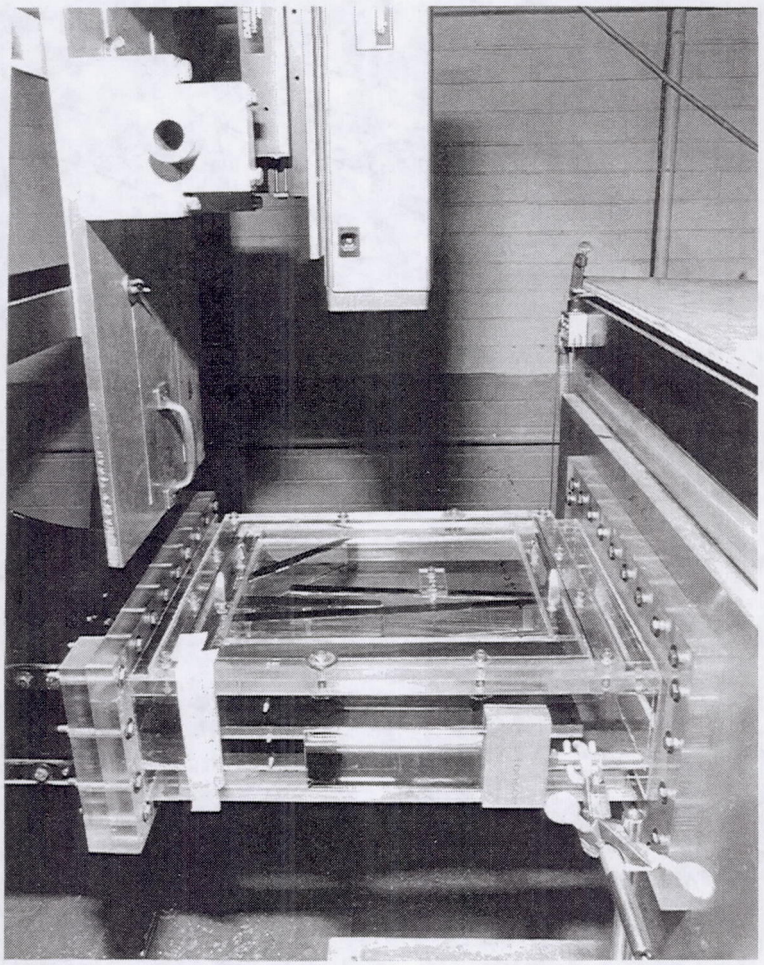


Figure 6: Overhead View of Water Tunnel Test Section

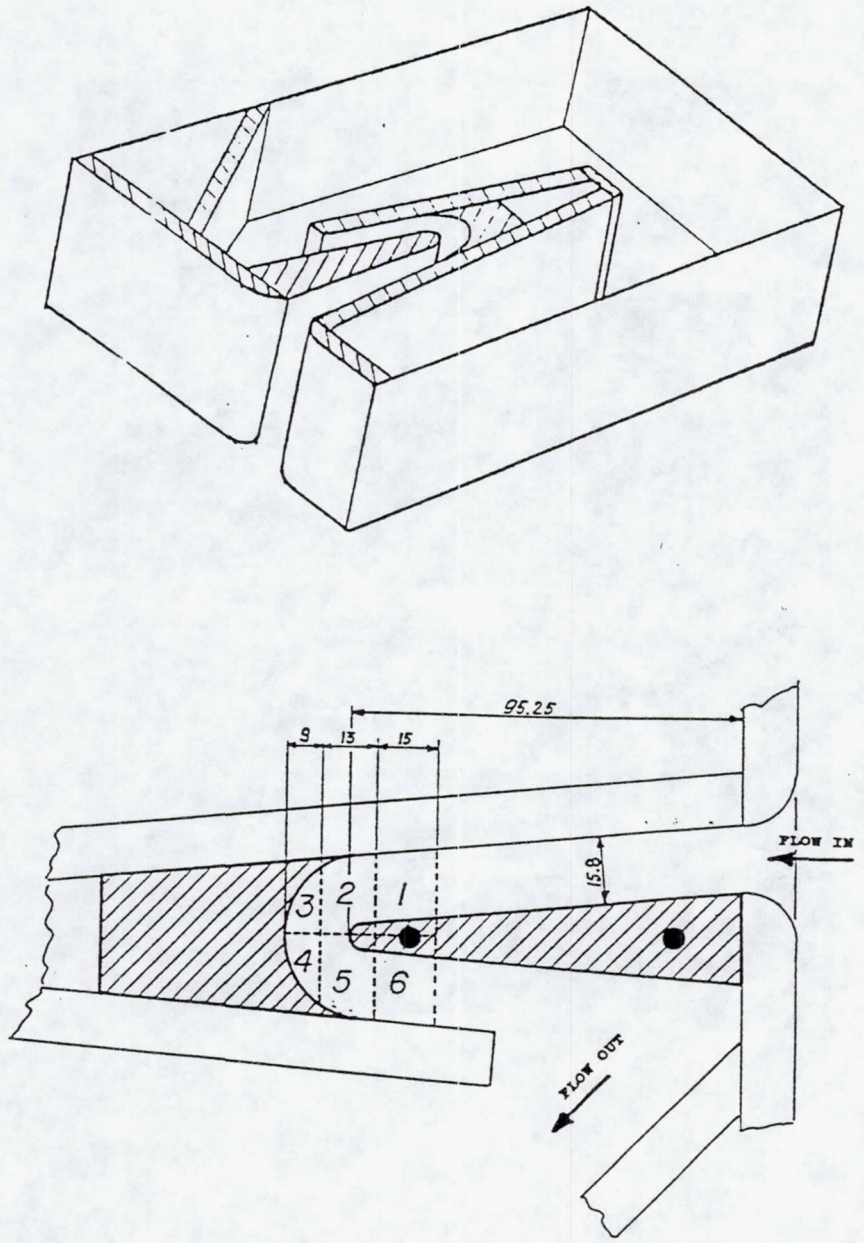



Figure 7: Typical Inserts Capable of Study in the Water Tunnel

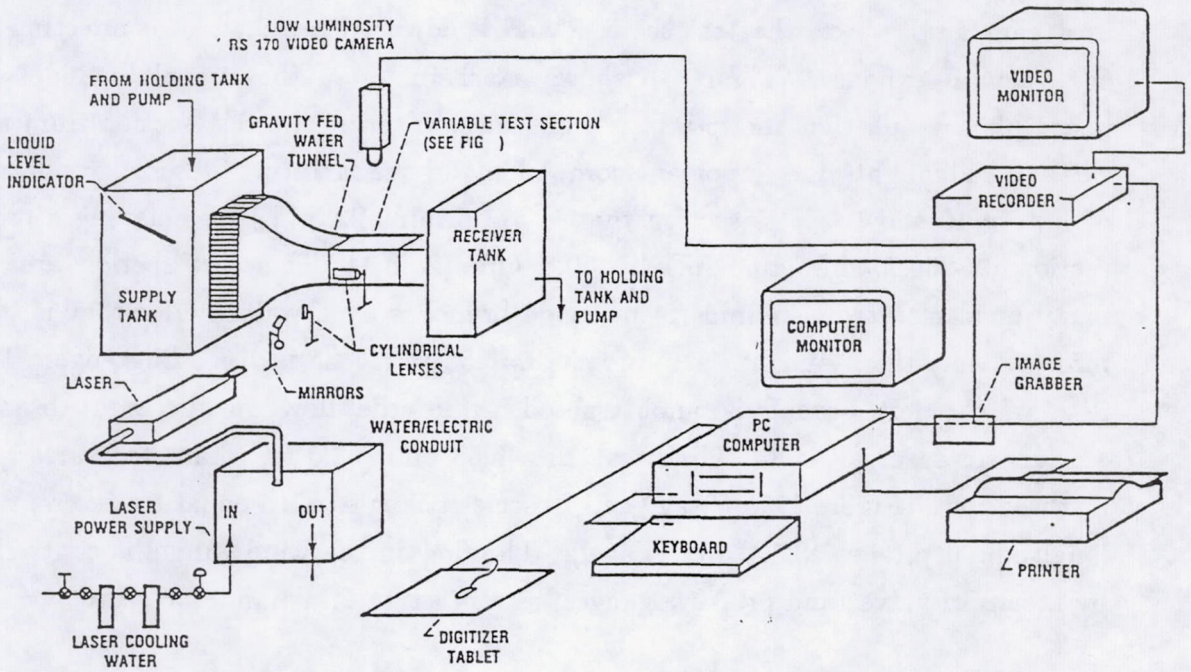



Figure 8: Schematic of the Water Tunnel

## 3.3 The Wind Tunnel For The Staggered Pins Experiments

The experimental test facility, located at the NASA Lewis Research Center, consists of the wind tunnel containing the branched duct staggered pin configuration, the modified low luminosity TV camera, and the laser and optical train that provides the light sheet (Figure 9). The tunnel is connected to a 203 mm (8 in.) diameter vacuum line, and is powered by centralized exhausters that feed multiple test cells. Figure 9 shows (right to left) the inlet bellmouth, the upstream guide duct, the test section, and a downstream channel connecting to the vacuum exhaust. Figure 10 shows a schematic of the tunnel, includes an insert photograph that shows a laser light sheet entering the test section from the side, and highlights the important components of the facility. Closer examination of Figure 10 shows a test section that is 571.5 mm (22.5 in.) long having a cross section of 266.7 mm (10.5 in.) by 50.8 mm (2 in.). This test section area is partitioned into two 127 mm (5 in.) wide branches by a wall divider that is 12.7 mm (0.5 in.) thick and has a rounded [R=6.35 mm (.25 in.)] leading edge. The flow in the left branch is unobstructed, while the flow on the right branch encounters an array of 14 cylindrical pins [9.53 mm (0.25 in.) diameter], arranged in three rows (Figure 11) of staggered isosceles triangles with equal transverse and longitudinal pitches [25.4 mm (1 in.)]. The flow in the wind tunnel is controlled by means of valves and pressure gauges, as a function of dynamic pressure.

## 3.4 The Laser and Optical Train

The 8 Watt, Continuous Wave custom Lexel Model 5500 argon-ion laser provides an intense light source for the flow visualization. A system of controllable mirrors and lenses create a thin sheet of light that is passed through the test section. While the fluid above and below the light sheet remains in the dark, the thin sheet illuminates particles flowing in the light sheet. The coherent beam is directed through an optical system, described in Figure 12, that includes four cylindrical lenses, and micrometrically adjustable mirrors (not shown). The mirrors are used for fine beam adjustment both horizontally and vertically, while

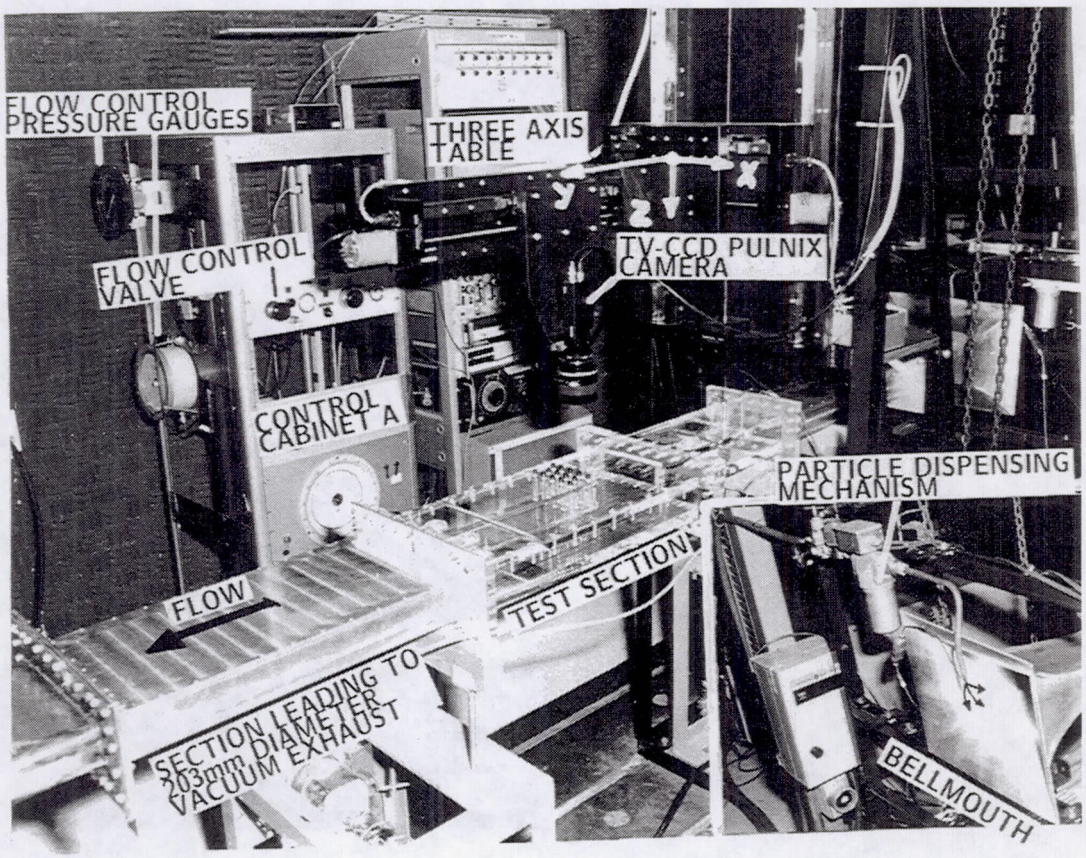



Figure 9: Vacuum Wind Tunnel at NASA Lewis Research Center

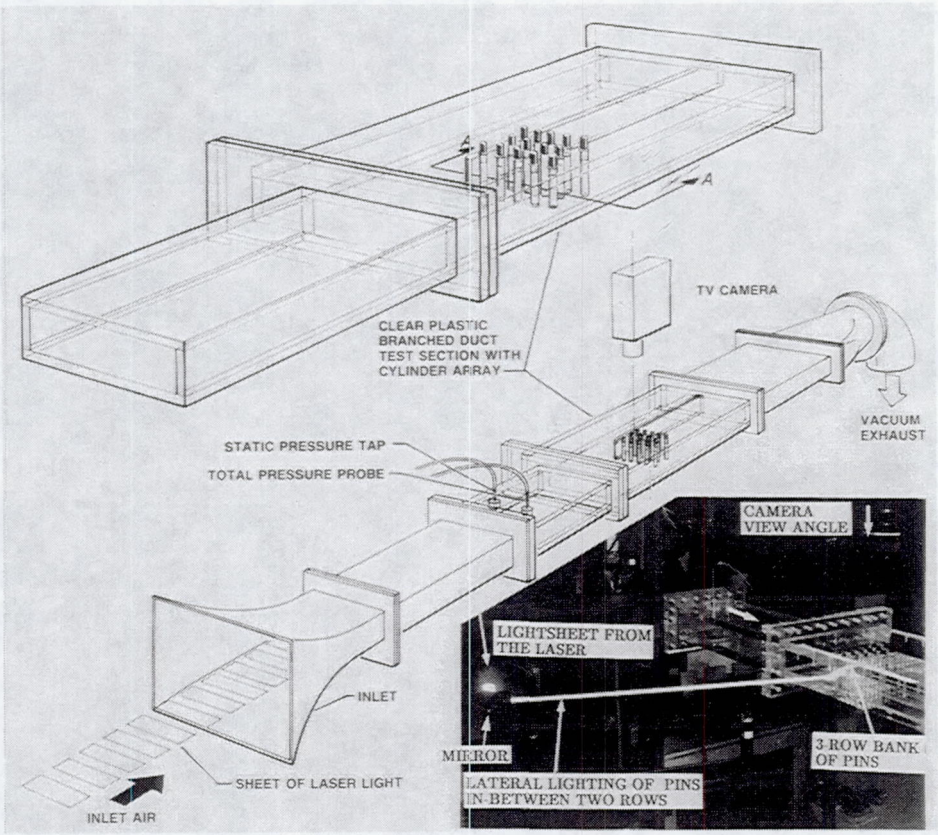



Figure 10: Schematic of Wind Tunnel

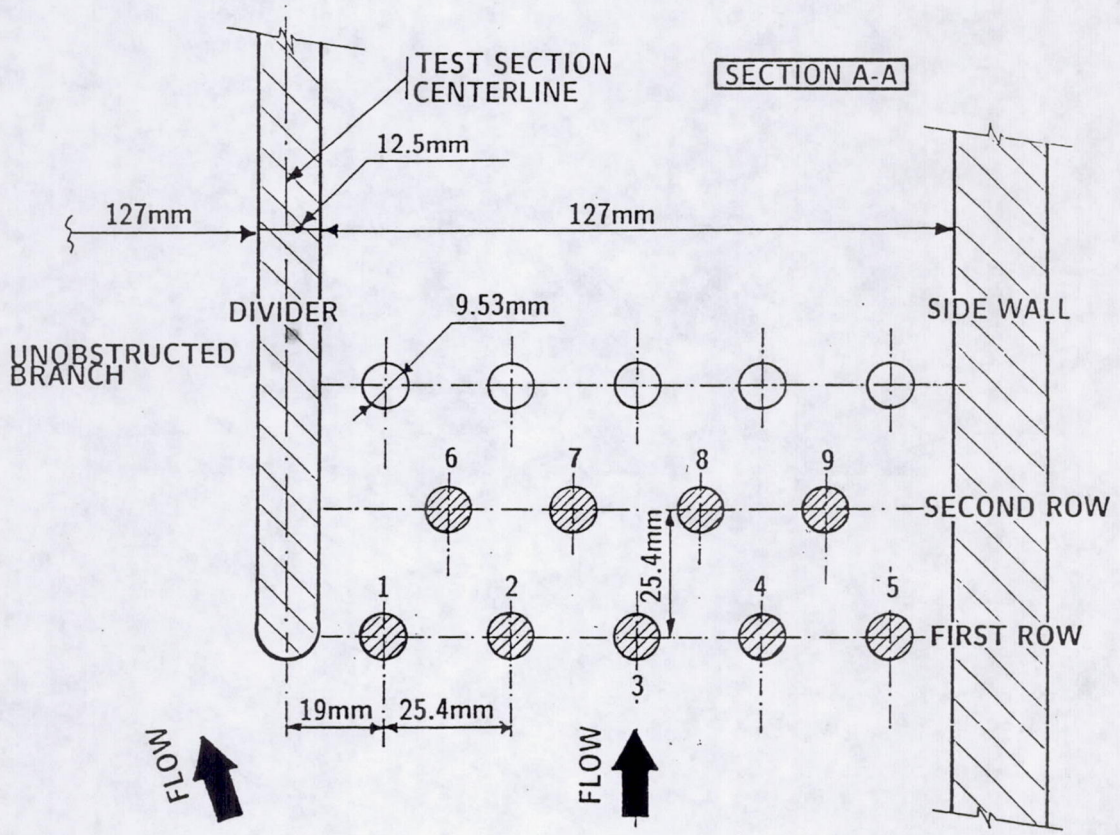



Figure 11: Close-Up Schematic of Staggered Pin Array Geometry

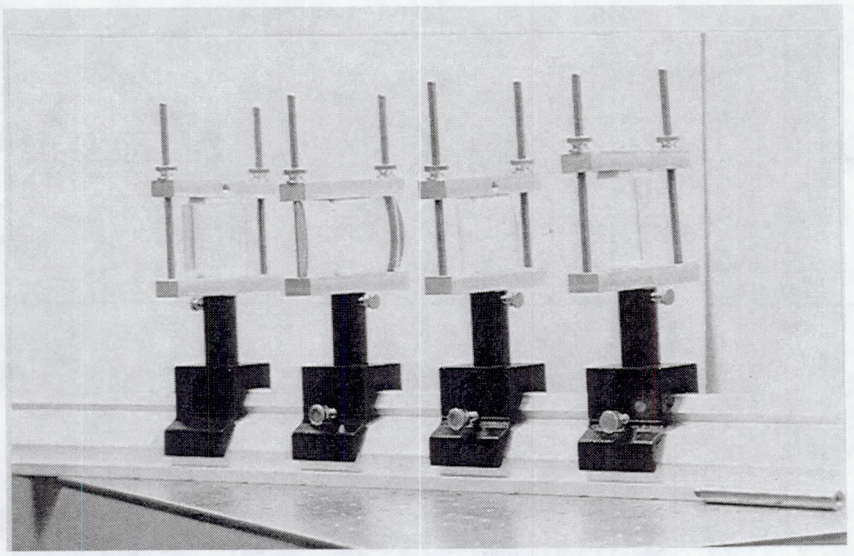


Figure 12: Lens System Used to Create Light Sheet

the lenses are positioned in a specific manner to form the thickness and width of the beam that is desired.

Using the methodology described by Diemunsch and Prenel [65], the cylindrical lens system was designed based on the desired amount of beam expansion, and the focal lengths of the lenses. The resulting lens system transformed the beam into a thin sheet of light, and controlled its collimation, waist length, and width in the test section. The first three cylindrical lenses in the system (see Figure 12) created a light sheet, controlled its thickness, and controlled its width respectively. A fourth cylindrical lens allowed the light sheet of desired thickness and width created by the first three lenses to remain at those conditions (before diverging) for longer lengths of time.

An additional component of the optical system is an electronically controlled stroboscope disk that is inserted between the laser and the first lens. Used in cases where the flow rates are faster, the strobe allows external pulsing of the laser beam at adjustable frequencies. The strobe is necessary because the commercial camera signal (30 Hz) is too slow to capture the higher velocity flows as anything more than one continuous streak across the screen. By choosing the strobing frequency at multiples of 30 Hz, a series of complete luminous imprints of light reflected by the particles crossing the field of view are created. For the experiments performed in this thesis, the strobing frequency ranged from 120 Hz in the water tunnel to 3000 Hz in the wind tunnel depending of the flow rates of the fluids under investigation.

## 3.5 The Tracer Particles

The flow visualization experiments required seeding the fluids with particles that were small enough that when entrained accurately represented the flow, while still being large enough to reflect the light necessary to be seen by the camera. For the experiments involving the oil tunnel, a 10$\mu$m filter was used to limit the size of neutrally buoyant Magnesium Oxide ($MgO_2$) particles passing

through the brush seals placed in the test section. The $MgO_2$ particles were also used in the water tunnel experiments with a $10\mu m$ filter. In both liquids, the particles accurately followed the flow path with no signs of erroneous flows.

The experiments on flow through staggered pins performed in the wind tunnel required a much more involved study to determine the type of seed particles to be used. The first particle used was Cabosil powder which was discharged into the flow by an aeration system. Since images recorded using these tracers showed some particles rebounding off of pins and reentering the free stream (see Section 5.6 and Chapter 6), latex spheres were then used. These spheres are accepted by many LDV researchers as particles that accurately respond to changes in turbulent flows. The latex particles were discharged into the free stream approximately 2.5 meters upstream at the entrance of the wind tunnel (see Figures 9 and 10) in a fluid mixture. The thought was that the fluid would evaporate before reaching the test section, leaving only the latex particles to follow the flow path. The first fluid used to float the latex particles in was water, but this was found to be unacceptable as pockets of water were left on the tunnel floor at the leading edge of many pins. Ethanol, a more volatile fluid that evaporates faster than water, was then used. Initially, it still left some residual pools at the foot of the pins, but this was solved by heating the ethanol-latex mixture to approximately 120° Fahrenheit (F), which increased its evaporation rate. An analysis based on Sheun et. al [70,71] was performed to confirm that the ethanol carrier would be evaporated when the mixture droplets reach the test section, leaving only the latex spheres. This analysis is discussed in more detail in Section 6.3 of Chapter 6.

## 3.6 The Image Acquisition System

The image acquisition system (Figure 13) consists of the TV camera, a Compaq 286 IBM-compatible personal computer, a Panasonic (variable speed playback) video recorder (VCR), and Summagraphics digitizer pad. The low luminosity camera (.3 lux) gated Pulnix TM-740 CCD-TV camera offers a CCD

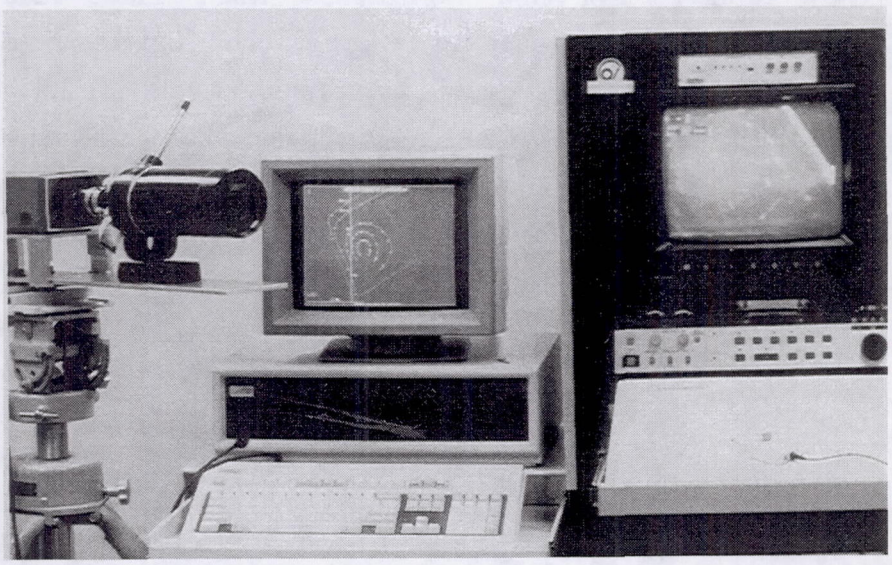


Figure 13: FFFT Image Acquisition System

array with a resolution of 756 (Horizontal) by 581 (Vertical) pixels (11 micrometers). The camera had three degrees of translational freedom for all of the experiments. For the experiments in the wind tunnel, a three-axis XYZ table controlled by stepping motors and manipulated by joysticks provided simple relocation of the camera. The front end of the TV camera is made up of a series of interchangeable extension rings attached to either an 85 mm Nikor lens, used in the water and wind tunnel experiments, or a Questar Q100 high magnification lens used for the brush seal studies in the oil tunnel. This video camera system functions as a long distance microscope (LDM), whose magnification was controlled by the insertion or removal of extension rings. These video images are interfaced to the computer through an Imaging Technology imaging board to a custom software package, first used by Braun et al. [31-32], capable of manipulating these images. This system is capable of storing images either on video tape, or directly into the computer memory for later offline processing. The operational procedure and the features of this package are described thoroughly in the next chapter.

# CHAPTER 4

# COMPUTER PROGRAMS USED FOR IMAGE QUANTIFICATION

A Computer Integrated Image Quantification (CIIQ) method provides a vehicle to transfer raw video images into descriptive information regarding the flow field. This menu driven mathematical and graphics package allows rapid quantification of qualitative images providing Full Flow Field Tracking (FFFT) of particle trajectories. A flowchart (Figure 14) describes the process that begins with the positioning of a video tape at a frame of interest by utilizing the pause or freeze frame feature of the VCR. and determining the magnification of the recorded images in a program referred to as FACT. Recorded images are then digitized into trajectory traces, and stored in computer memory as coordinates in the program SNAP. These files are then processed through a curve fitting algorithm, and the velocities and accelerations are determined by the program VADT. A CAD package can assemble these files into a complete description of the entire flow path. The computer programs, and the method of operation of the CIIQ system are described below.

## 4.1 The Computer Program 'FACT'

The initial stage in the operation of the computer programs is to determine the magnification factor of the recorded images. This scaling is accomplished by running the program **FACT**. During the experiments, a portion of millimetric graph paper is recorded by placing it on the outside of the test section and focussing on it. Once the focus is established, the controls of the lens themselves will not be modified for the rest of the experiment. By fixing the focus of the

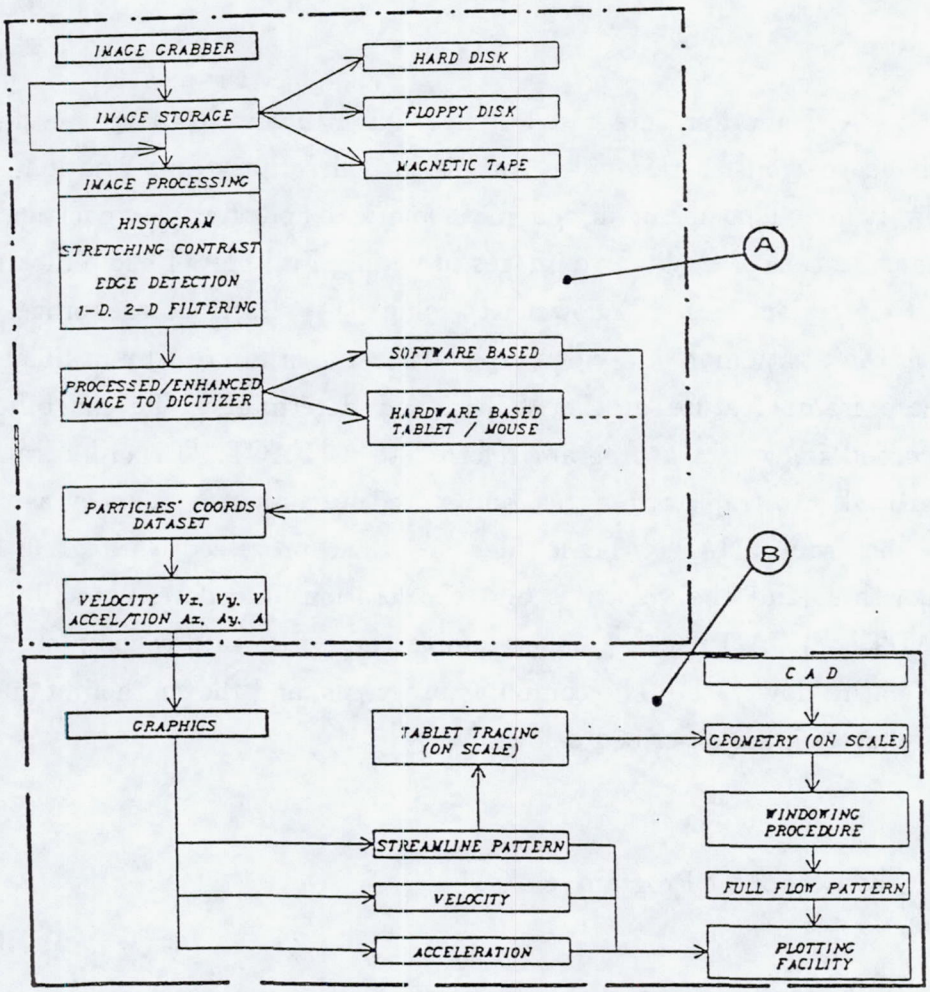


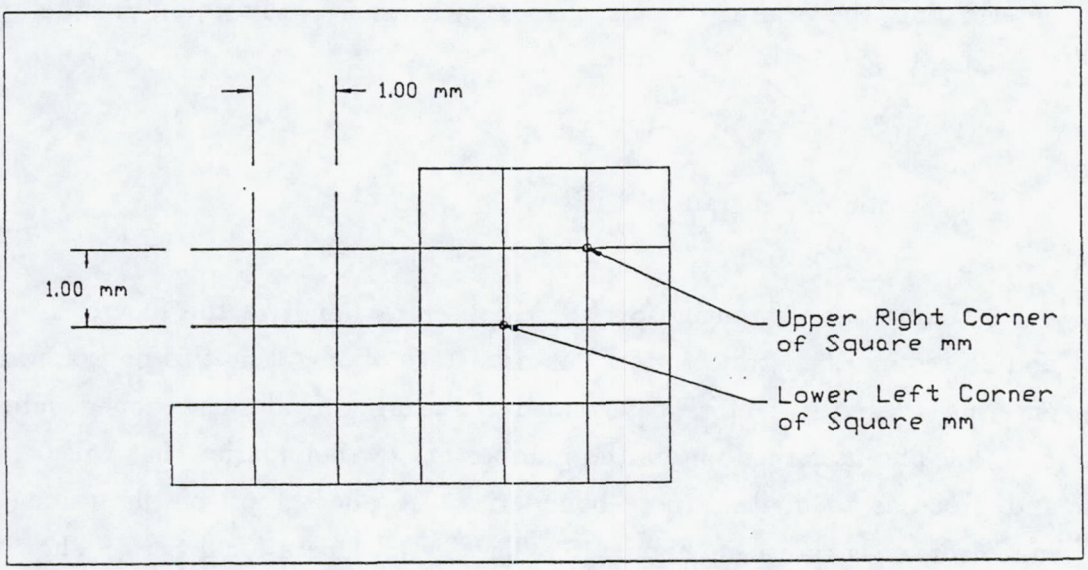

Figure 14: FFFT/CIIQ Operational Flowchart

lens, the distance between the camera and plane of interest is kept constant. Since the desired and illuminated plane of study is inside the test section, the entire camera system is moved closer until flow particles in that plane are brought into focus. This process insures that the graph paper and the images are viewed at the same magnifications. The corners of a square centimeter are then digitized, and FACT calculates the X and Y (2-D) direction scaling factors in units of pixels/mm. A typical grid used for scaling is shown in Figure 15. This process is repeated 5-10 times to assure the accuracy of the scaling factors. After determining the scaling factors, the user is then ready to begin the particle digitizing process.

## 4.2 The Computer Program 'SNAP'

Using the subroutine **SNAP**, the user can digitize the particles positions and determine their trajectories. The first stage of operating this program involves entering the scale factors determined by using the aforementioned subroutine FACT. The user then enters the number of flow boundaries that will be traced, and proceeds to digitize these boundaries. A photograph of the scaling factor input screen is shown in Figure 16. The SNAP Operational Screen showing the functions available to the user is shown in Figure 17. After the boundaries have been digitized, the user begins to trace the particles and their trajectories.

In the case in which the flow is not very fast, the particles' motion is recorded on consecutive frames of video tape, without the use of a strobing device. Utilizing the function of the VCR that allows frame by frame viewing of the recorded tape, the tracing particles are located and the position of each particle of interest is marked on the TV screen by means of a digitizing table and puck (Figure 18). This is repeated for all the sequential frames in which the particles can be followed along well defined planar trajectories. This process can be repeated for many particles, across several frames, until the flow field is mapped.




Fgure 15: Typical Grid Used for Scaling in FACT Program

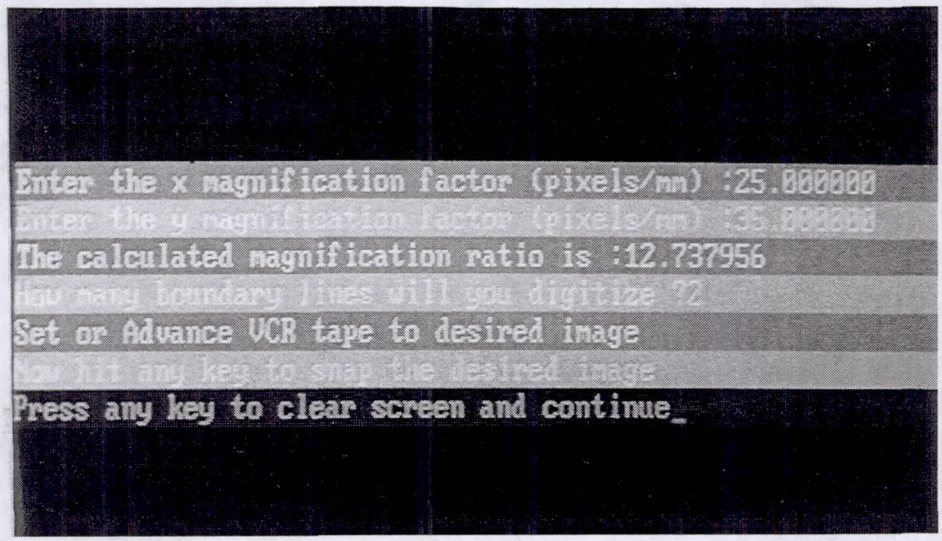



Figure 16: Input Screen for SNAP Program

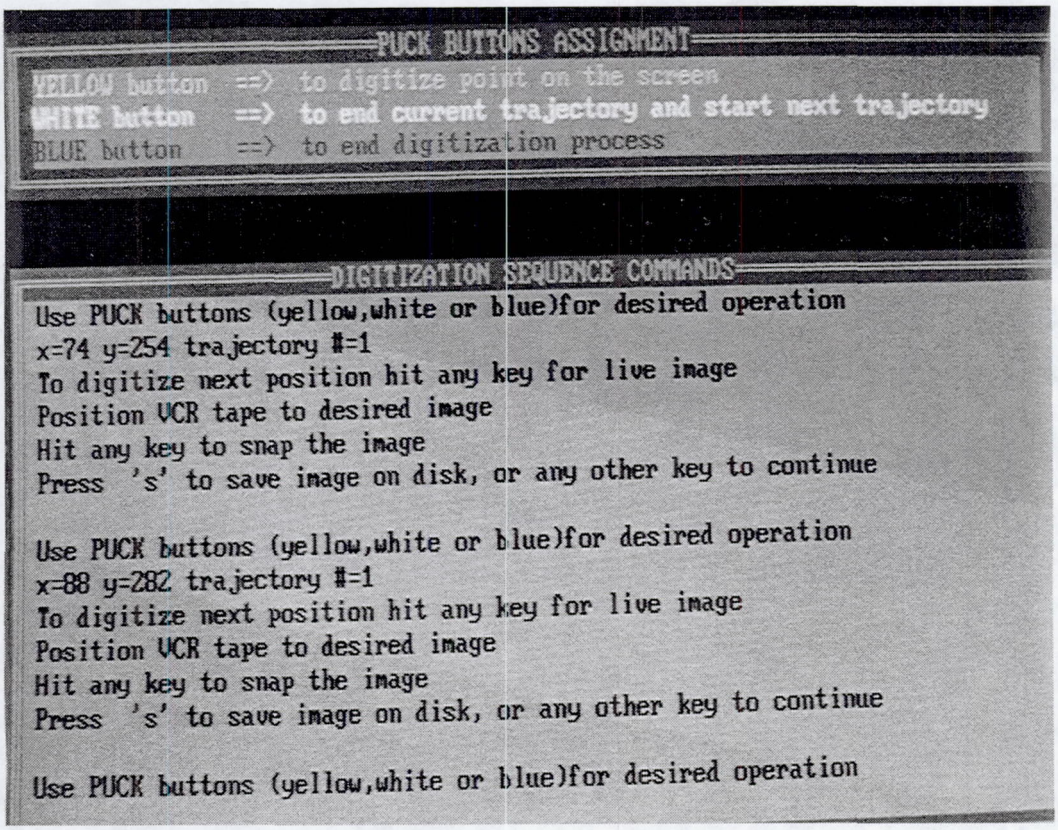



Figure 17: Operational Screen for SNAP Program

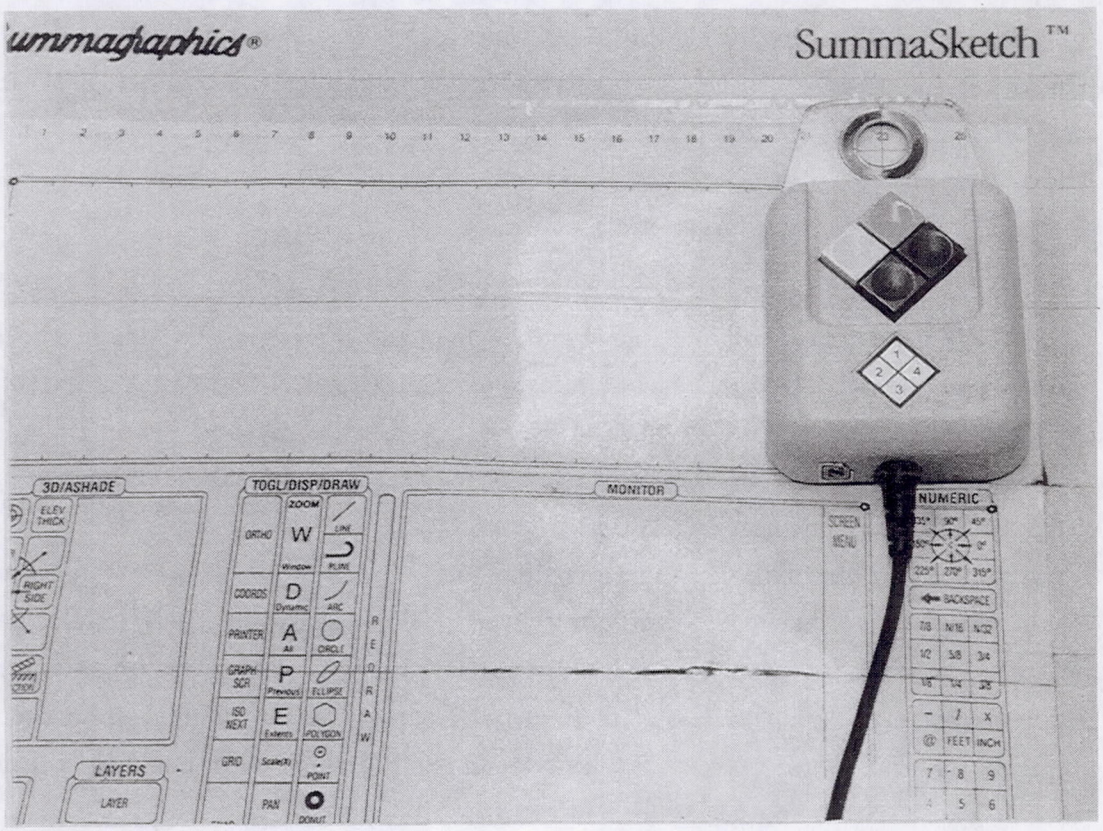



Figure 18: Digitizing Puck and Pad Used to Trace Trajectories

Each trajectory set of digitized points are marked by a flag (trajectory identification number) assigned by the program during the digitization process. The digitization traces appear on the TV monitor (Figure 19), and when the user is satisfied with the number of trajectories that have been digitized, he gives a name to this data set, and exits the program. This name, the coordinates and the trajectory number of each digitized point are stored in automatically created, and mnemonically labeled files. The program creates two files providing the extensions **.bnd** for the file containing the locations of the boundaries, and **.tra** for the other file that contains the positions of the particle trajectories. Both have the same root name selected by the user, and the screen that accepts and assigns the name to the appropriate files is shown in Figure 20. Additional hidden files for use by the program VADT are also created at this time.

When the flow rate is increased, it becomes necessary to strobe the light source to a specific frequency that allows several chops of the same trajectory to be captured within the same viewing frame. If the first method were utilized, the particle would appear in the viewing area as one long streak of reflected light. The strobing device, however, divides this streak into contiguous 'chops' of light that appear on the same frame thus increasing the number of points making up each trajectory. These chops are contiguous positions of the same particle, and as the time interval of the strobing is known (the inverse of the strobing frequency) one can more accurately follow its flow path across the flow field. The user can digitize as many trajectories as desired on each frame, and has the ability to search additional frames for more information. The program creates a graphical representation of the digitized trajectories and boundaries on the computer monitor (Figure 21), and offers the option of printing a hardcopy. The naming of the files occurs in the same manner (see Figure 20) described above.

## 4.3 The Computer Program 'VADT'

After a sufficient number of trajectories have been digitized, the user can begin the quantitative processing of the data by running the program **VADT**.

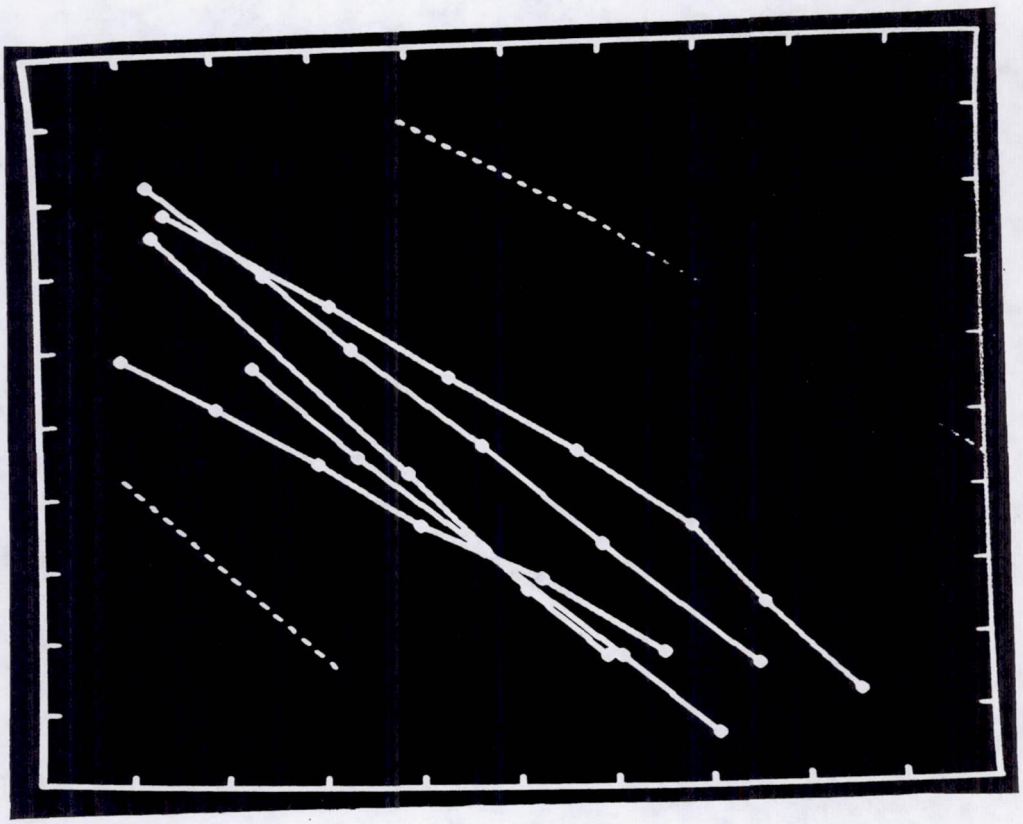


Figure 19: Digitized Tracings Shown on TV Monitor

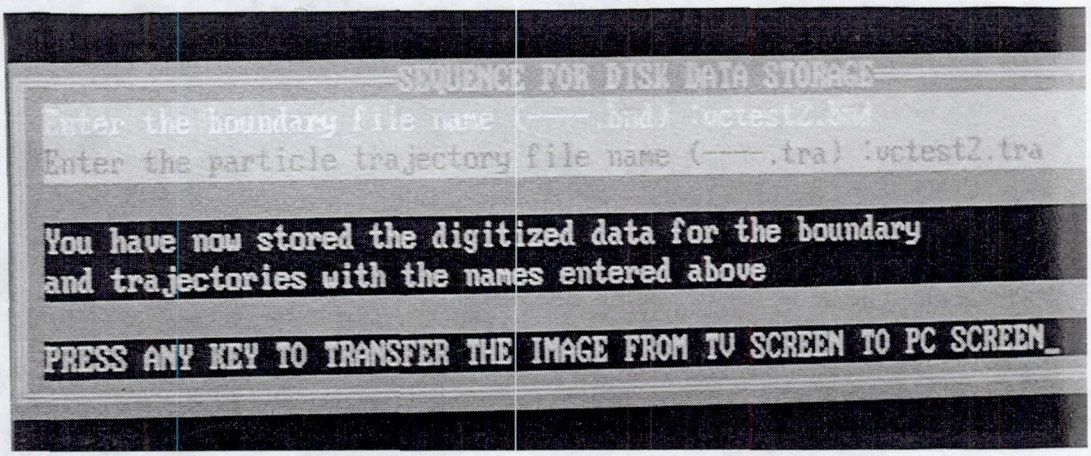



Figure 20: Screen Showing Naming and Storage Menu

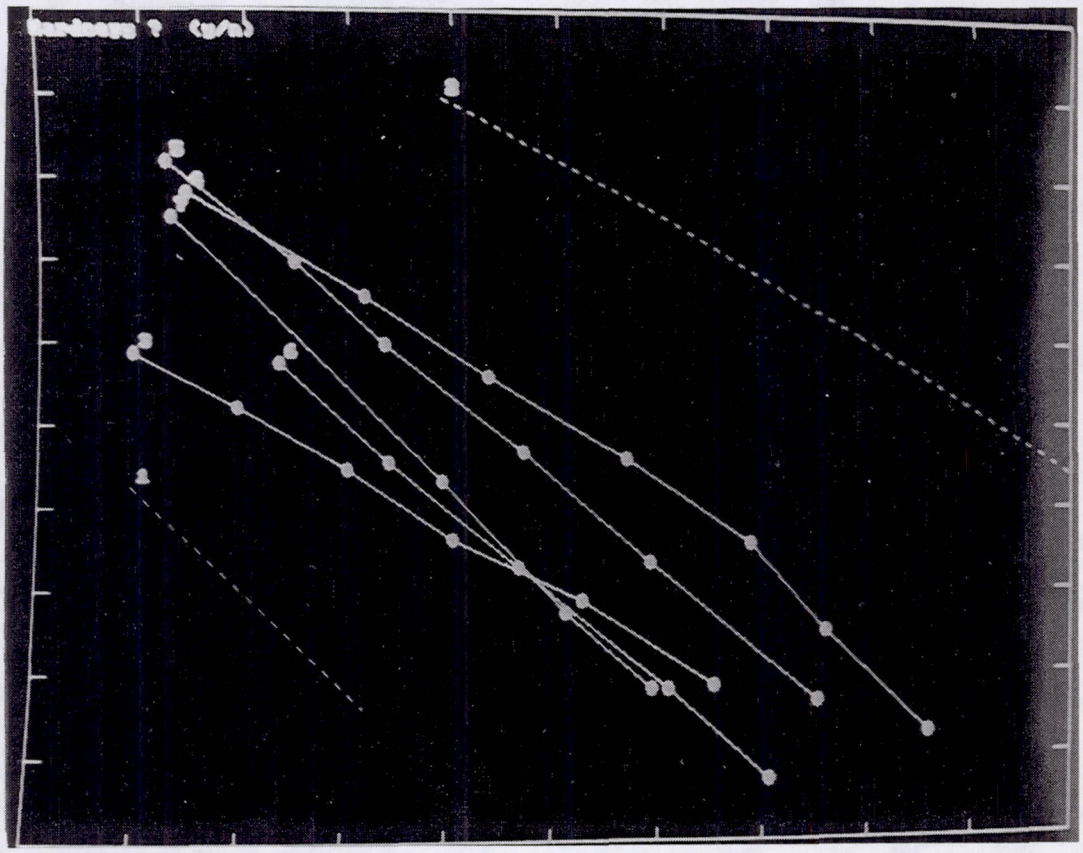


Figure 21: Digitized Tracings Shown on Computer Monitor

This program gets its name from its ability to derive the velocity and acceleration vectors from flow images recorded at various time steps. The user begins this program by first inputting the name of the data file that he wishes to process, the associated scale factors, and the appropriate time interval DT. The time interval [the VCR recording speed (1/30 sec), or the reciprocal of the strobing frequency] allows the computer program to determine the time interval between digitized points. This information input screen is shown in Figure 22. The program then proceeds to parametrically fit the flow trajectories (Equations 1 and 2),

$$x(t) = A_o + \sum_{i=1}^{i=1} A_i t^i \quad (n=1...9) \tag{1}$$

$$y(t) = B_o + \sum_{i=1}^{i=1} A_i t^i \quad (n=1...9) \tag{2}$$

and the user can choose from polynomials ranging from first to ninth order, as a function of the number of points and the best fit. Two helpful and descriptive screens are shown in Figures 23 and 24, while the input screen itself is shown in Figure 25.

For each polynomial, the computer program determines the accuracy of the fit by comparing each fitted point with each actual point, and determining and listing the percent error between the two points (Figure 26). The arbitrary trajectory shown was fit to a third order polynomial in the figure, and the percentage errors varied from 0.03% to 2.58%, which are very typical numbers. The user can also determine graphically the accuracy of the fit (Figure 27) by comparing the fitted curve with the actual digitized points making sure that it passes through them accurately representing the flow path. The user has the option to choose several fits before deciding which one is most representative. Many other functions can be selected from the menu shown in Figure 28, such as graphically describing the actual flow trajectories, the digitized flow trajectories, and the comparison between the two. Shown in Figures 29 and 30 respectively

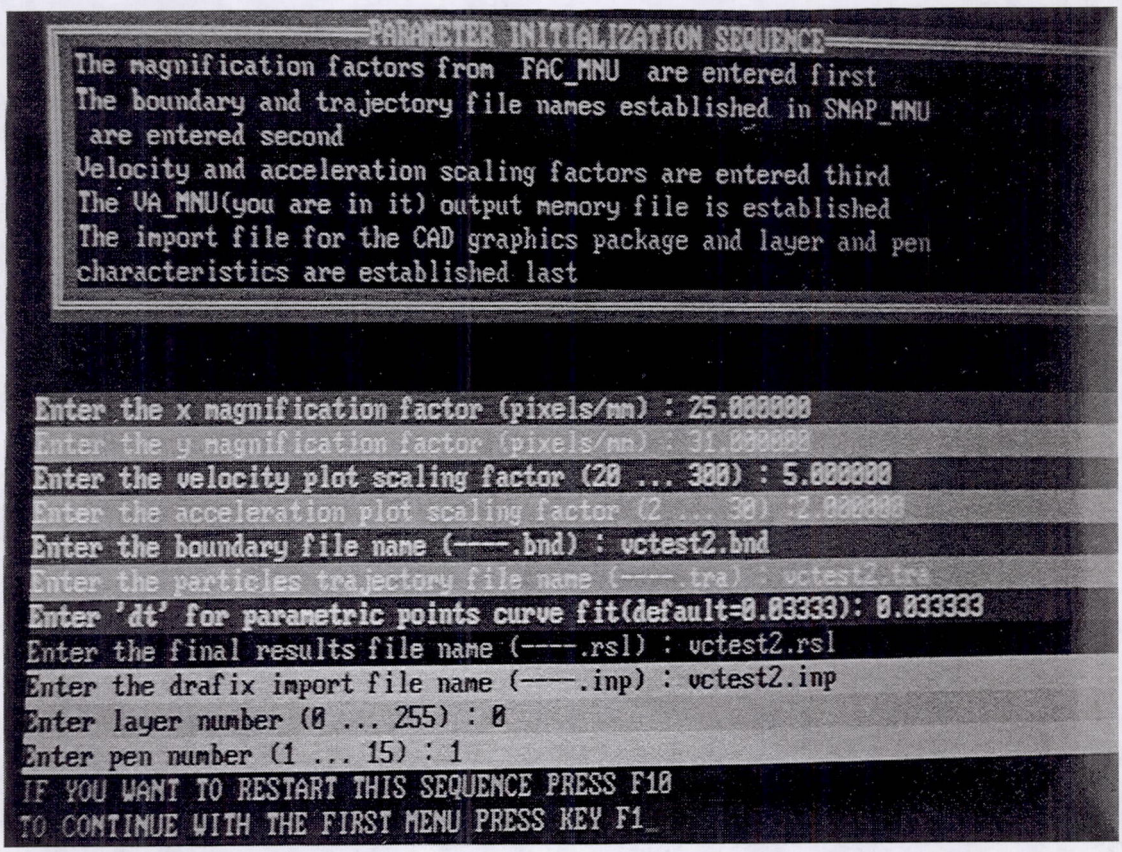



Figure 22: Input Screen for VADT Program

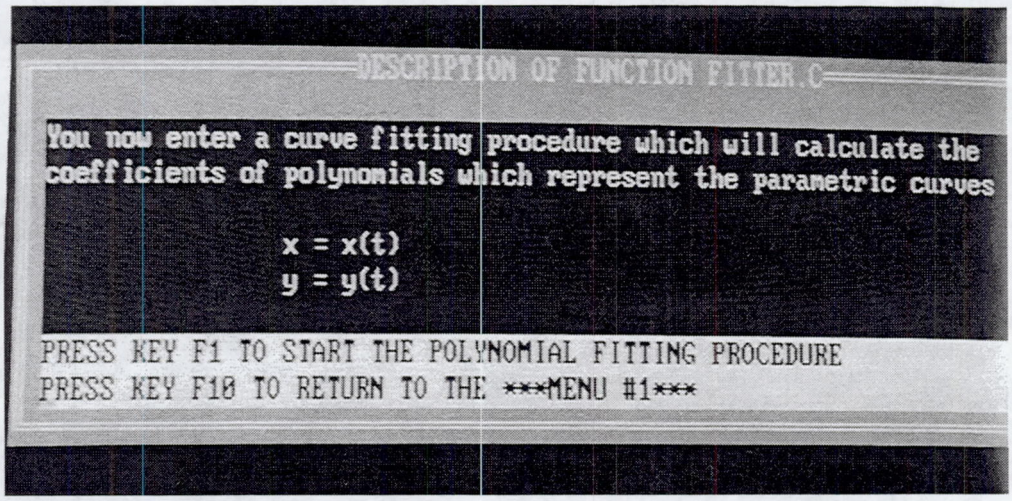



Figure 23: Screen Describing Curve Fitting Procedure

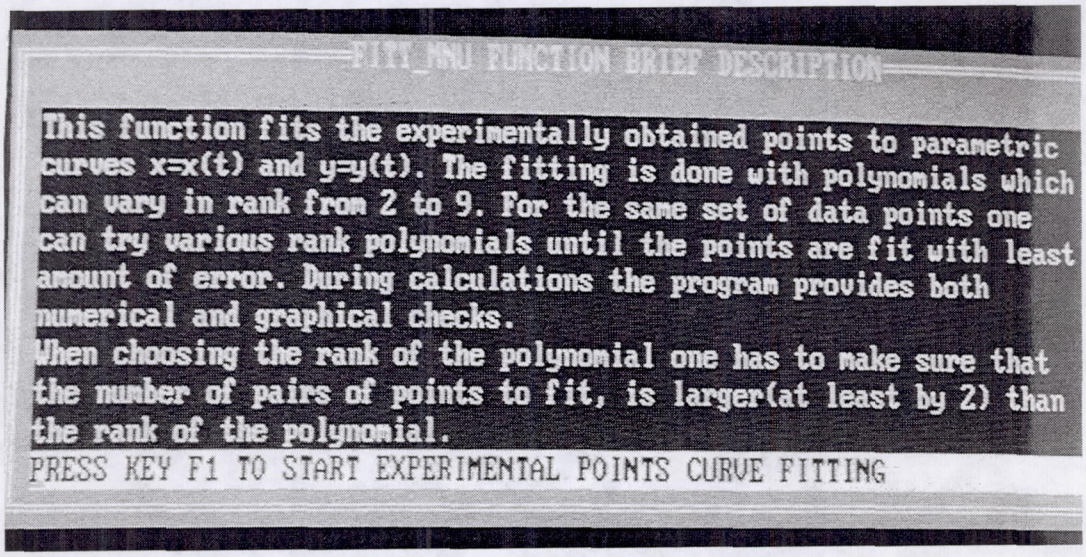



Figure 24: Text Describing Polynomial Curve Fitting Function

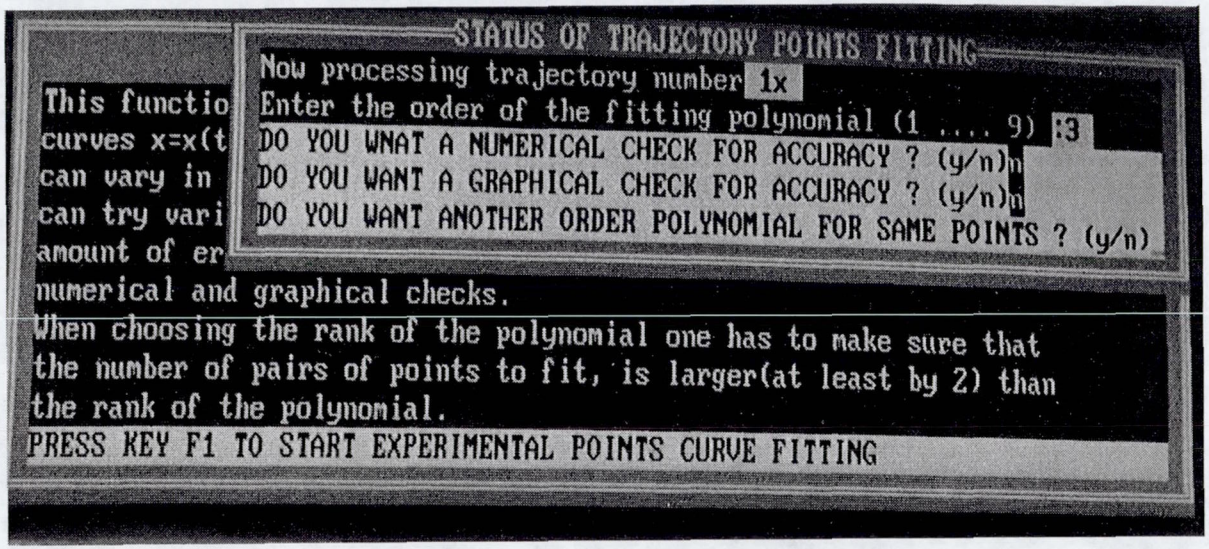



Figure 25: Polynomial Curve Fitting Selection Menu

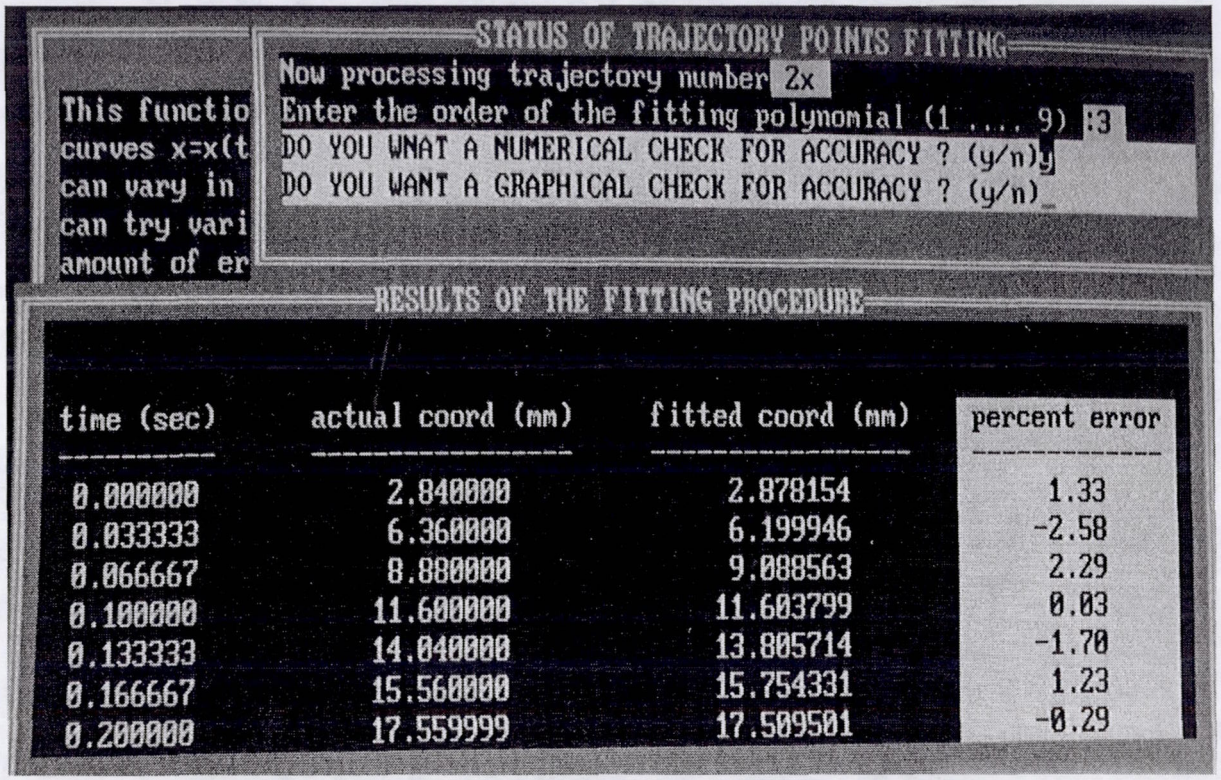



Figure 26: Screen Showing Numerical Check of 3rd Order Curve Fit

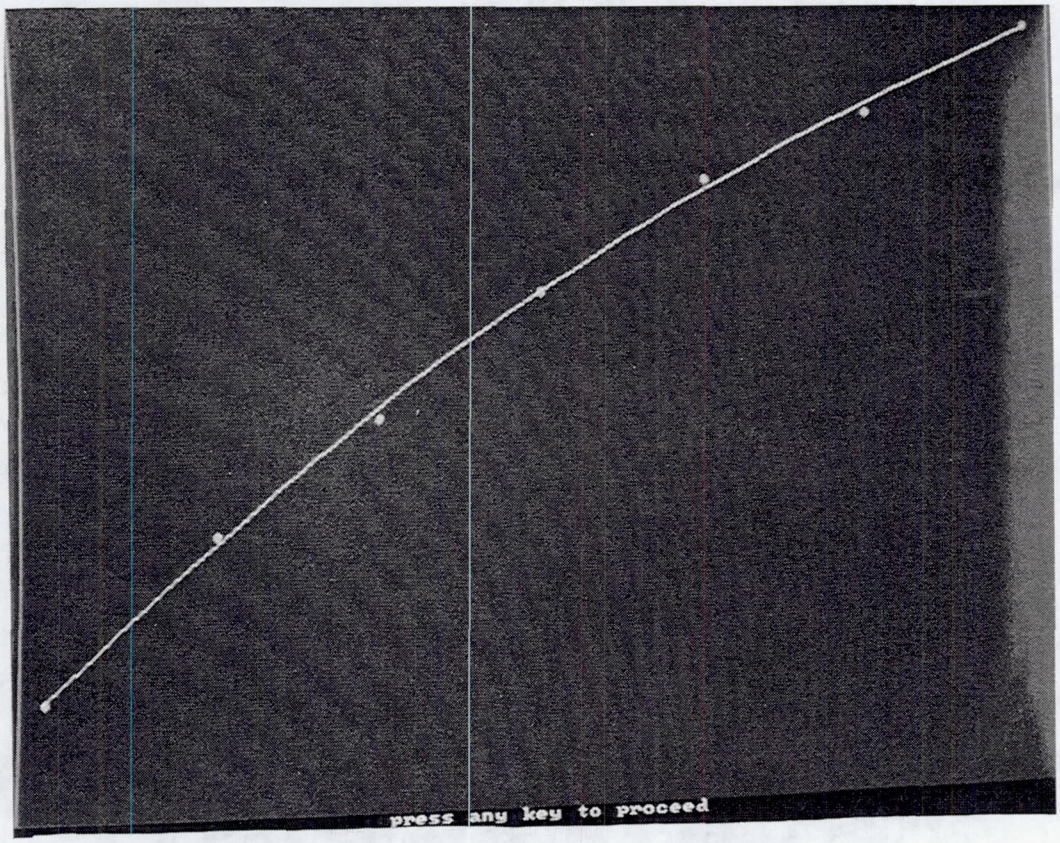



Figure 27: Screen Showing Graphical Check of 3rd Order Curve Fit

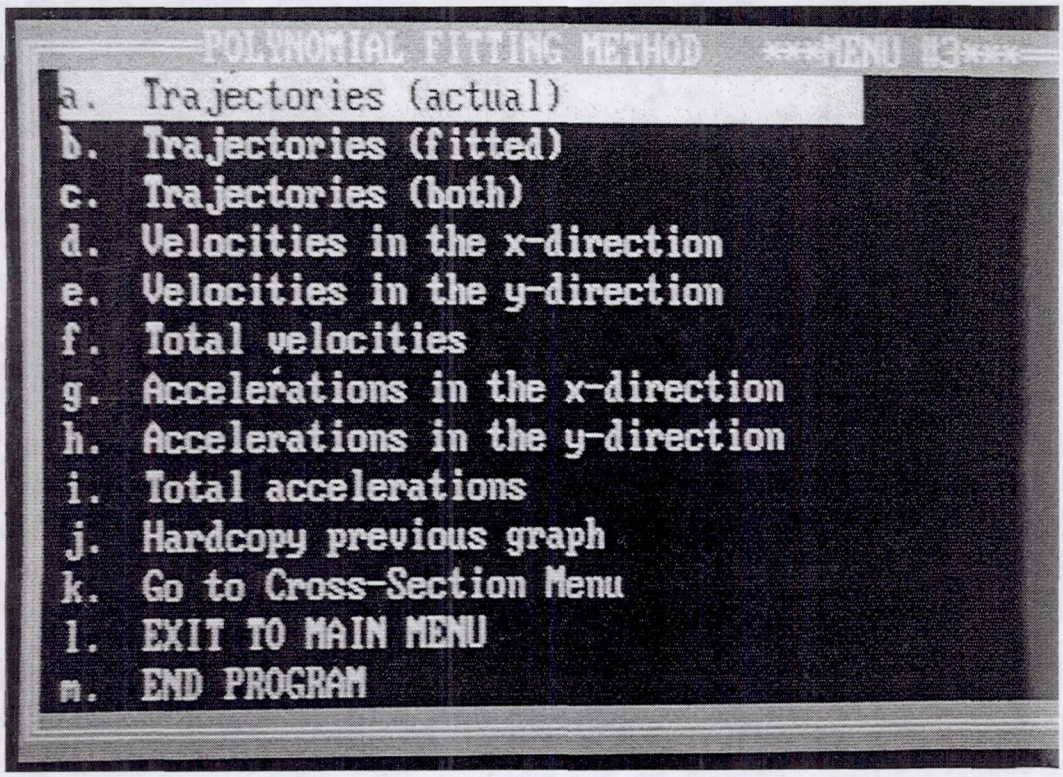



Figure 28: VADT Menu #3

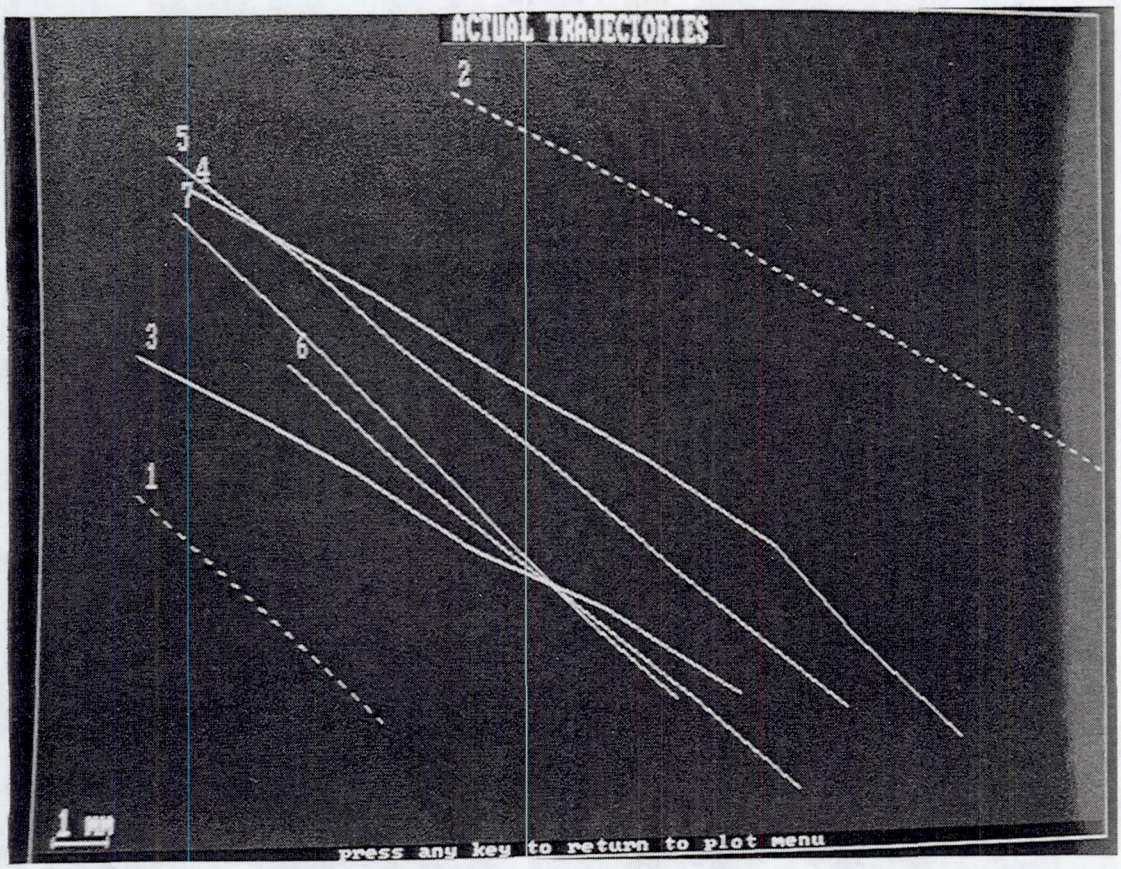



Figure 29: Screen Showing Digitized (Actual) Flow Trajectories

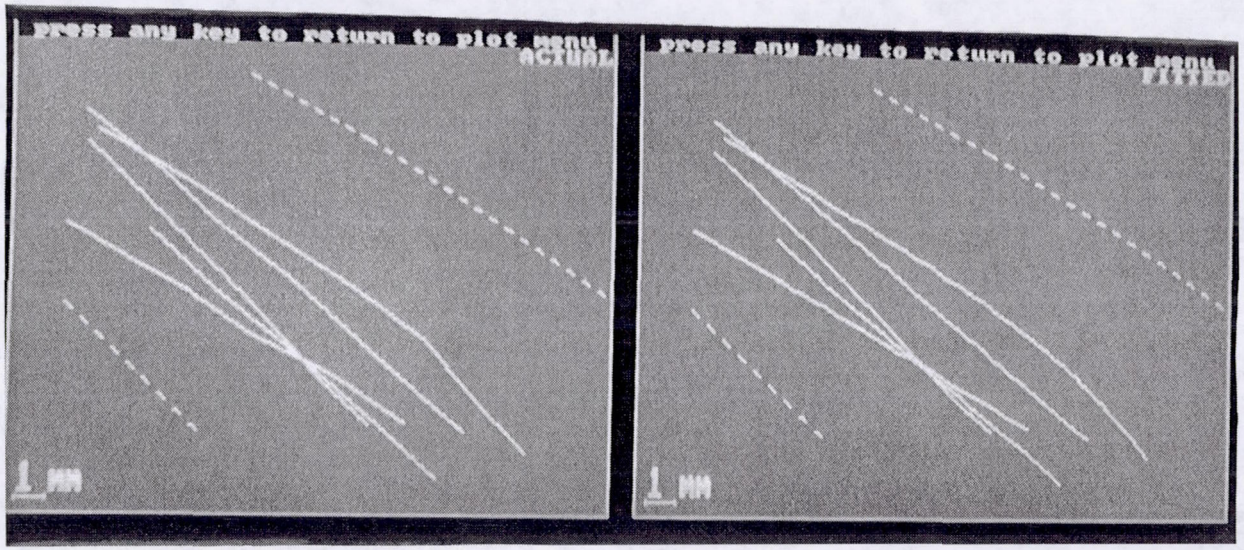



Figure 30: Screen Comparing Digitized (Actual) and Fitted Flow Trajectories

are the actual traced trajectories (menu selection 'a') and the comparison showing the actual and fitted trajectories (menu selection 'c') of a typical set of trajectories. Additional menu selections allow access to information regarding velocities and accelerations. As the fitted trajectories are in the form of polynomials, they are differentiated to determine the velocity and acceleration values at any point along all trajectories in the X, Y, and oblique directions (Equations 3 and 4).

$$\frac{dx(t)}{dt} = \sum_{i=1}^{i=1} i\, A_i t^{i-1} \quad (n=1...9) \tag{3}$$

$$\frac{dy(t)}{dt} = \sum_{i=1}^{i=1} i\, A_i t^{i-1} \quad (n=1...9) \tag{4}$$

By selecting menu selection 'k' (see Figure 28), the user can go to the cross sectional menu screen (Figure 31) that allows velocity and acceleration profiles to be displayed. Examples of X and Y velocity profiles for the same typical file used before are shown in Figures 32 and 33. The program also includes an option to print these profiles after they are viewed.

VADT creates a file, having the same root name chosen by the user in SNAP giving it the extension .rsl, containing the fitted and scaled data points, as well as the three corresponding velocity, and acceleration values at each point. The velocity and acceleration values stored in this file can also be graphically shown, again in the X, Y and resultant directions. The program is also capable of determining the velocity and acceleration values at any location on the trajectories between any two digitized points. Again, the program can draw a vector representation of the velocities and accelerations in the X, Y, or any oblique direction desired.

Since the camera is only capable of recording a limited area of the flow field at one time, the process must be repeated sufficiently enough times to

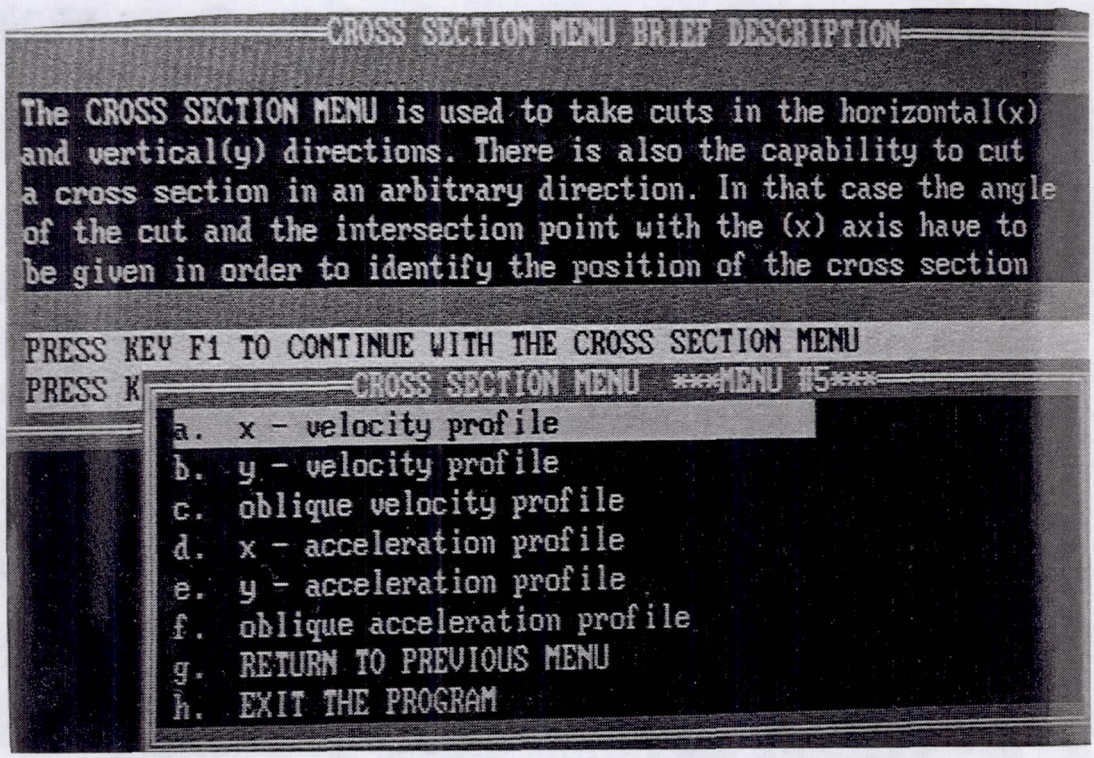



Figure 31: VADT Menu #5 (Cross Sectional Velocity Menu)

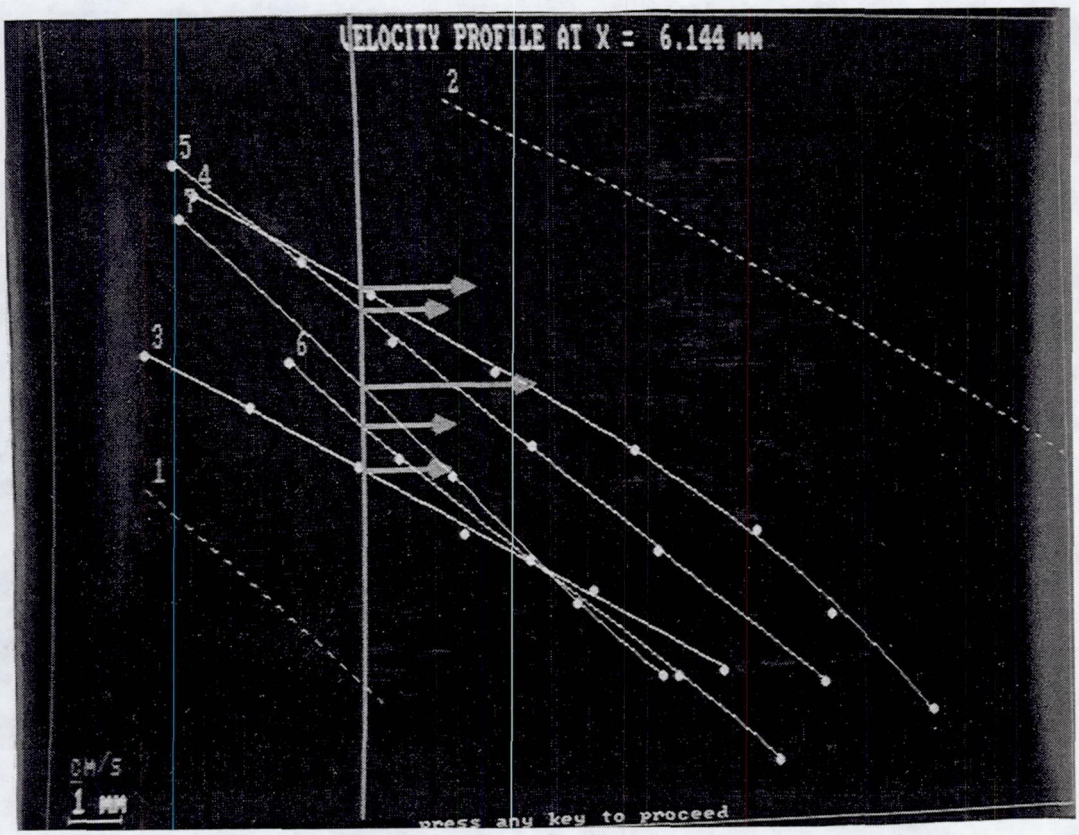



Figure 32: VADT-Generated X-Direction Velocity Vectors

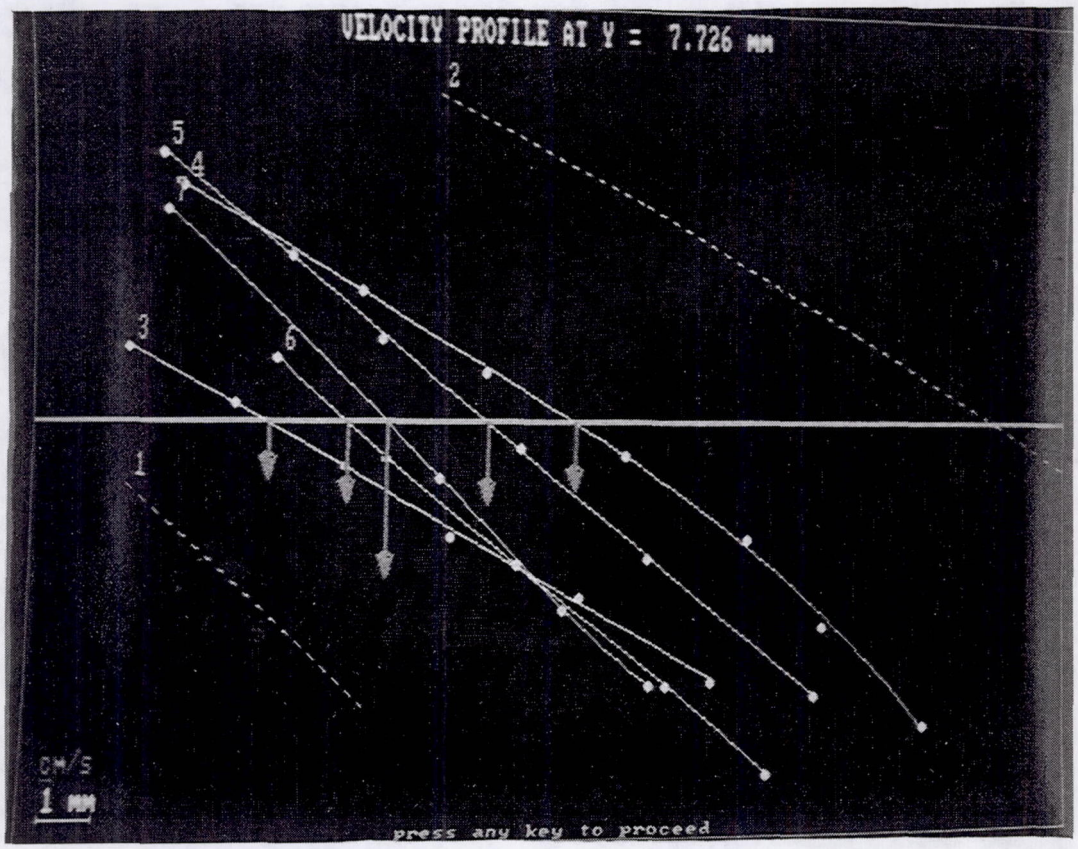



Figure 33: VADT-Generated Y-Direction Velocity Vectors

determine the entire test section flow field representation. Because the viewing area is limited, VADT creates an additional file, again having the same root name, with the extension **.inp** that allows a graphical representation of the boundaries and fitted trajectories to be imported into a Computer Aided Drafting (CAD) package. The drafting package utilized is Drafix CAD Ultra by Foresight Resources, and it accepts the '.inp' data files and allows the assembly of a qualitative representation of the flow through the entire area of study. Assembled flow fields will be discussed in Sections 5.4 and 5.5. Also, examples of the four output files discussed above can be found in Appendix A.

# CHAPTER 5

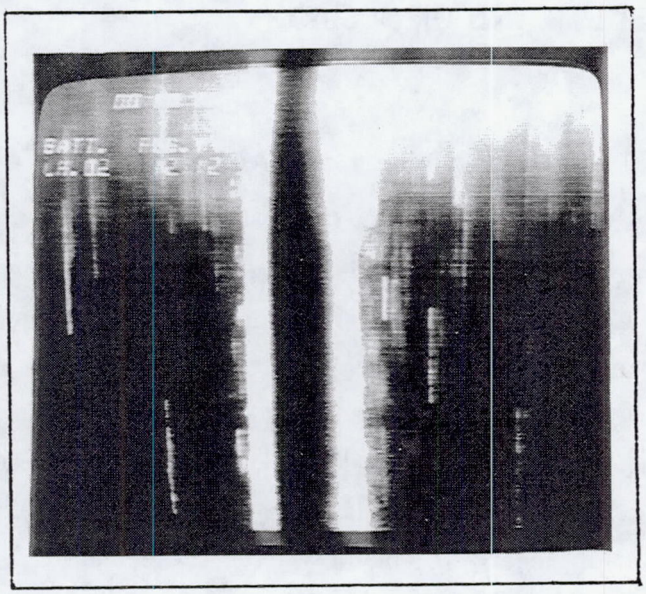
# RESULTS AND DISCUSSION

## 5.1 Visualization Studies of Flat Plates, Cylinders, and Airfoils

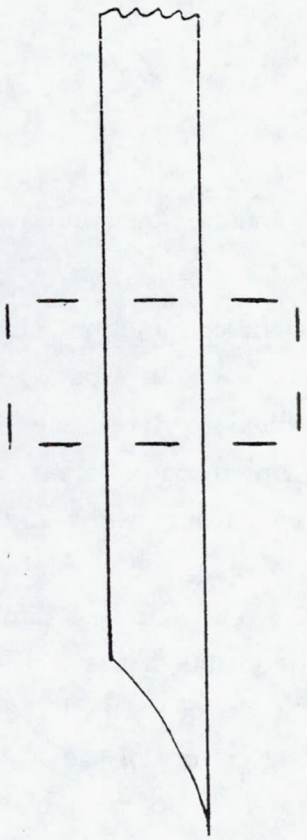
In conjunction with initial attempts to visualize flow in brush seals and cowl lip cooling passages, additional studies of simplified geometries were performed to determine the feasibility and limitations of extending the method from microscopic areas using optically matched oils [31,32], to macroscopic channels using water and air as working fluids [53,64]. Classical experimental models such as flat plates, cylinders, and airfoils were used in this preliminary work. While limited information regarding the flow over these classical models was determined, the studies proved to be very useful in improving and perfecting the aspects of the FFFT system. These preliminary studies served as not only the proving ground of the system itself in the larger macroscopic geometries, but also as the source of valuable training experience by the users of the FFFT system. The knowledge gained from performing these experiments proved to be useful when addressing obstacles encountered in the brush seal, cowl lip, and staggered pins experiments discussed in greater detail below. Some of the results of this preliminary work are enclosed here, concentrating on the lessons learned by performing these experiments.

### 5.1.1 Visualization of Flow Over a Flat Plate

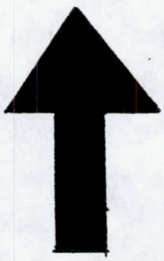
The study of the flow over a flat plate (Figure 34) was the first attempt to extend the FFFT/CIIQ method from experiments involving optically matched oils



FLOW OVER A FLAT
PLATE IN WATER



CUSPED
FLAT
PLATE



FLOW

Figure 34: Geometry of Flat Plate Used in Experiments

as the working fluid to experiments involving water, whose refractive index is different than that of the lucite walls of the channel and model itself. These experiments were performed at the NASA Lewis Research Center in the water tunnel described in Section 3.2 (Figure 5) that would later be used in the study of flow around various cowl lip geometries (see Section 5.3 below). These flat plate experiments provided useful experience regarding the operation of the water tunnel control system, while additional experience was also gained in the area of laser operation and light sheet control through the optimization of the cylindrical lens system. Examination of the photograph in Figure 34 shows the increase in the lengths of particle streaks at positions farther away from the flat plate. This is an excellent illustration of the variance of flow velocities existing in a single image. As the exposure time of the frame is constant (1/30th of a second), the varying lengths of particle streaks indicate that distances traveled over the same (exposure) time varies, meaning the velocity of the longer streaks is higher. The digitized flow profile shown in Figure 35 quantifies the velocity variance revealing the classical boundary layer profile.

### 5.1.2 Visualization of Flow Around a Cylinder

To determine the limitations and effectiveness of applying the FFFT method to turbulent flows in a macroscopic channel, a study of the flow around a cylinder was performed in the water tunnel (Figure 5) at the NASA Lewis Research Center. The wake and stagnation regions were studied at various flow rates. A still photograph illustrating the unsteady vortical motion of alternating or oscillatory flow patterns (von Karman vortices) behind a cylinder is shown in Figure 36. In this figure, the vortex from the left side of the cylinder is extended beyond the centerline of the cylinder. This reverses, and the vortex from the right then covers most of the area behind the cylinder. It was observed that an increase in flow rates resulted in an increase in intensity, and a decrease in the time periods between oscillations. The magnification power of the system was increased as several extension rings were added to the lens system to study the approaching flow in the stagnation region. The varying lengths of the streaks

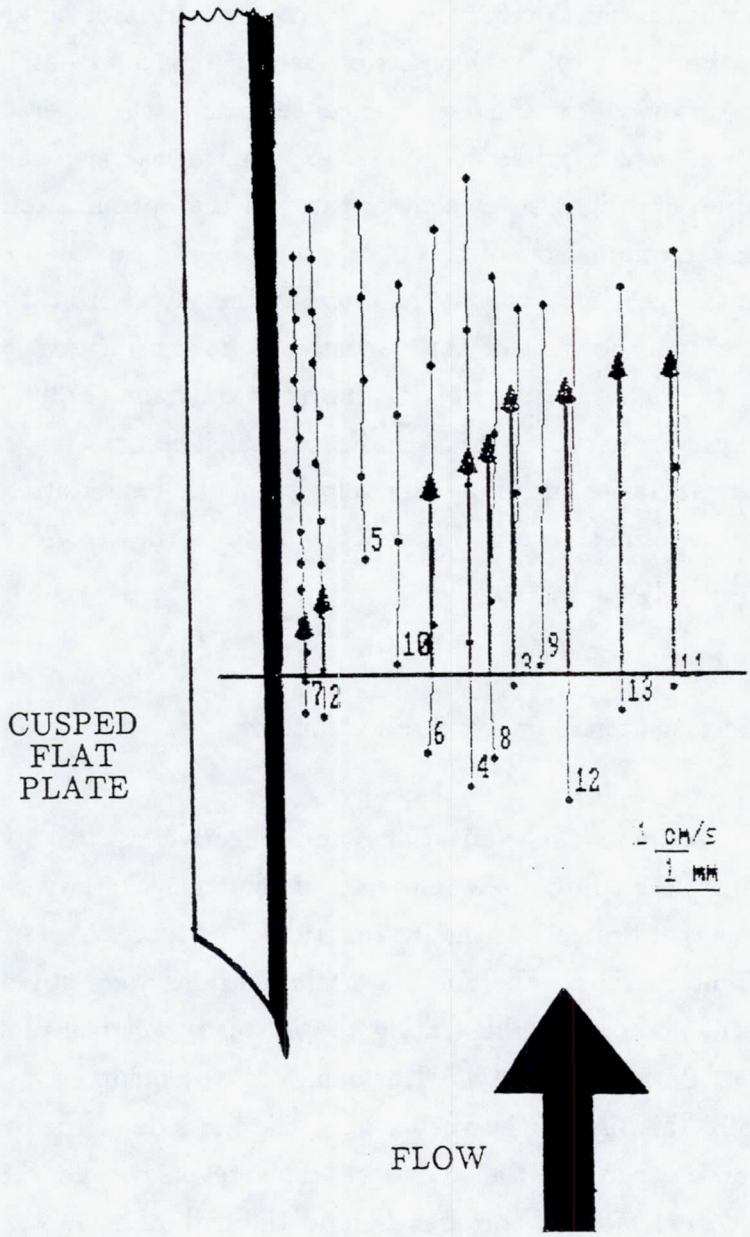



Figure 35: Digitized Flat Plate Velocity Profile

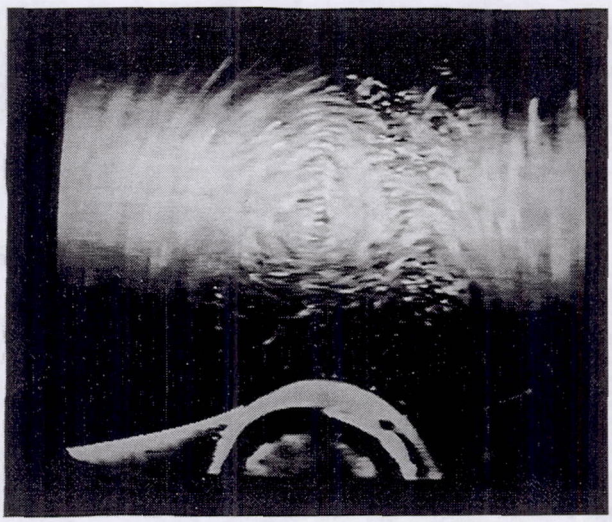


Figure 36: Vortical Flow Behind a Cylinder in Water

shown in Figure 37 illustrate the difference in speeds. The velocity of the flow directly upstream of the stagnation point is shown to be slow by the short streaks that can be seen in the figure. The longer streaks around the cylinder show that the velocity is higher as the flow curves around the flow obstruction.

### 5.1.3 Visualization of Flow Over Airfoils

Ice accretion on airfoils in flight can be fatal occurrences. Current studies underway investigate the manner of ice accretion on leading edges, the effect of ice on performance, and methods of ice prevention. A study using the FFFT method to compare the flow over two airfoils was performed. Figure 38 presents both a a 'clean' airfoil, and a second possessing the profile of an airfoil with a simulated ice shape designed into it. The goal of this project was to determine the flow patterns around both airfoils at different angles of attack, compare the velocity profiles around them, and determine the effective limits of the angles of attack in both cases. Attitude sweeps were performed from positive to negative angles of attack to visualize both the airfoils in qualitative fashion, and to place a limit on the acceptable angles. The angles that were considered were -8 to +15 degrees for the clean airfoil, and -4 to +8 degrees for the iced airfoil. Intense separation showing von Karman vortices can be witnessed at angles higher than this. Photos of both at small positive angles of attack are included in Figure 39 (clean airfoil) and Figure 40 (iced airfoil). In the original video data (not included), the oscillations illustrated in the photographs become clearer, and resemble the alternating vortices described earlier in discussion of the flow behind the cylinder. Qualitatively it was shown that the airfoil with a simulated ice shape obstructs and alters the smooth flow around the foil as expected, and is less effective than the standard NACA 0012. This agrees with the results of the prior work by Zaman and Potapczuk [76] that concluded that the increased turbulence created by an iced airfoil causes a reduction in the effective lift.

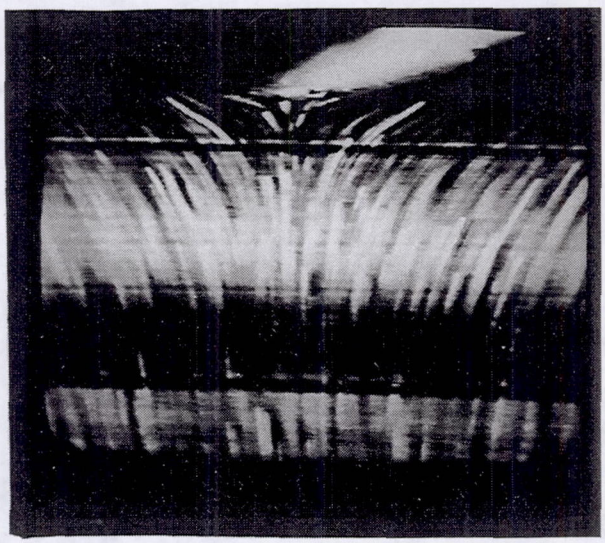


Figure 37: Stagnation Region of a Cylinder in Water

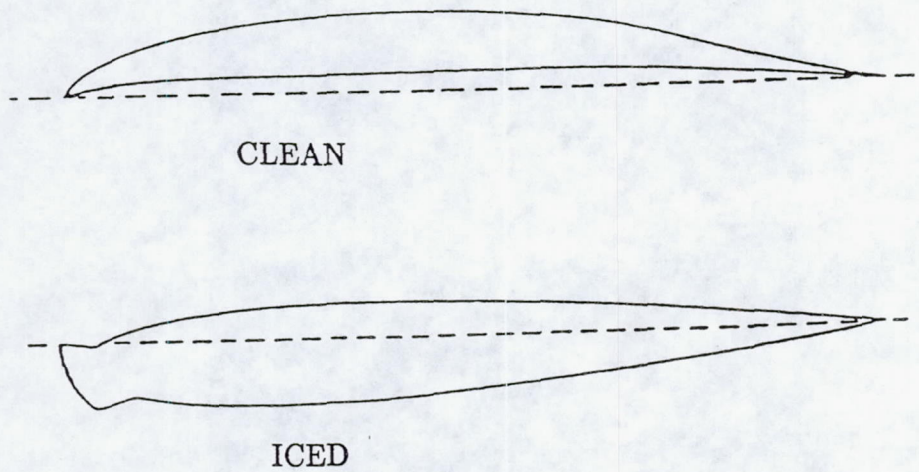



Figure 38: Geometries of Airfoils Tested in Water

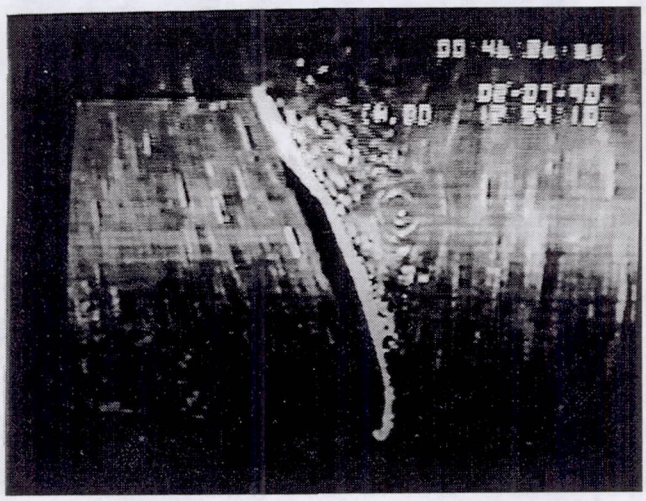


Figure 39: Photograph of Flow Over a Clean Airfoil

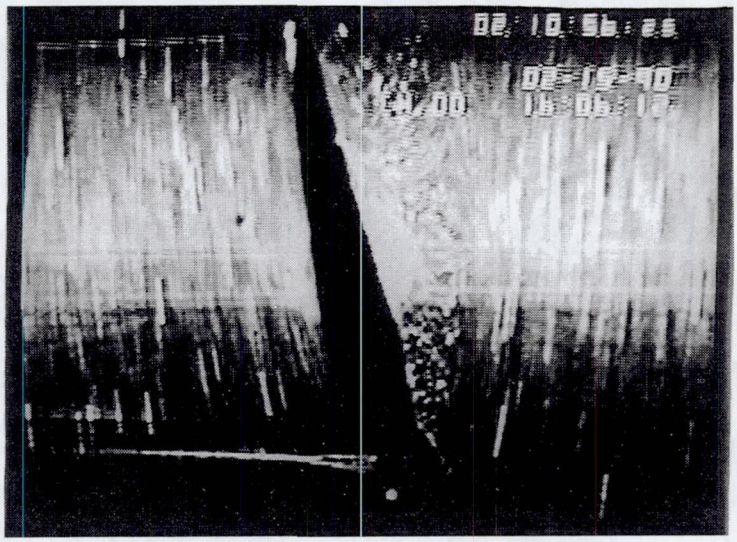


Figure 40: Photograph of Flow Over Iced Air Foil

## 5.2 Visualization Studies of Flow Through Brush Seals

As a benchmark for computational codes currently being developed, flow visualization and quantification of flow through a brush seal was desired. The initial analysis was done in optically matched silicon based oil, and later in water. The intent of the work was to determine the pressure drop and sealing effectiveness for various brush seal configurations containing different diameter bristles. The brush (Figure 1), modeled as a linear section of a brush with an infinite radius, was mounted in an oil tunnel (Figures 2 and 4). The clearance of the brush is defined in the experiment as the distance between the end of the bristles and the side wall, as opposed to a rotating shaft in an actual engine. The clearance must be minimized to effectively allow the brush to seal, and for these experiments it was kept between 20 mils [0.020 in. (0.508mm)], considered a large clearance, and an interference fit. Some of the characteristic flows found within a brush seal are discussed and shown below, as well as the results of the various flow quantifications.

A brush has a varying bristle density due to manufacturing imperfections. Under experimental flow conditions, brush fibers are displaced due to the pressure acting on the seal. This displacement and the strains created during manufacturing and installation create transient and spatial variations through the brush. These variations within the bristle matrix occur not only in the direction of the flow, but also axially along the bristles from the attach point to tip. These distinct configurations contain areas of varying porosity that alter the path of the flow through the brush as the working fluid attempts to follow the paths of least resistance by flowing through the spatial voids in the brush. It is important to keep the clearance to a minimum to allow the brush to seal properly. As the upstream pressure and the mass flow increase, the uniform flow approaching the fibers becomes nonuniform as it is deflected from regions of closely packed fibers to regions of loosely packed fibers. These diverted flows tend to form rivers and jets between the rows of fibers, thus engendering secondary flows with random and chaotic vortices. Figure 41 shows the mass flows associated with changing the head pressure from 20 psi to 80 psi.

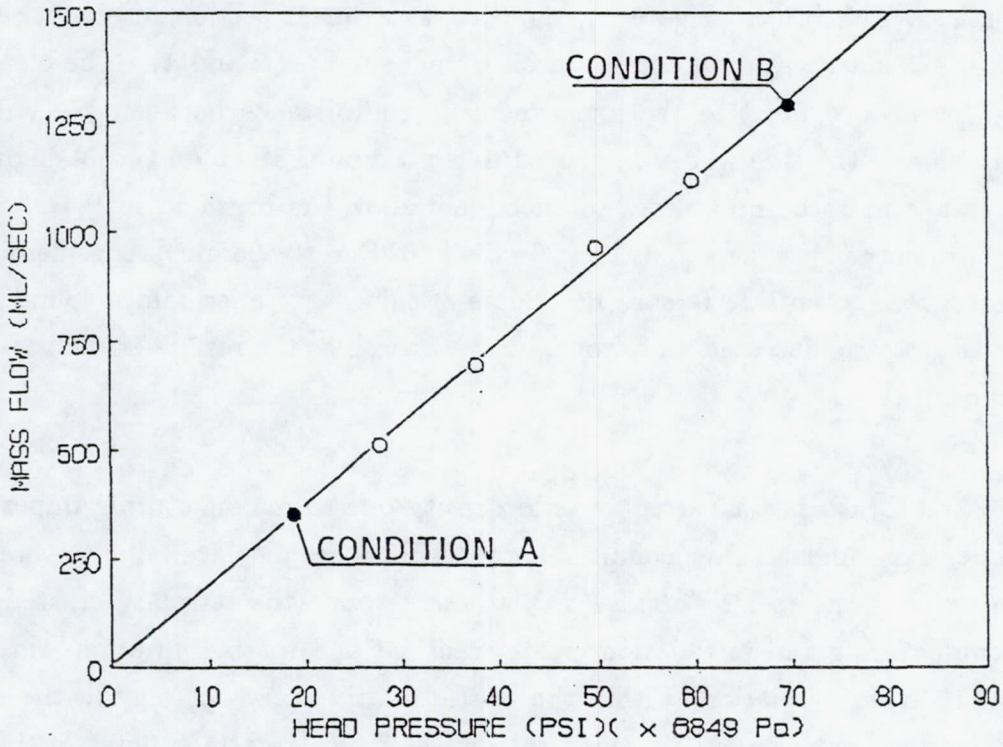



Figure 41: Mass Flow vs. Head Pressure Curve

Figures 42 and 43 present images at 60x obtained using the long distance microscope (LDM, Section 3.4) containing the Questar lens. The positions of the brushes at the two mass flows, 300 ml/sec (A) and 1200 ml/sec (B), were recorded on video tape, and digitized. The series of photographs in Figure 42 shows a powerful jet of fluid separating Bristles 2 and 3 as the flow rate is increased from Condition A to B. The two bristles are shown in contact with each other in Figure 42.1, while in Figure 42.6, they have been separated and relocated a distance of more than their 2 mm diameter. Figure 43 presents a chronological series of enlarged images of a group of fibers located at the exit section of a brush. As the flow increases between conditions A and B, bristles 1 and 2 are pushed apart allowing the penetration of a strong jet. The vertical space between bristles 1-2 and 3-4 at the higher mass flow exhibits a strong lateral flow which increases the effectiveness of the seal.

Figure 44 presents the change in position of four brushes (1mm diameter bristles) in series. The images were assembled to quantify the global motion of the bristles as the flow rate is increased from Condition A to Condition B (see Figure 41). Figures 44a, 44c, 44e, and 44g present a comparison of the positions of the upper three bristle rows of each brush, while Figures 44b, 44d, 44f and 44h present the same comparison for three middle rows. Inspection reveals that as the flow rate is increased from condition A to B, the bristles in the top rows of the first two brushes move between 2 and 3 mm downstream, while the spacing inside the brush increases. The displacements are of the bristles in the first brush are larger than those of the other brushes due to the higher upstream pressure. Adding more brushes in series increases the resistance, reduces the flow rate, and increases the pressure drop. The advantages of multiple brush seal configurations can be seen by comparing the pressure drops across the four configurations shown in Figures 45-48. The pressure tap locations are also included for each of the four configurations as they varied between each.

Evaluation of local fluid flow patterns are useful in the process of building a full quantitative trajectory map of the velocities in the brush, to support the qualitative conclusions derived from the study of Figures 41-48. The velocity

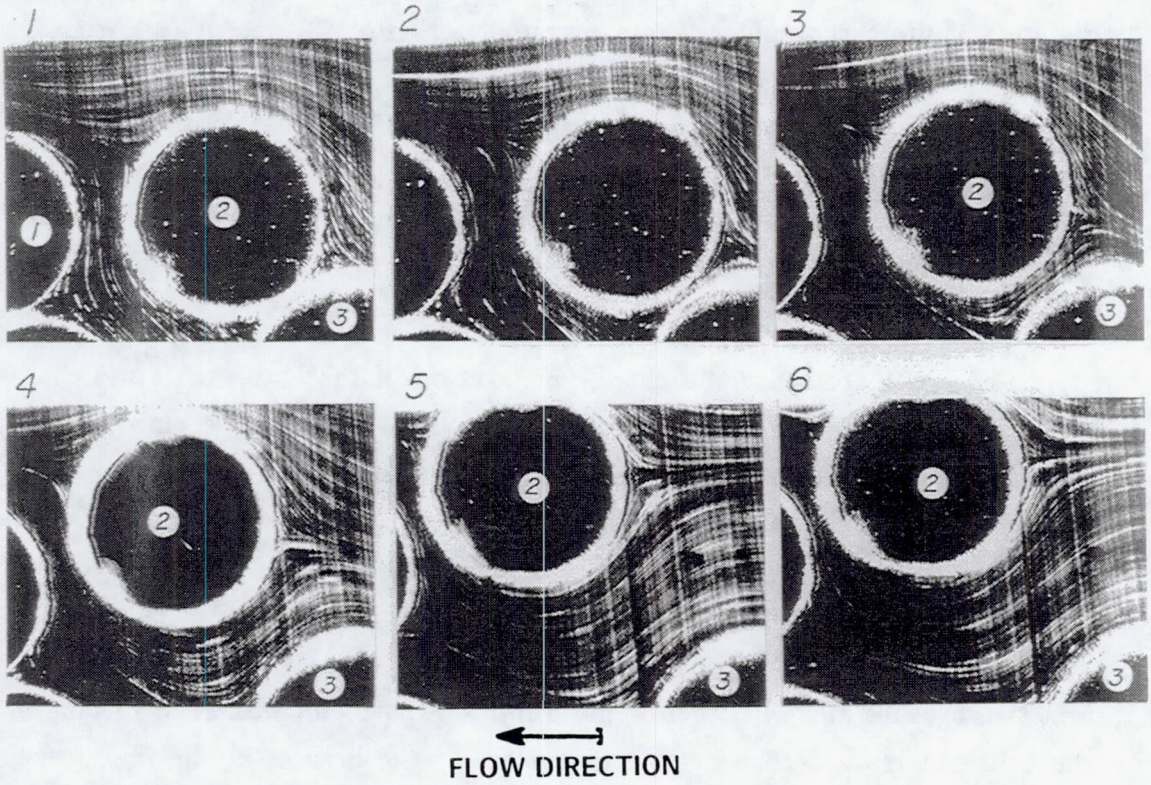



Figure 42: Photographic Sequence Illustrating Bristle Motion at Brush Seal Inlet

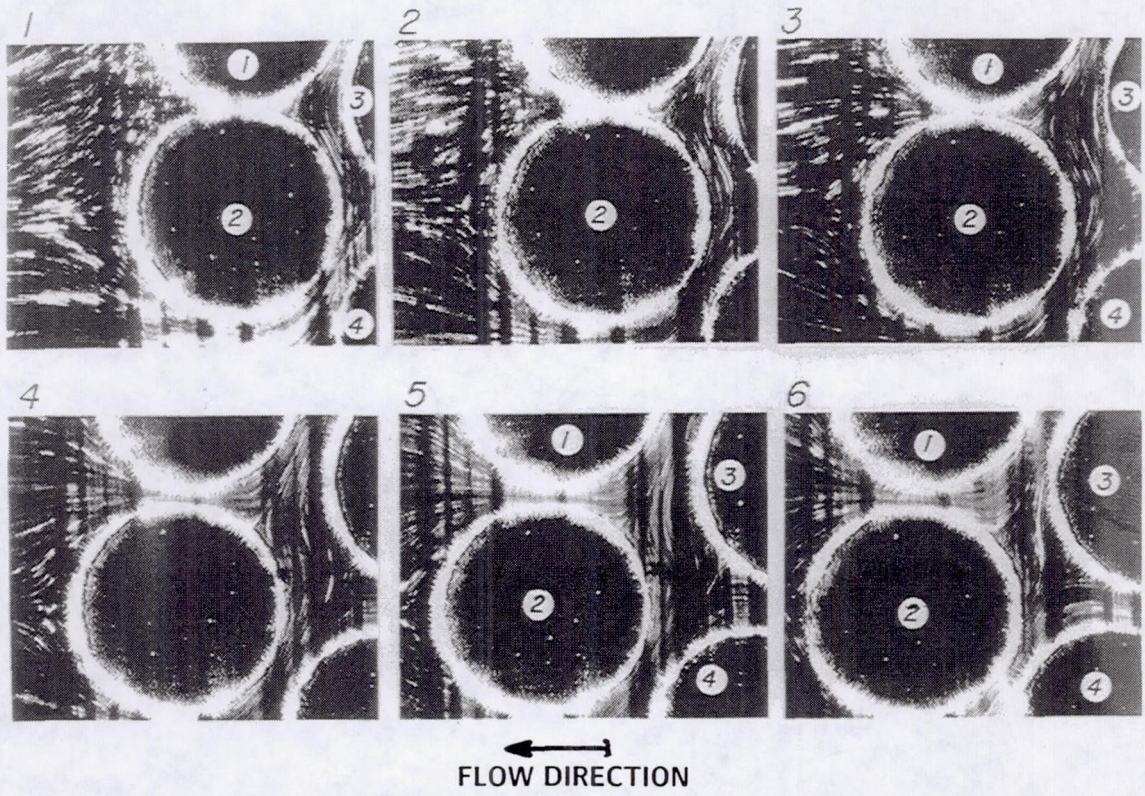



Figure 43: Photographic Sequence Illustrating Bristle Motion at Brush Seal Exit

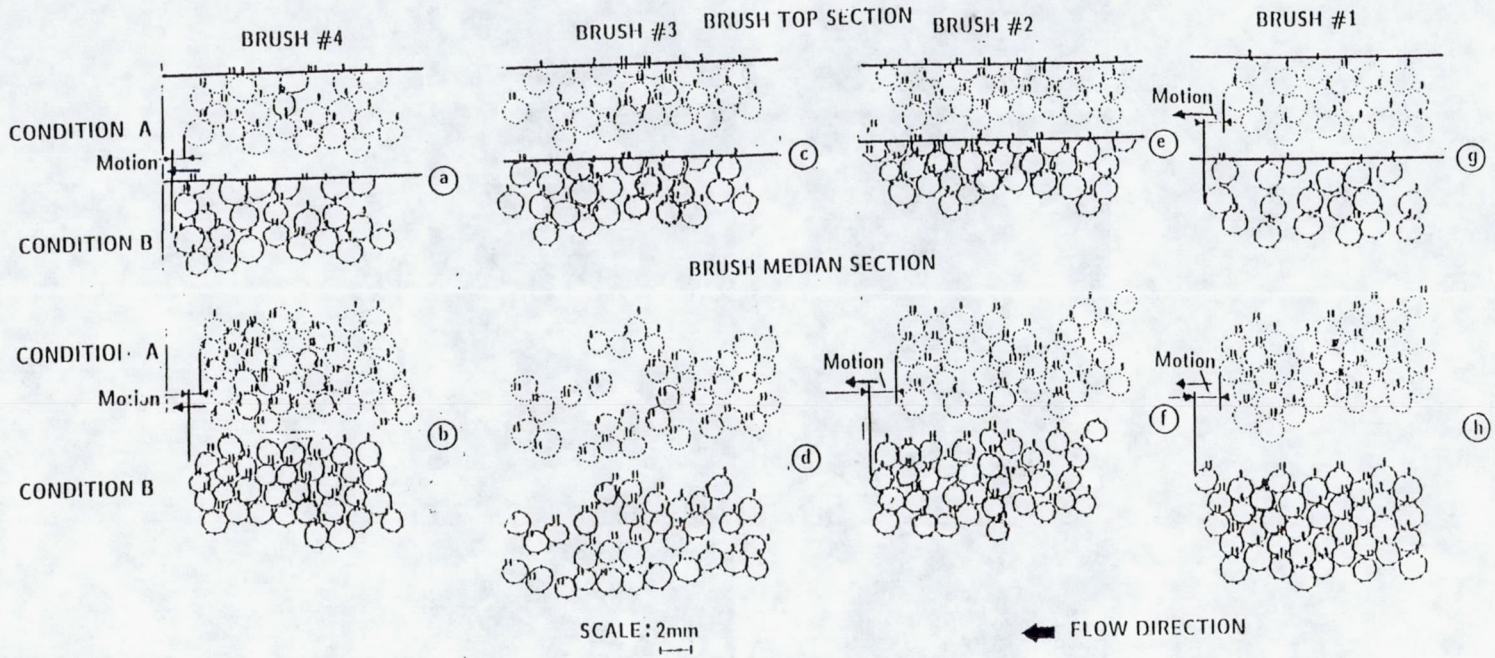



Figure 44: Digitized Bristle Motion at Conditions A and B (see Figure 41)

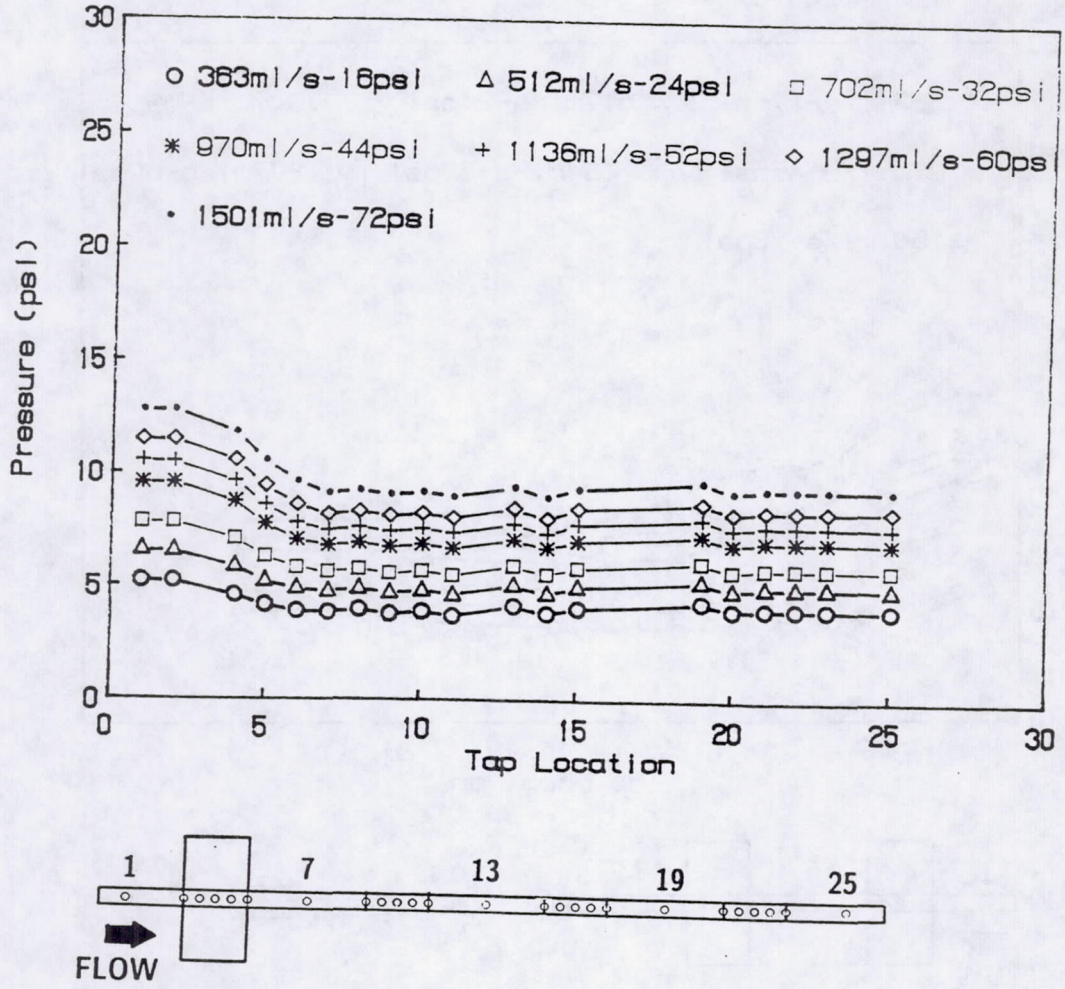



Figure 45: Pressure Profile for Flow Through One Brush Seal
(1 mm Diameter Bristles)

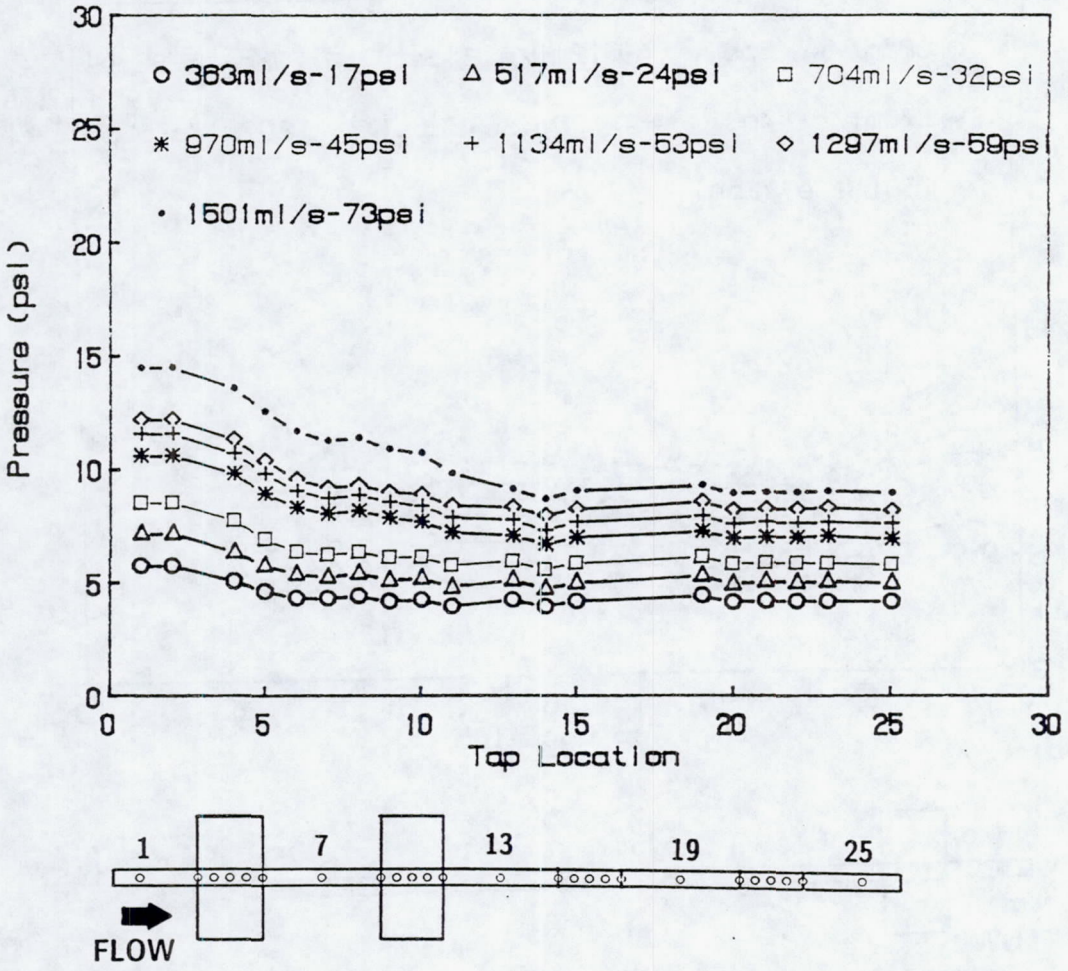



Figure 46: Pressure Profile for Flow Through Two Brush Seals in Series
(1 mm Diameter Bristles)

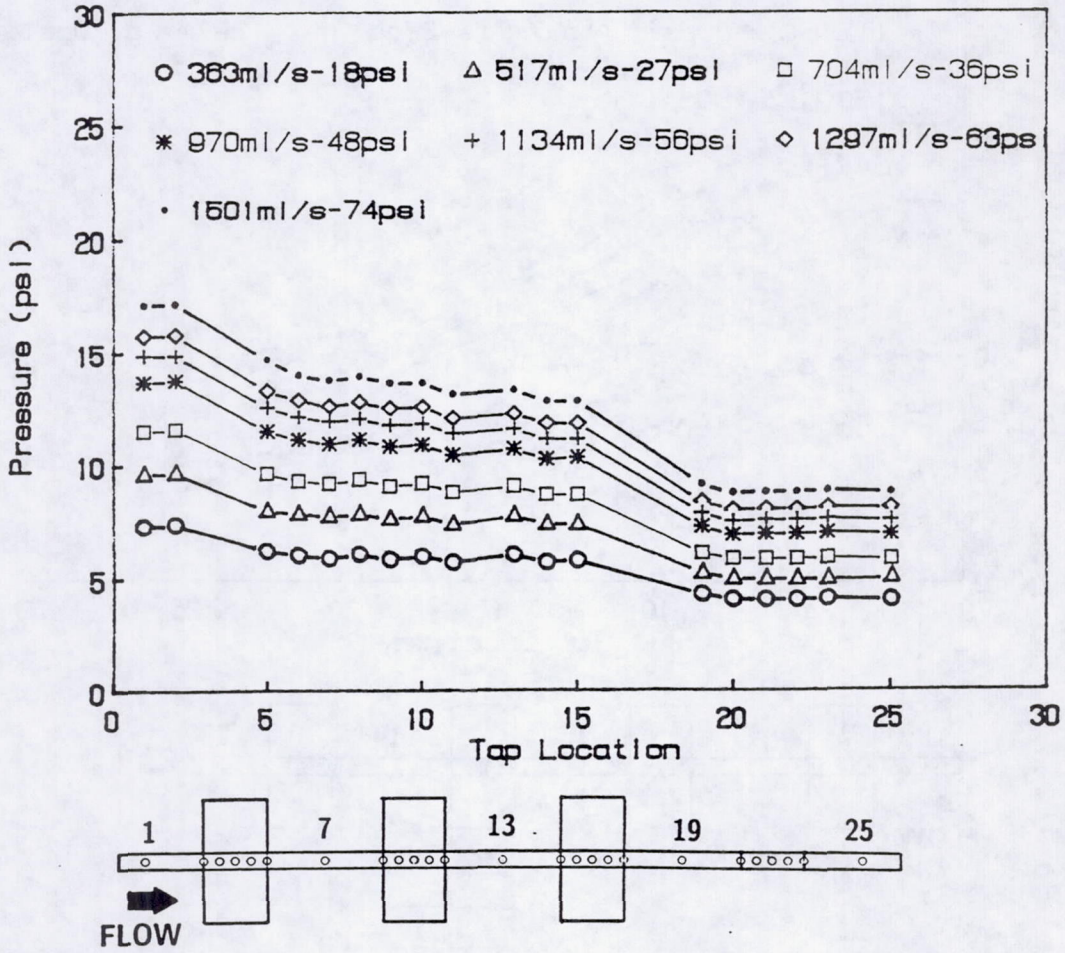



Figure 47: Pressure Profile for Flow Through Three Brush Seals in Series (1 mm Diameter Bristles)

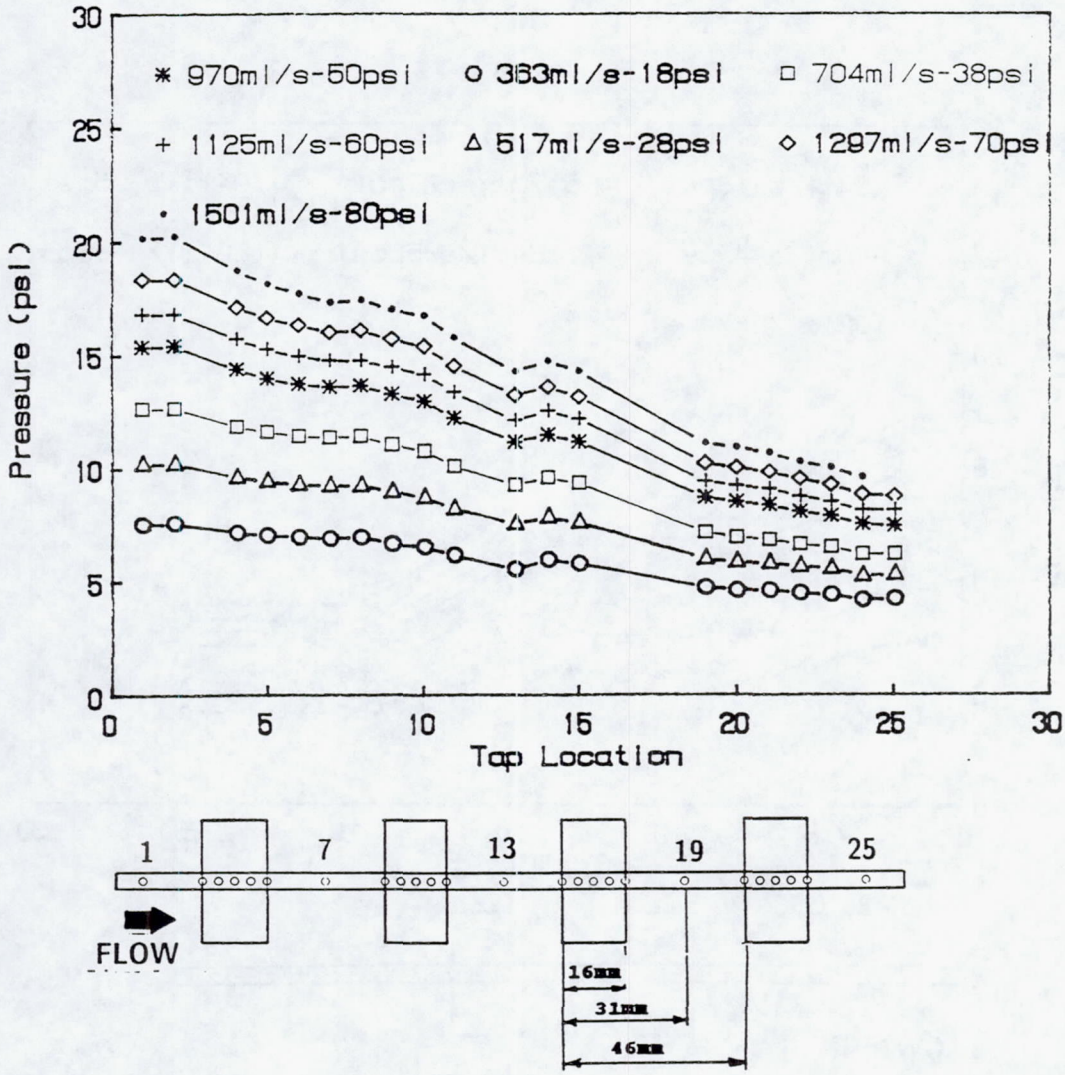



Figure 48: Pressure Profile for Flow Through Four Brush Seals in Series (1 mm Diameter Bristles)

information, in conjunction with the pressure distribution maps across the brush, contribute to the experimental evaluation of the brush seal effectiveness, and the development of more advanced seal configurations. Two brush configurations were compared with the above 1 mm diameter bristle experimental results. The pressure tap arrangements are included in both figures, as they varied slightly from the configurations in Figures 45-48. The graph in Figure 49 shows the pressure drop occurring for flow through a 2 mm diameter bristle brush. Figure 50 shows the pressure drop for the flow through the same 2mm diameter-bristle brush in series with a 1 mm diameter bristle brush. Local pressure increases caused by flow reversals within the bristle matrix can also be seen in Figure 50, and are discussed below.

The flow in the area of the brush shown in Figure 51 has been visualized and quantified using the FFFT technique. Figure 51A shows a map of the inlet region of a 2 mm diameter bristle brush, subdivided into four reference windows, each to be individually discussed. Figure 51B (Window C) presents the flow patterns in the region adjacent to the upper wall at the brush inlet. This is a good example of jetting and lateral flow effects which are caused by the non-homogeneous spacing of Regions 1, 2, and 3. Figure 51C (Window A) presents detailed flow entering the first few rows of the brush. Locations where the bristles are bunched together, such as Bristles 3 and 9, prohibit the flow from penetrating between them. The flow then follows the path of least resistance and travels around them. This creates extended portions of lateral flows (regions near Bristles 1, 3, 4, 5, and 6) or zones where flow merges from several directions (region near Bristles 7 and 8). Figure 51D (Window D) presents quantified flow trajectories and velocities. The bristle configuration alters the flow between Bristles 9 and 10, rendering it nearly perpendicular to the direction of the free stream flow. The velocity vectors, computed using the FFFT method, reveal that the perpendicular velocity has become twice that of the free stream flow velocity entering the brush. This physical situation contributes to efficient sealing and causes large axial pressure drops by increasing the flow resistance of the brush configuration.

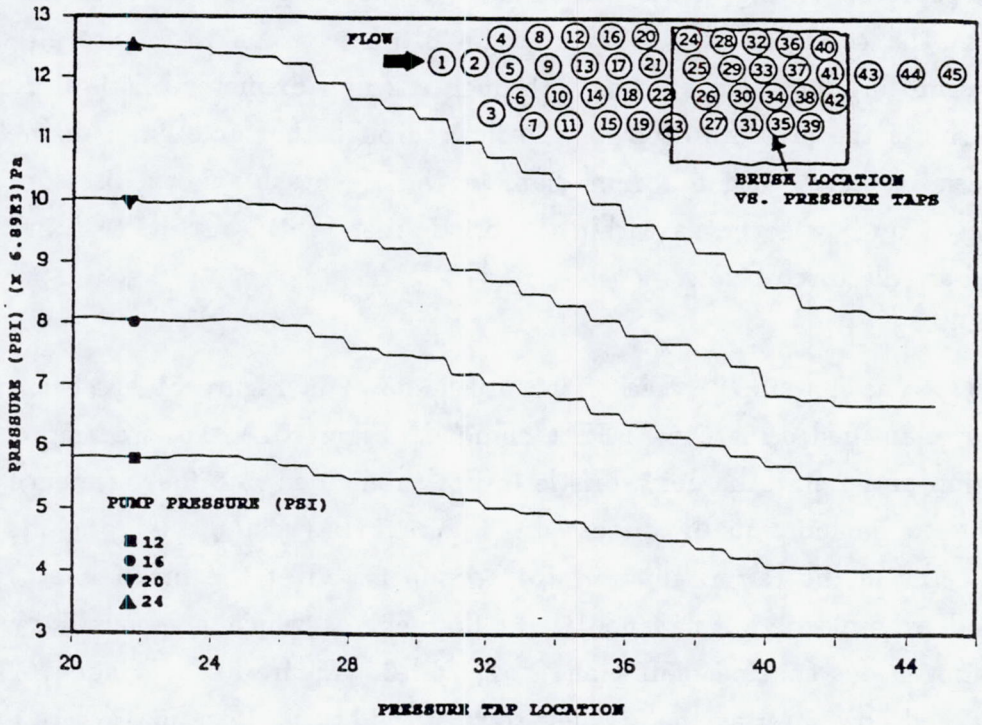



Figure 49: Pressure Profile for Flow Through One Brush Seal
(2 mm Diameter Bristles)

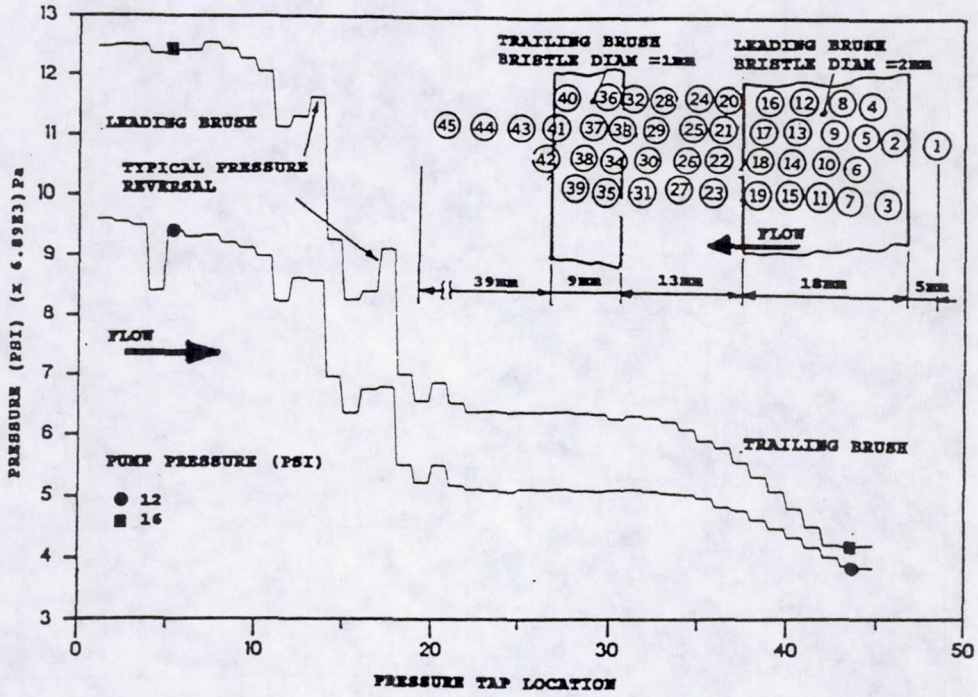



Figure 50: Pressure Profile for Flow Through Two Brush Seals in Series (2 mm Diameter Bristles-Leading/1 mm Diameter Bristles-Trailing)

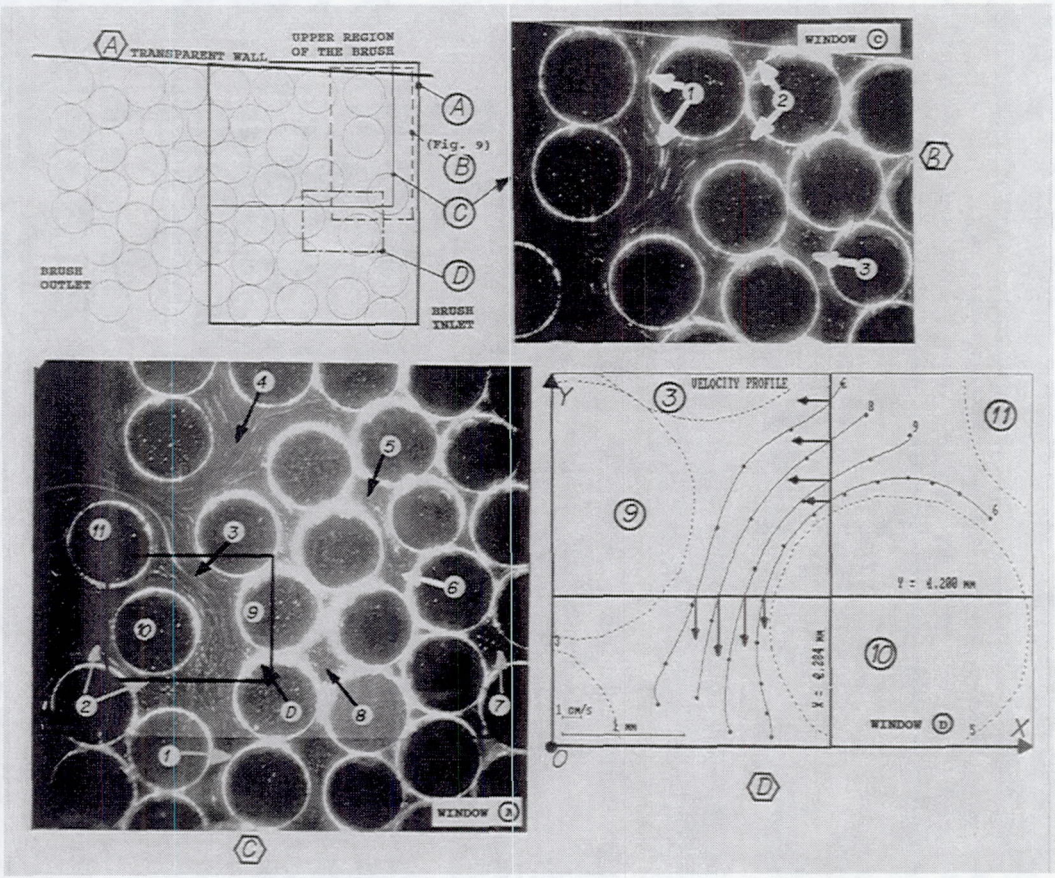



Figure 51: Qualitative and Quantitative Flow Assessment in the Inlet Section of a Brush Seal (2 mm Diameter Bristles) in Oil
A) Map of the Upper Region of the Brush Seal
B) Flow Visualization of Window C
C) Flow Visualization of Window A
D) Quantification of Flow Trajectories in Window D

Figure 52 presents flow in Window B of Figure 51A at the brush inlet adjacent to the upper wall. The flow is diverted from passing between the wall and the brush downward, as Bristle 1 is in direct contact with the wall. A jetting effect can be observed in the region between Bristles 2 and 4 in Figures 52A and 52C as the fluid accelerates and decelerates as if it were passing through sequential inlets. The vectors in Figure 52C show that the velocity of the fluid increases as it passes through the smaller width. The stagnation point of Bristle 3 can be observed in both Figures 52A and 52B. This flow pattern around Bristle 3 is similar to the flow approaching a cylinder, however the neighboring brushes affect the symmetry of the flow.

The above brush seal flow analysis was repeated using water as the working fluid. Water was used to show the effects of a less viscous fluid in the brush seals. The end wall effects, and the overall leakage were found to increase as a direct result of the lower viscosity. The resulting flow patterns can be seen, with their overlays, in Figures 53 and 54. Figure 53 presents flows in the inlet region of a brush in water. Regions 1-5 of Figure 53 illustrate typical flows present within the brush matrix. The effects of the nonhomogenities in the matrix can be seen in the rivering and jetting flows in Figure 53 in Regions 1 and 5. Regions 2, 3 and 4 exhibit vortical motion common to areas of contacting bristles. Figure 54 shows the outlet regions of the flow through the brush. This complex flow field involves many types of flows. Region 1 of Figure 54A and its overlay 54C illustrate the jetting effect caused by loosely packed bristles near the wall. This jet results in the adjacent vortex shown in Region 3. Multiple vortices (Regions 2) separated by a river-like stream (Region 4) are evident emerging from loose fiber areas. Examination of Figure 54B and its overlay 54D reveals a lateral crossflow (Region 1). This crossflow results in a self-sealing effect. Lateral flows within the interior of the brush and along its exterior provide a barrier for fluid attempting to follow the flow paths which increase the effectiveness of the seal. A summary of typical flow formations that were visualized and occur frequently in a brush seal is shown in Figure 55. These patterns show regions that are characteristically rivering, jetting, lateral, or vortical. The end wall flows only occur in linear brush seals, and are not present in brush seals used with rotating shafts.

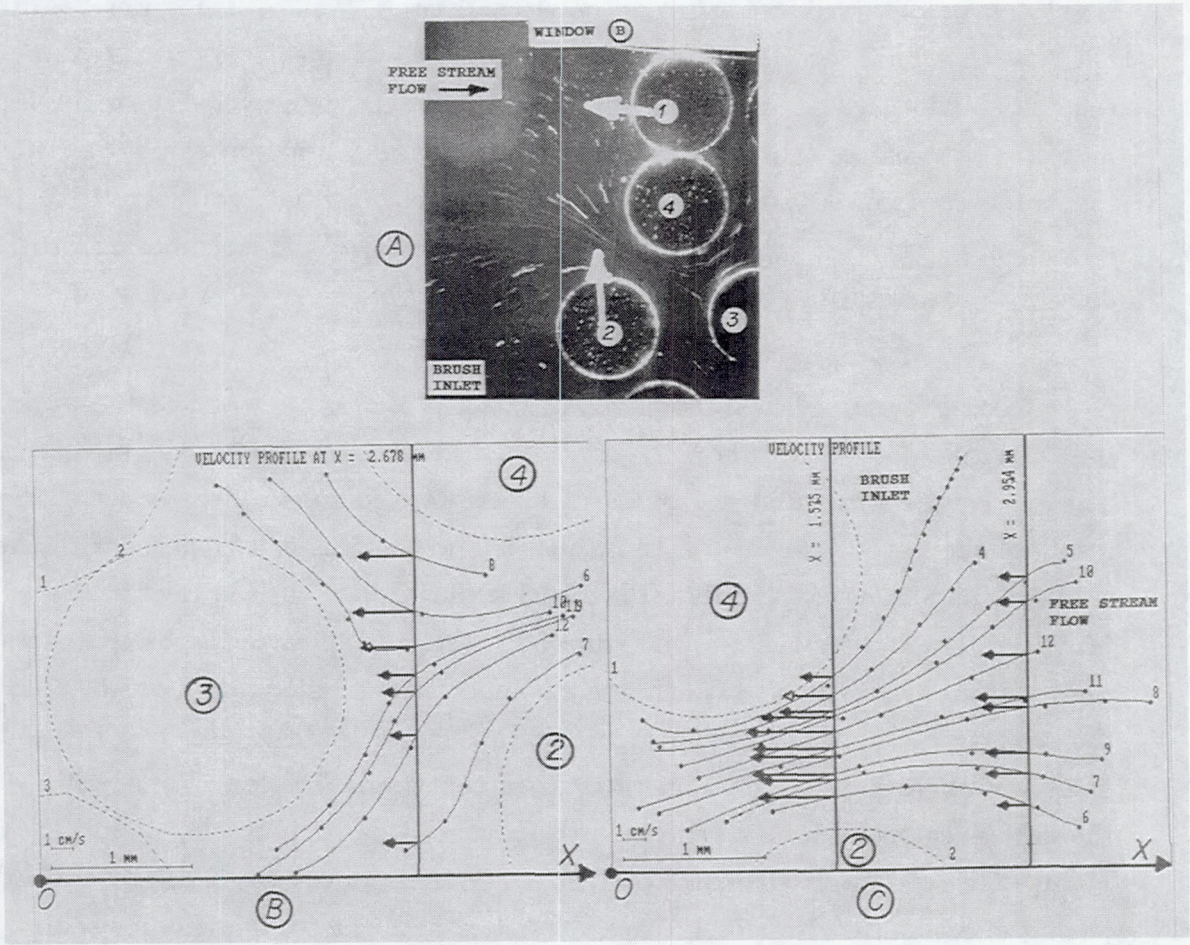



Figure 52: Qualitative and Quantitative Flow Assessment in Window B (see Figure 51)

A) Flow Visualization at Brush Inlet Adjacent to Upper Wall
B) Flow Trajectories and Velocities Around Inner Bristle 3
C) Flow Trajectories and Velocities of Upstream Free Stream Entering Spatial Void Between Bristles 2 and 4

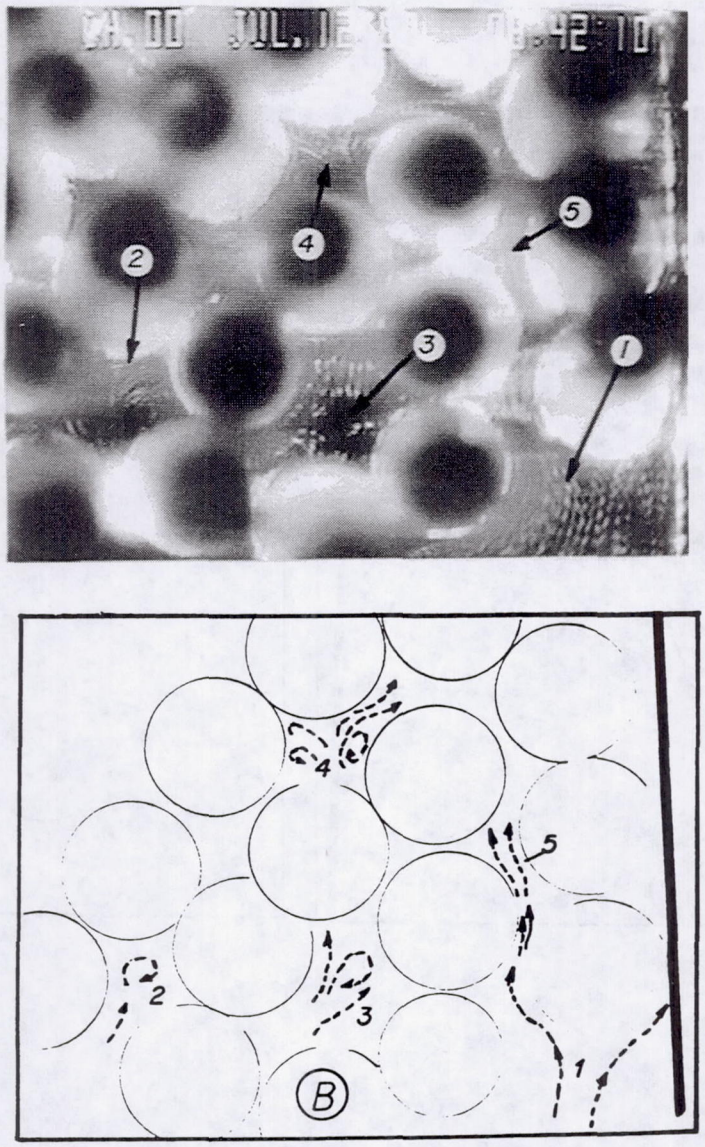



Figure 53: Visualized Flows at Inlet of Linear Brush Seal in Water
A) Photograph
B) Overlay

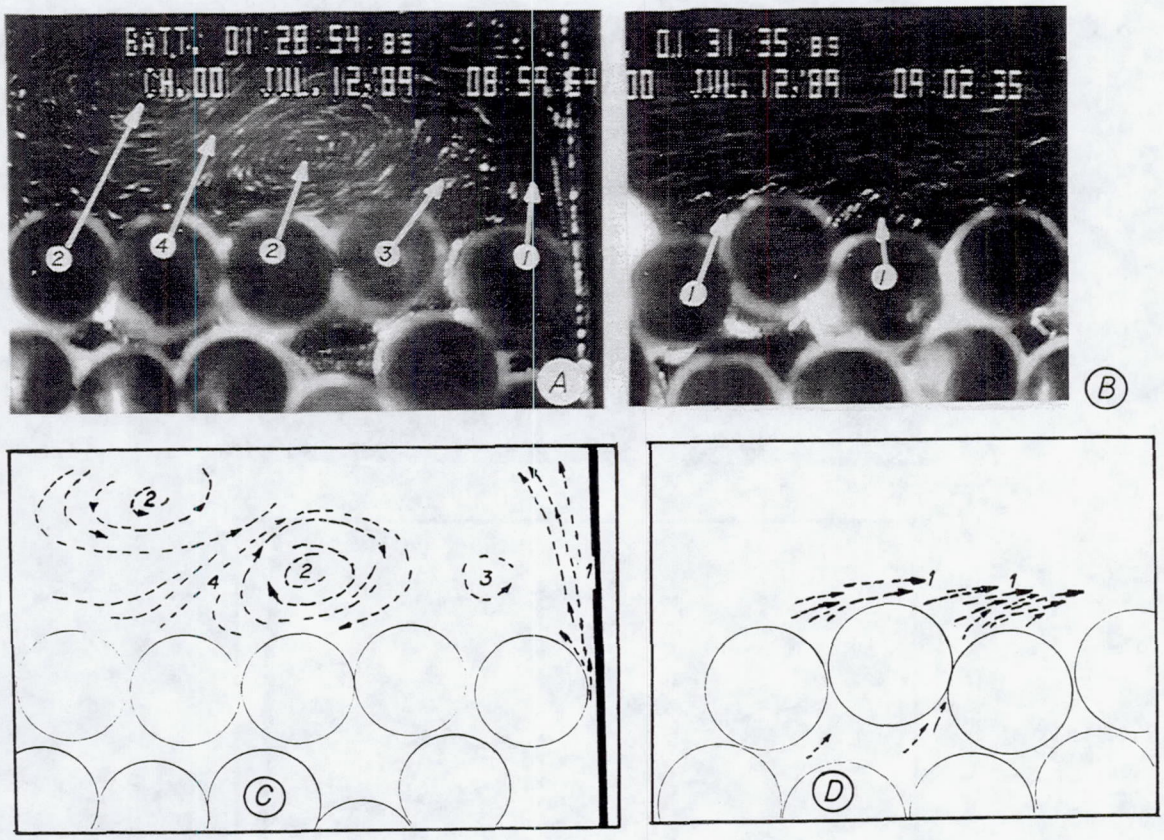



Figure 54: Visualized Flows at Exit of Linear Brush Seal in Water
A) Photograph of Flow Near Wall
B) Photograph of Exit Lateral Flow
C) Overlay of Flow Near Wall (see Figure 53A)
D) Overlay of Exit Lateral Flow (see Figure 53B)

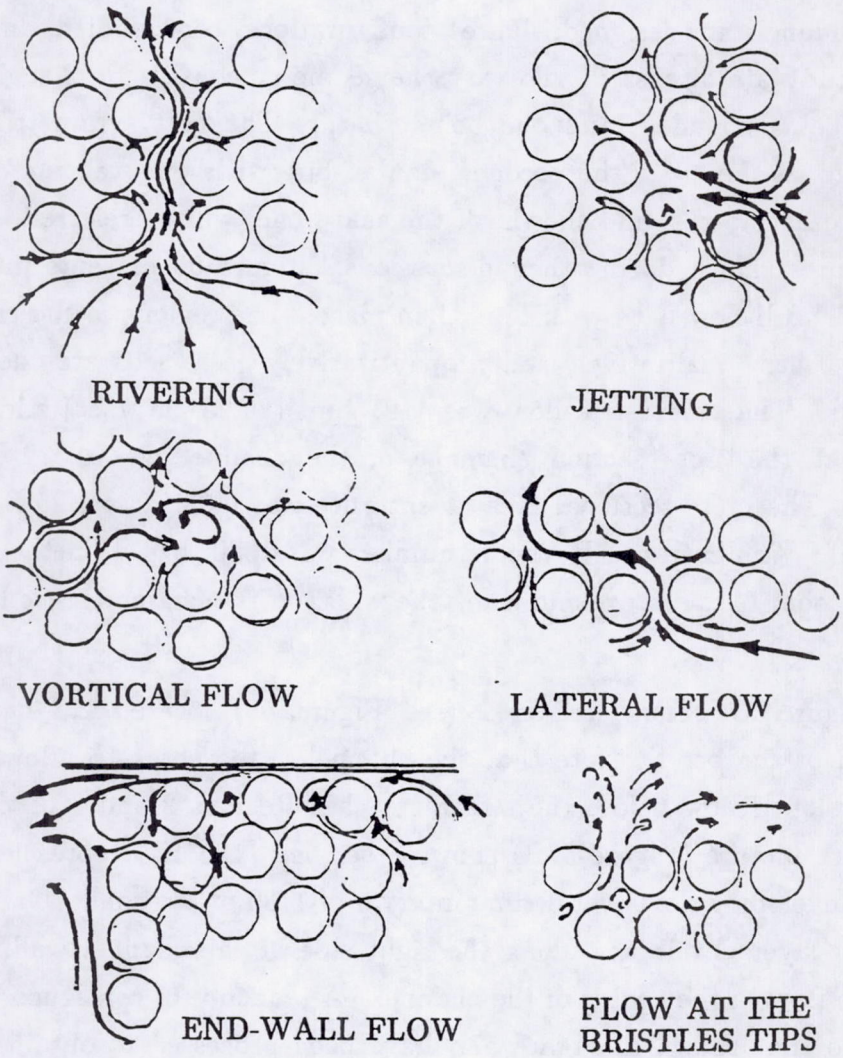



Figure 55: Sketches of Typical Flow Formations Found in Brush Seals

## 5.3 Visualization of Flows Through Cowl Lip 180° Cooling Channels

To cool hypersonic aircraft leading edge engine cowls, recirculating flow cooling channels are designed. Three configurations were studied, and the results of each study are discussed. To vary the geometry consists of changing the inner lip, two being rounded, and one being sharp. The first symmetric lip will be referred to as Lip #1, the second, similar but with one varying side, will be referred to as Lip #2, and the third, the sharp one, will be referred to as Lip #3, in all figures shown during their discussions. Figure 56 presents in detail a top view of the full flow path with Lip #1 in place. The regions of the channel where the flow was qualitatively and quantitatively assessed are described and numbered. The volumetric flow was 1.42 gpm (89.95 $cm^3$/sec) and the average velocity at the cross section entrance of the channel was 0.572 ft/sec (17.43 cm/sec). The cross sectional area at entrance was 0.63 in. x 1.25 in. (1.60 cm x 3.175 cm). The entrance Reynolds number was 1380, based on the properties of water at room temperature and using the width as the characteristic length.

Figure 57 shows Region 1 (see Figure 56) located 2.2 cm (0.866 in.) upstream of the bend. Note that the channel is too short to allow the onset of fully developed flow before the stream reaches Regions 2 and 3 of the 180° bend. The insert picture (Figure 57B) shows a strobed (120 Hz) representation of this steady, developing flow over a time interval of 1/30 of a second. One can notice a boundary layer developing along the right side of the channel wall, and inviscid slug type flow in the center of the channel. A sequence of contiguous photographs similar to that shown in Figure 57B have been processed to obtain the digitized version of the flow shown in Figure 57A. An external strobe, explained in detail in Chapters 3 and 4, allowed particle motion sampling at 120 Hz frequency which produced four traces of the target particle. Figure 57A shows, at scale, velocities calculated at two cross sections of Region 1. Figure 58 shows additional digitized trajectories enlarged to further illustrate the flow in Region 1. This figure indicates that the velocity near the center of the channel is higher (longer arrows) than the velocity near the side walls.

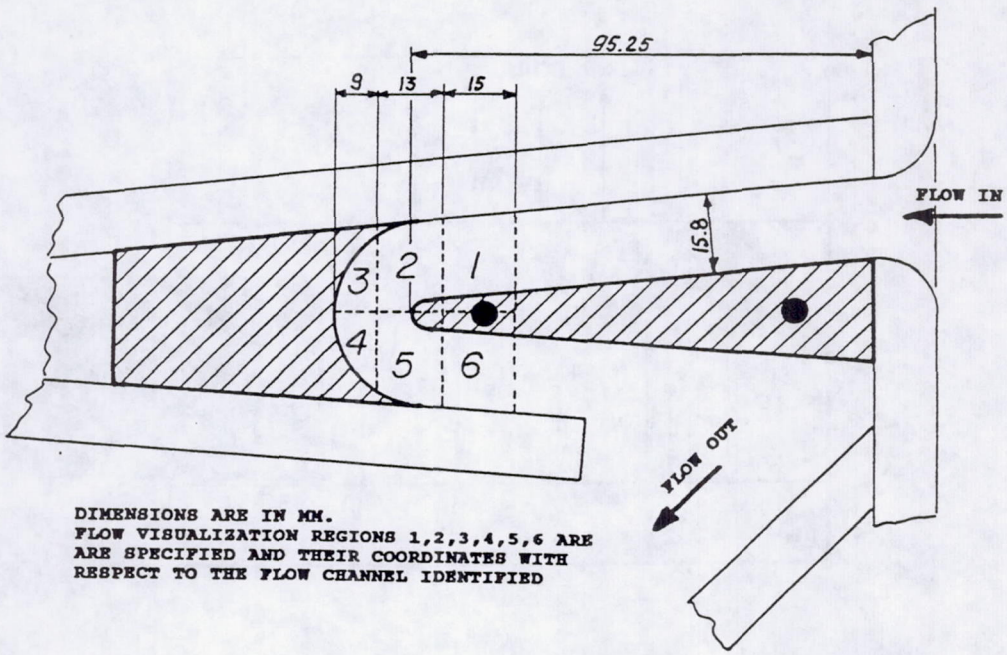



Figure 56: Geometry of Flow Path Using Lip #1

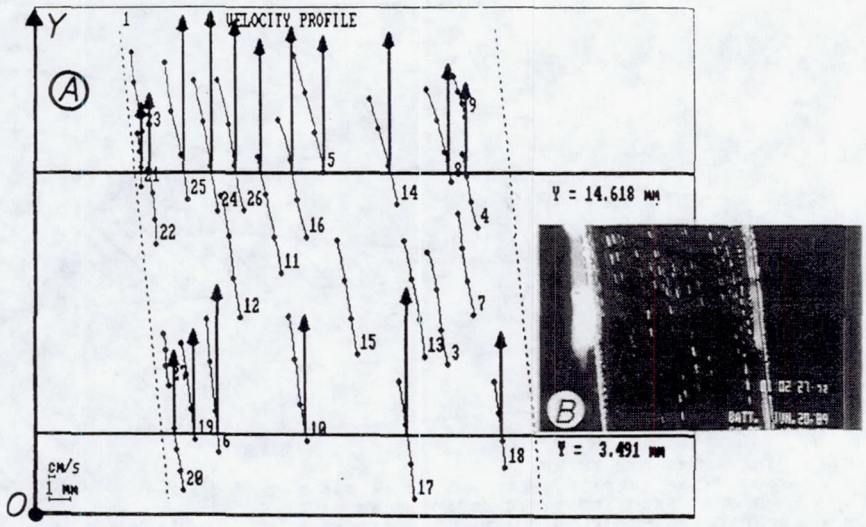



Figure 57: Flow Trajectories for Region 1
A) Quantified Flow Velocities
B) Visualized Flow Trajectories

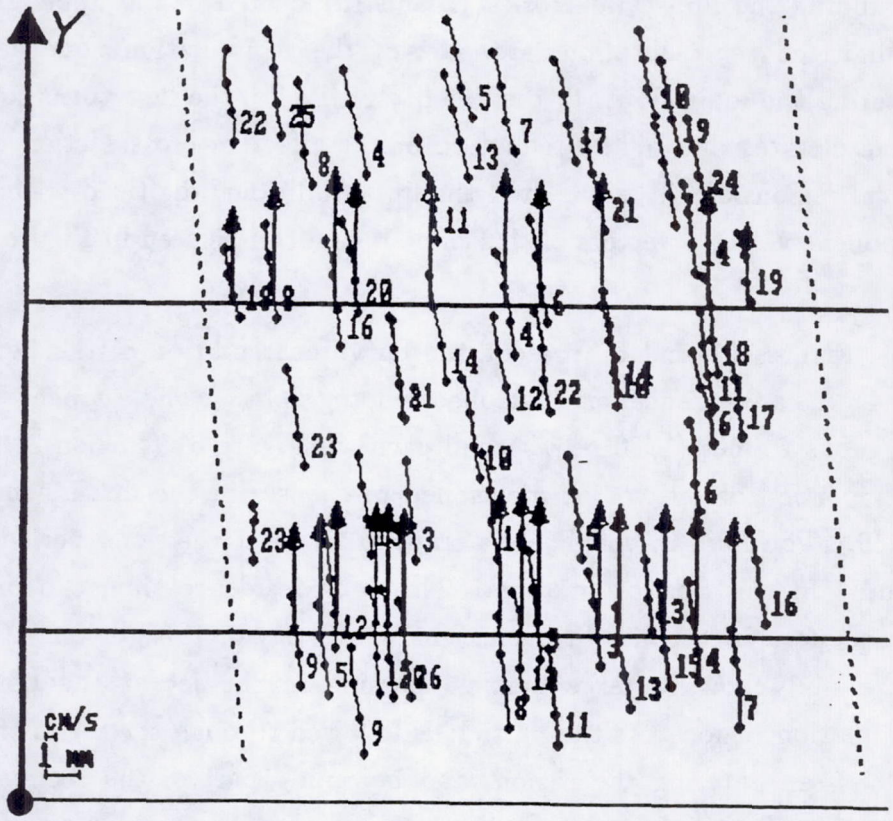



Figure 58: Additional Quantified Flow Trajectories and Velocities for Region 1

Figure 59 presents a photograph of flow during 1/30 second of time in Region 2 while the laser light has been strobed to 240 Hz producing eight traces of the target particles. Two separation and recirculation zones with vortical flows can be found in the upper right corner and in the vicinity of the lip between Regions 3 and 5 by examining the insert photograph. The digitized trajectories in Figure 59 present the X and Y velocity component profiles in the region surrounding the lip. Trajectories 12 and 13, located in the upper right corner of the digitized representation, are part of the recirculation zone and are shown reentering the main flow. In the vicinity of the lip, the flow turns towards the left and accelerates due to the reduction of the effective cross section caused by the vortical regions above and behind the lip. Additional digitized trajectories and Y-component velocity vectors of this same region can be seen in Figure 60.

Figures 61 and 62 present the curvilinear portion of the bend (Regions 3 and 4) in a sequence of unstrobed photographs. The sequence of six time-contiguous frames (1/30 of a second each) in Figure 61 (Region 3) represents the upper portion of the vortex mentioned previously in the discussion of Figures 57 and 59. The fluid in this zone is trapped for relatively long periods of time (1-2 seconds) in this vortical motion. This long residence time can produce serious consequences in the heat transfer characteristics of this region. Observation of Figure 61-1 shows a large particle passing in the jet at the boundary of the recirculation region. As the particle is followed through the series of frames 2-6, it can be seen entering the region, and becoming part of the recirculation vortex. Eventually, it will be released into the jet after it remains trapped for several seconds. The sequence of three photographs (1/30 of a second each) in Figure 62 depict the jet as it passes from Regions 2 and 3, and impinges on the outer boundary of Region 4. While some of the flow can be seen to bend to the left and move downstream with the rest of the flow after impinging (frame 3), one portion of the jet feeds the vortical formations that form in region 4 (frame 1). The location of this impingement point fluctuates through an arc of approximately 15° on the outer boundary. This variation is evidenced in Figure 62 as the jet is shown impinging in three locations creating three characteristic flows each time. The flow is highly unsteady and the change in the position of this point creates

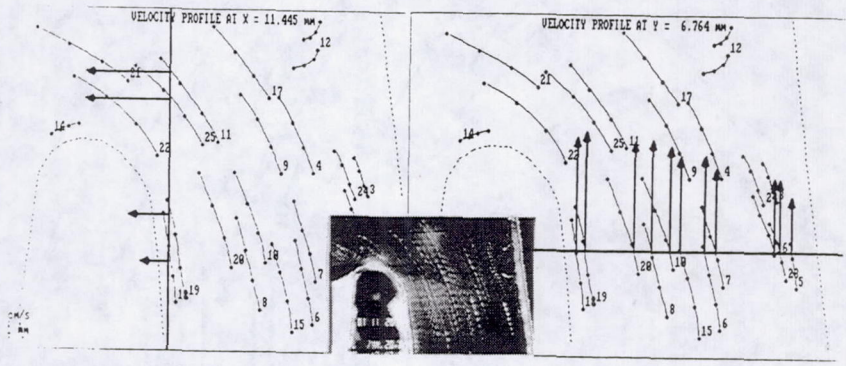



Figure 59: Quantified Flow Trajectories and Velocities for Region 2

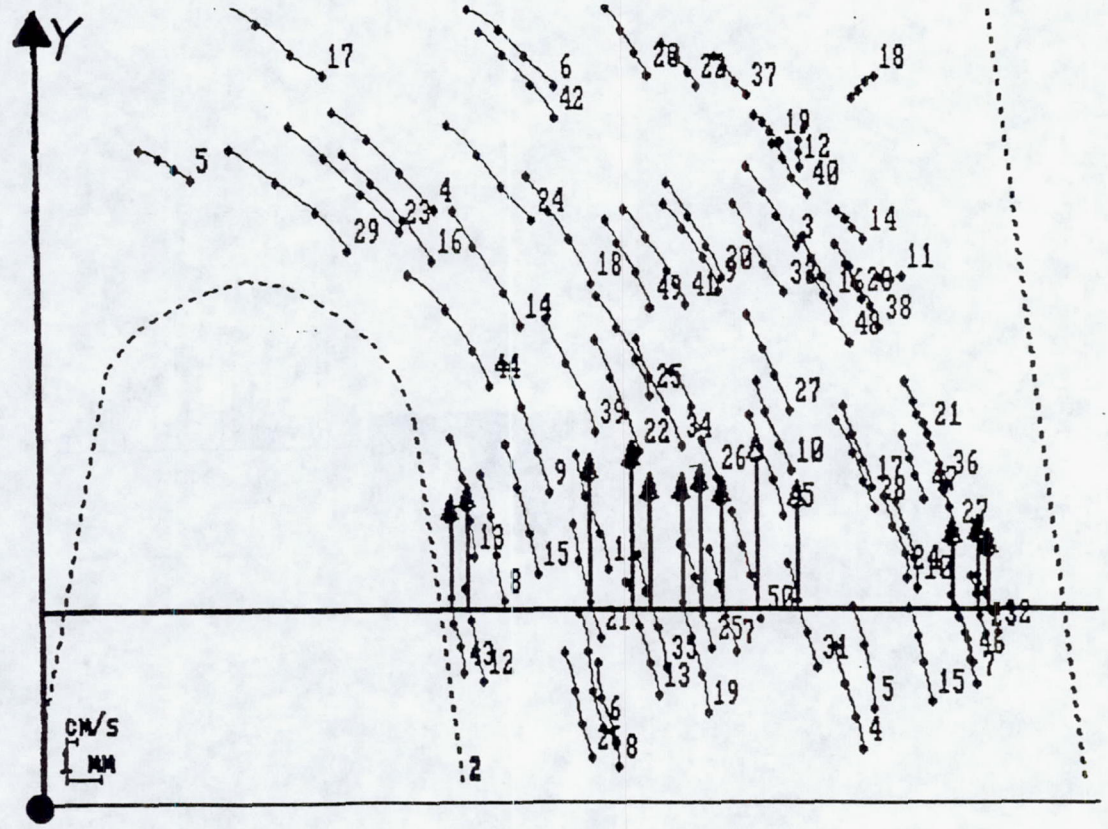



Figure 60: Additional Quantified Flow Trajectories and Velocities for Region 2

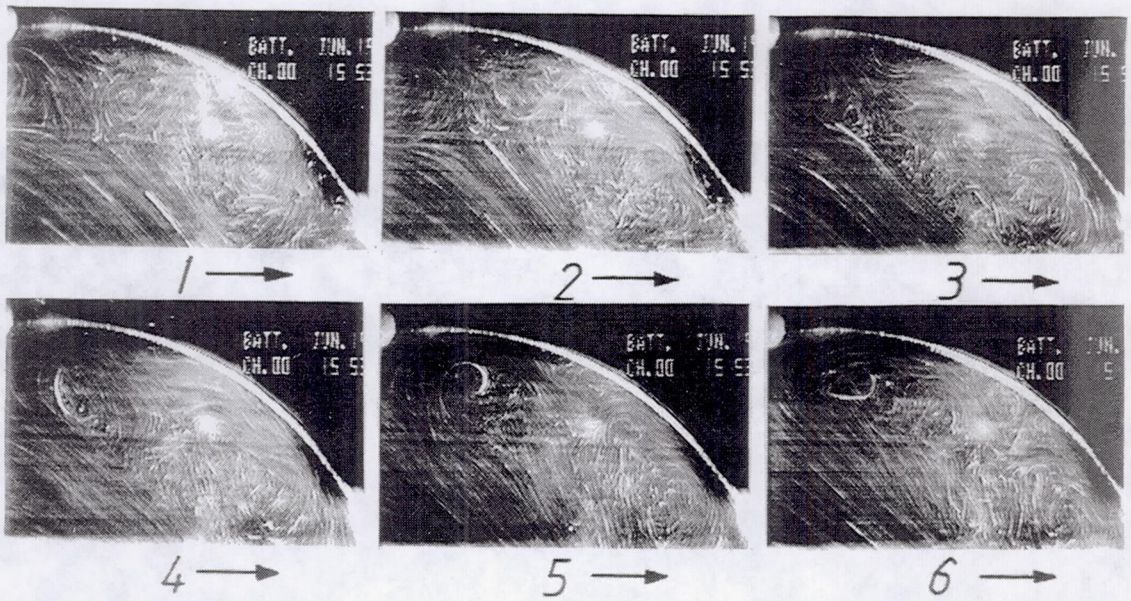



Figure 61: Photographic Sequence Illustrating Flow Occuring in Region 3

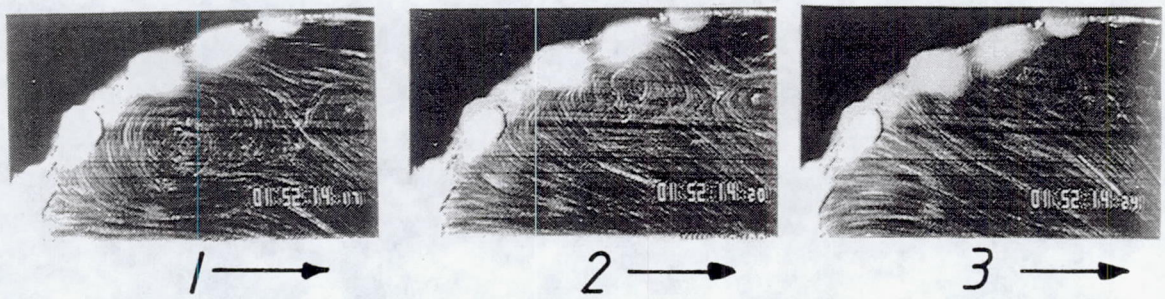



Figure 62: Photographic Sequence Illustrating Flow Occuring in Region 4

alternating source- and sink-like formations. This periodic behavior traps the fluid during the sink-like part and releases it during the source-like part of the cycle. As was the case in Region 3 (Figure 61), the time dependent flow pattern will have serious consequences for the heat transfer characteristics of the zone, as prolonged residence causes excessive heating on the outer confines of Region 4.

Figure 63 presents the flow in Region 5 after the jet hits the impingement region and splits. In this figure the region of the jet, as well as the separation zone in the vicinity of the lip, have good definition despite the horizontal light and dark areas evident (see insert photograph) that are the result of the light source being refracted by the rounded lip. In the separation zone, the flow is unsteady and the optical magnification ratio (8.47) is not large enough to chart the trajectories and velocities. The periphery of the recirculation zone is defined by a set of trajectories (3,4,5,7,9,15) for which the spatial resolution at 120 Hz was high enough. Turbulent reattachment follows at the lower portion of Region 5 (lower portion of Figure 63), and becomes more evident looking at Region 6 (Figure 64). The flow can be seen accelerating towards the exit along the outer wall, adjacent to the chaotic flow of the recirculation (lower area of Figure 64).

Using the graphics capabilities provided by the CIIQ package, Regions 1 through 6 have been assembled to obtain a composite image (Figure 65) of the entire Lip #1 cowl geometry. Since the flow in Regions 3-6 is time dependent, this composite yields largely qualitative information. However, it does represent well a time averaged behavior of the fluid in the 180 degree bend, and as such can be very useful for determining the quantitative time averaged heat transfer characteristics of this cowl lip pattern. The composite figure, and therefore the time averaged behavior of the flow through the Lip #1 geometry, was assembled after observing more than 11,250 frames of data at 25 different locations.

Alternative geometries to Lip #1 were considered. The geometry of the Lip #2 is illustrated in Figure 66. This geometry is different from the previous one (Figure 56) in that it contains a narrowing cross-section immediately upstream of the 180 degree turn. The same six regions that were identified in the

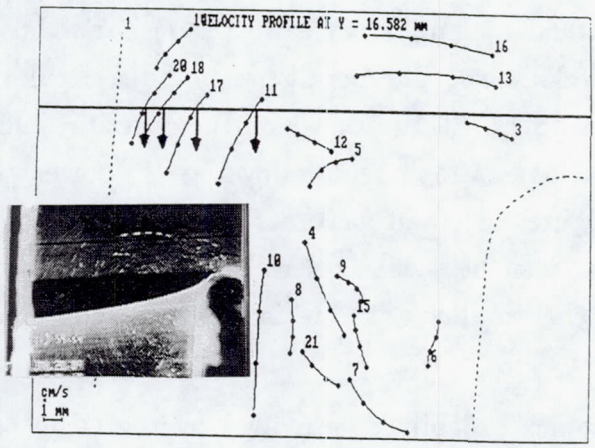



Figure 63: Quantified Flow Trajectories and Velocities for Region 5

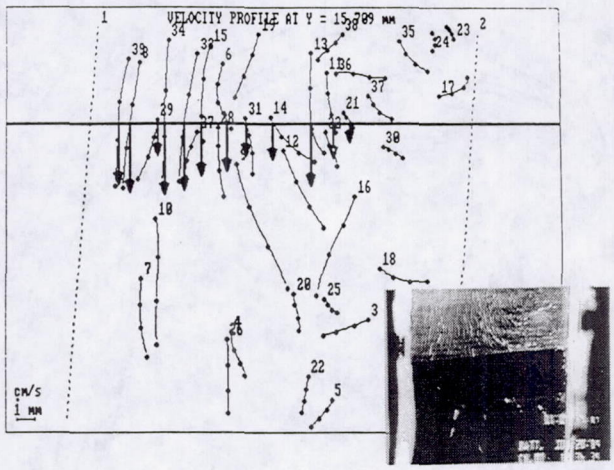



Figure 64: Quantified Flow Trajectories and Velocities for Region 6

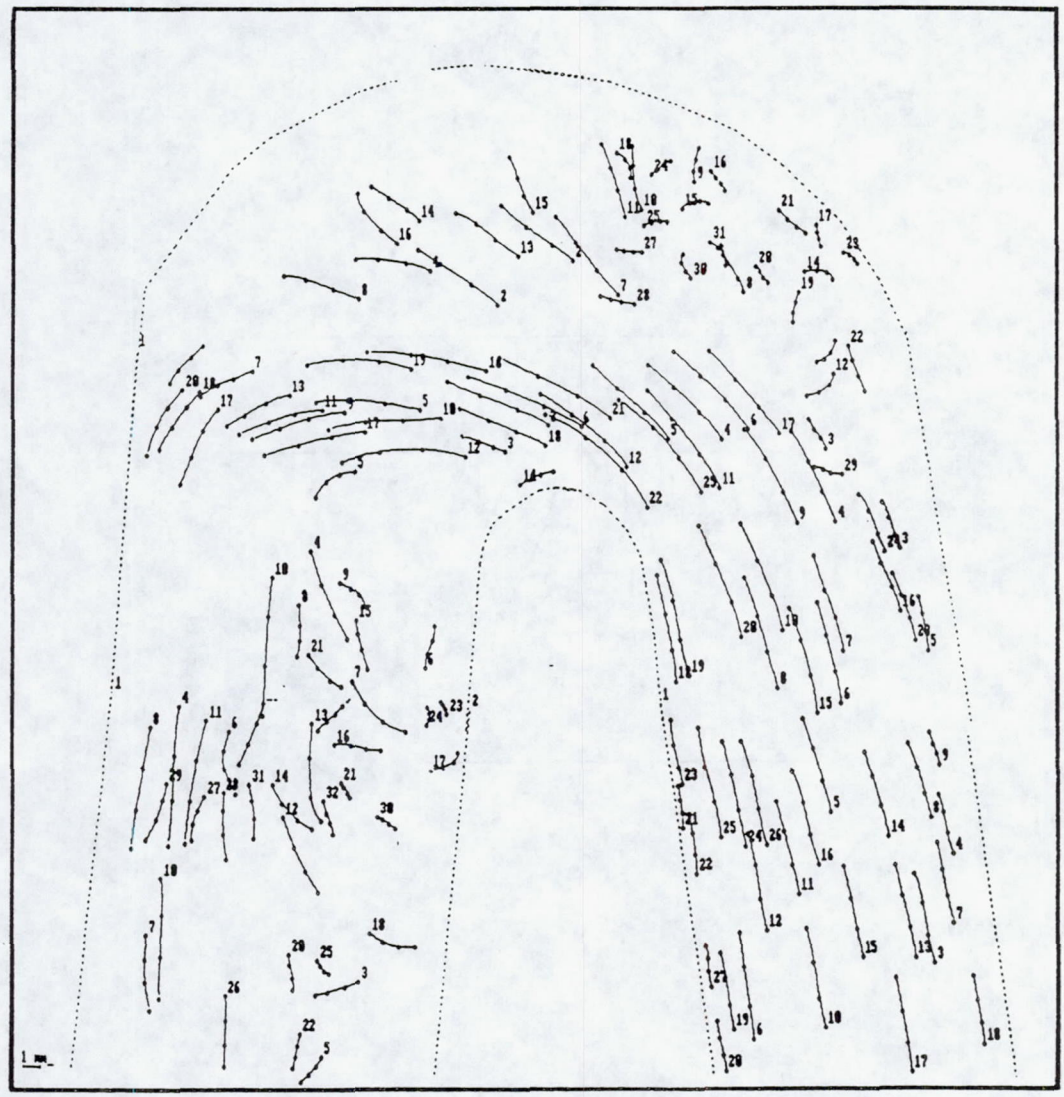


Figure 65: Composite Image of Flow Trajectories Around Lip #1 (Regions 1-6)

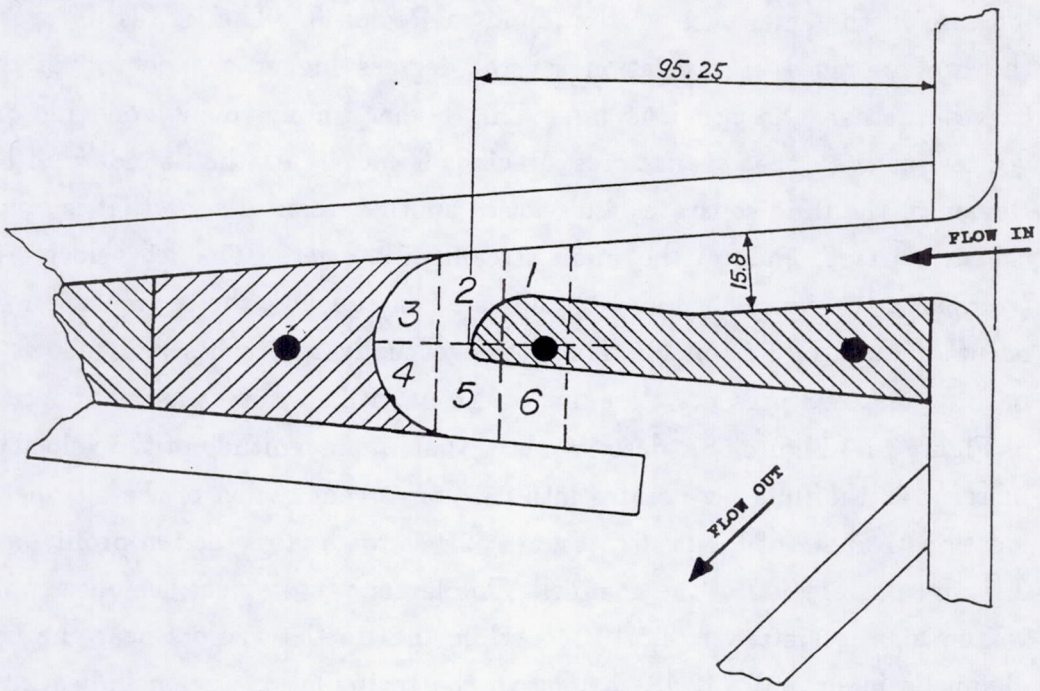



Figure 66: Geometry of Flow Path Using Lip #2

previous geometry of Lip #1 (see Figure 56) were observed around Lip #2. For comparative reasons, the flow rate used was identical to that used for the experiments around Lip #1, 1.42 gpm (89.95 $cm^3$/sec). For reasons of brevity, only the quantified composite flow picture is presented. Included in Figure 67 are the corresponding photographic details of the right (Regions 2 and 3) and left (Regions 4 and 5) regions of curved boundary. The narrowing cross section causes an increase in the main stream velocity immediately before the 180 degree turn, and is accompanied by a pronounced 'vena contracta' effect that engenders an increase in the small size vortex found in Region 3. The jet, as it turns around the lip, impinges in a location several degrees higher on the top of the outer curvature than the previous lip. This higher impingement zone increased the vortical activity that spans across Regions 3 and 4. At the boundary of the lip in Region 5, the fluid separates and causes another vortical zone that is bounded by the lip surface, and by the main stream of the jet. The jet velocity is larger (compared to Figure 65, Lip #1) and as a consequence, the recirculation zone now occupies most of Region 6. The flow eventually reattaches and follows the exit path. Figure 68 presents close-ups of the quantified flow velocity at locations 1-3 of Figure 67. Figure 68A describes how that the magnitude of the velocity vectors increase as the fluid accelerates into the convergent region of the channel through locations 1 and 2 of Figure 67. Figure 68B shows a cross section profile at location 3 in the exit portion of the channel. The larger vectors near the outer wall belong to the main jet stream (4,5,10,14), while the smaller vectors near the lip on the channel's inner wall (12,18) belong to the recirculation region indicating smaller magnitudes, and flow reversal within the vortex.

Figure 69 presents the channel configuration of the sharp edged Lip #3. This geometry differs from that of Lip #1 and Lip #2 not only because the lip has sharp edge, but also since the curved upper boundary has been removed. Figure 70A shows the flow around Lip 3 in a start-up mode with the lower mass flow of 0.5 gpm ($3.154 \times 10^{-5} m^3$/sec, 1.116 $ft^3$/sec). The formation of the jet, its separation, and a slowly moving vortical region (bounded by the lip and the main stream) is evident. As the mass flow is increased to 1.0 gpm ($6.308 \times 10^{-5} m^3$/sec; $2.23 \times 10^{-3} ft^3$/sec), the separation region and recirculation zones

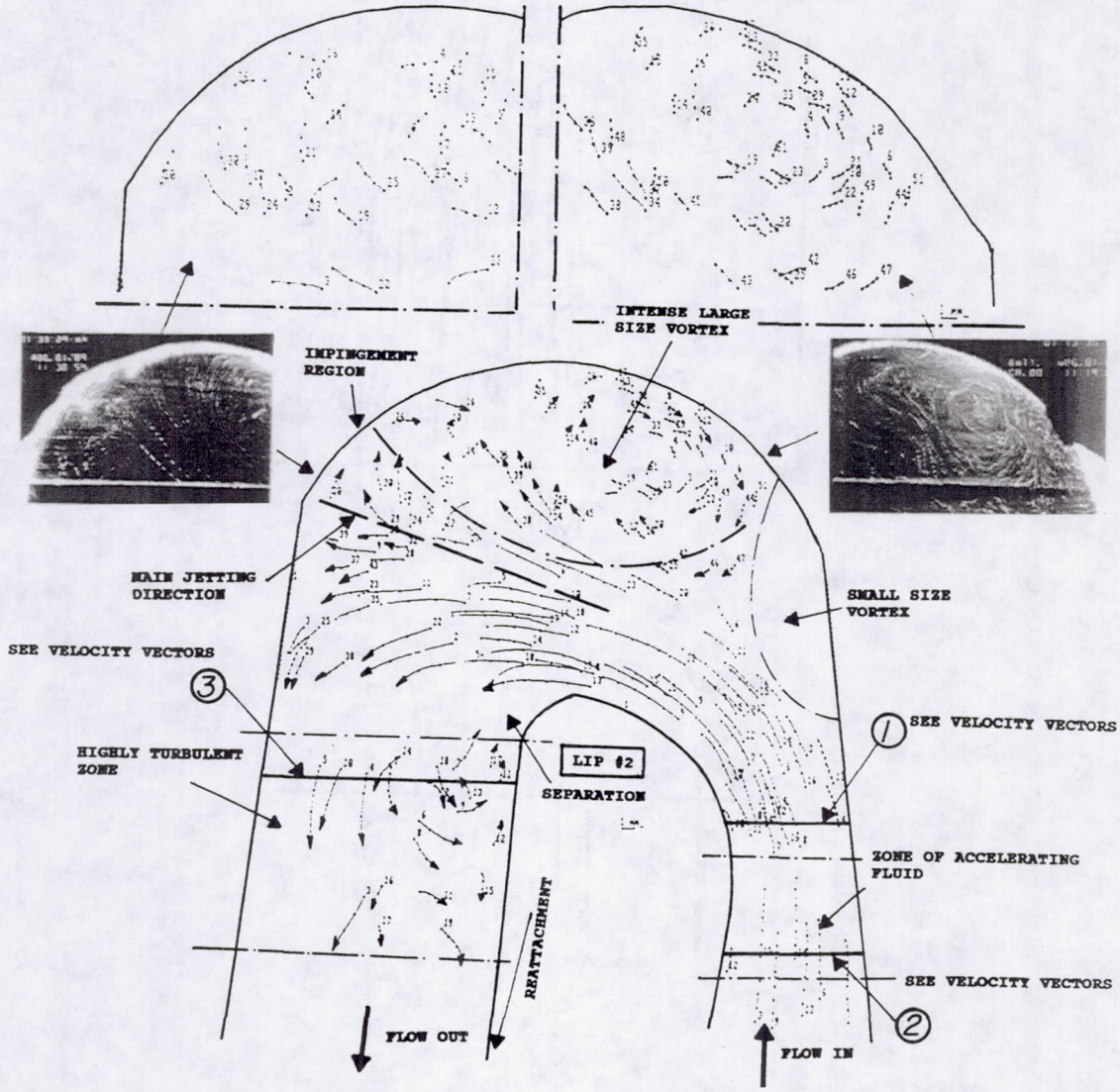



Figure 67: Composite Image of Flow Trajectories Around Lip #2 (Regions 1-6)

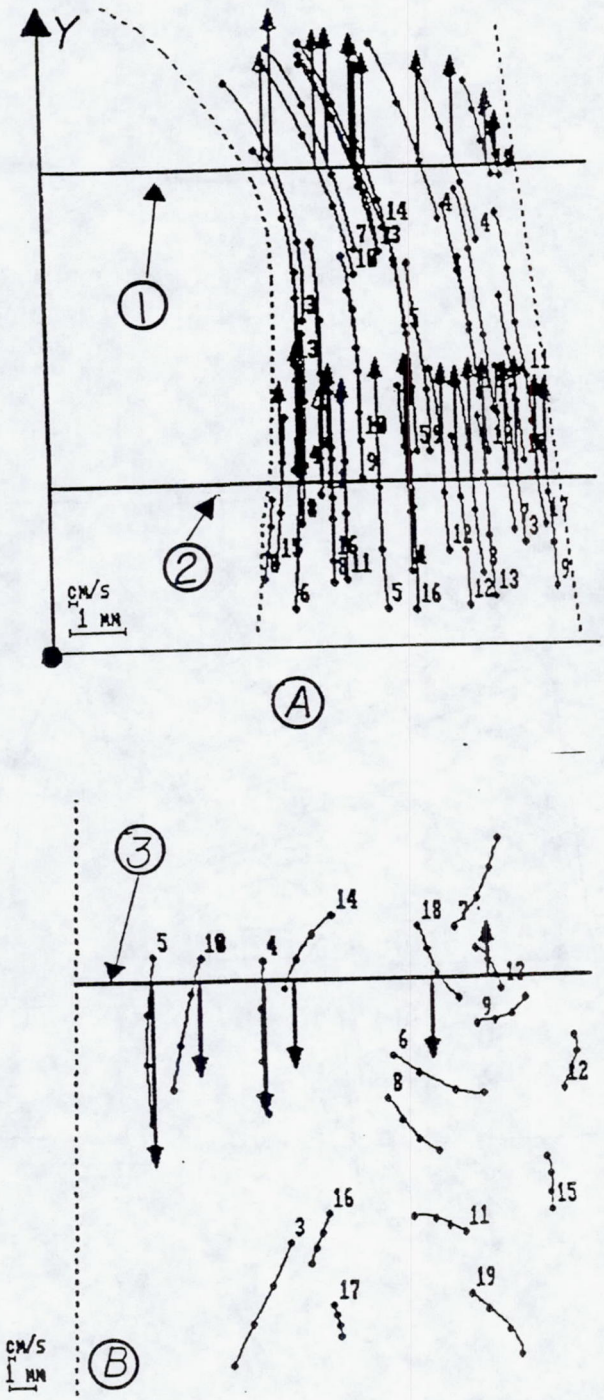



Figure 68: Quantified Flow Trajectories and Velocities
A) for Region 2
B) for Region 5

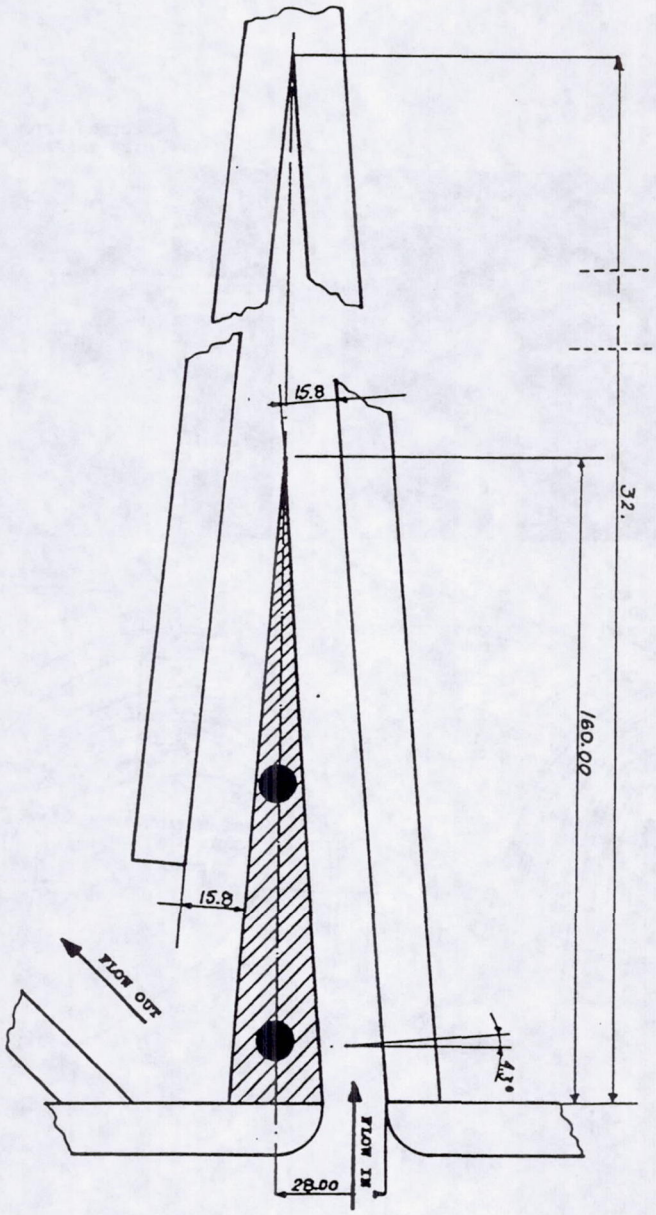



Figure 69: Geometry of Flow Path Using Lip #3

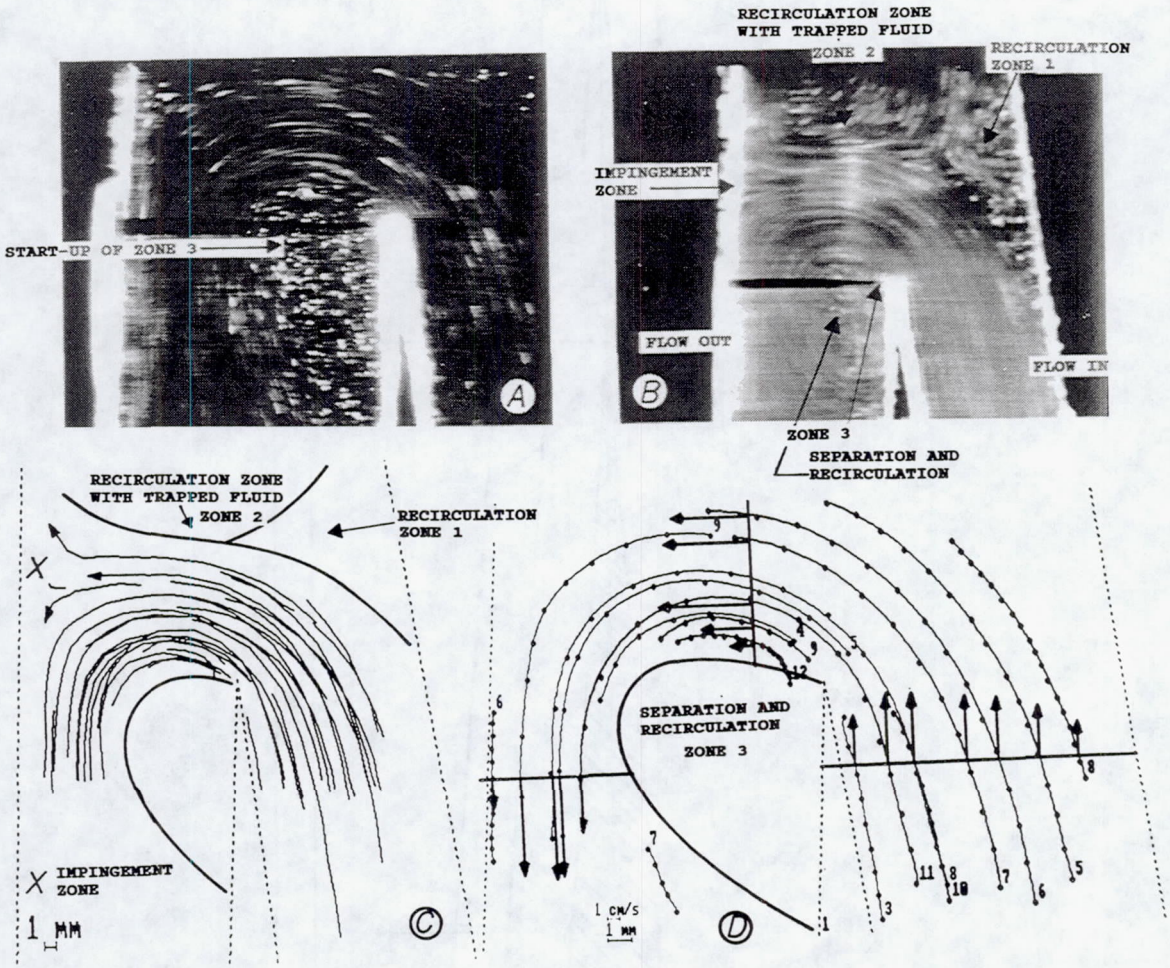



Figure 70: Composite Images of Flow Trajectories Around Sharp Edged Lip #3
A) Visualized Image of Low Flow Rate Around Lip #3 Apex
B) Visualized Image of High Flow Rate Around Lip #3 Apex
C) Digitized Flow Trajectories for High Flow Rate (Figure 70B)
D) Quantified Flow Trajectories and Velocities Around Lip #3 Apex for High Flow Rate (Figure 70B)

observed in Figure 70A grow into the well developed Zones 1-3 as seen in Figures 70B and 70C. Zone 1 forms to the right of the jet stream, and is confined by the outer boundary of the jet, and larger vortex of Zone 2. Zone 2 covers a region of rather intense recirculation, but the fluid in this zone gets trapped between the apex of the triangular outer boundary and the upper split of the jet. The lower split forms a free flowing new jet-stream that proceeds towards the exit of the channel. Comparison of the flow patterns in Figure 70 to those of the previous lips (Figures 65 and 67) yields that this lower split of the jet stream is similar. The flow pattern created by Lip #3 contains separation and recirculation areas (Zone 3-Figure 70B) that can also be seen in Regions 5 and 6 of the two previous lips (Figures 65 and 67) discussed. The digitized version of Figure 70B shows the flow trajectories and the jet impingement zone, X, in Figure 70C. The flow velocities at various cross sections of the channel, Figure 70D, were then calculated. The difference between the three lips is the increase in flow in the curvilinear Regions 3 and 4 of the Lip #2 geometry. The increase in fluid exchange between the vortices in Regions 3 and 4 and the free stream result in higher heat transfer, making Lip #2 the recommended choice.

## 5.4 Visualization of Flows Through Staggered Pins in a Branched Duct

The testing in the branched duct was started as part of a program to verify the accuracy of a numerical analysis code written to study the heat transfer and fluid dynamics of flows through internally cooled high temperature turbine blades. A typical blade describing the path of the air is shown in Figure 71. The staggered pin/branched duct geometry (see Figures 9-11) was designed to obtain baseline experimental data to verify the numerical results. The staggered pins are located on the right side of a branched duct connected to a vacuum exhaust tunnel and operated at an air free stream velocity of 30 ft/sec. The region of interest is illustrated in Figure 11, and is further indicated by the cross-etching of the pins in the first two rows. The FFFT/CIIQ method was applied to acquire the data as air entering the bellmouth of the tunnel (see Figure 9) was seeded with luminous particles.

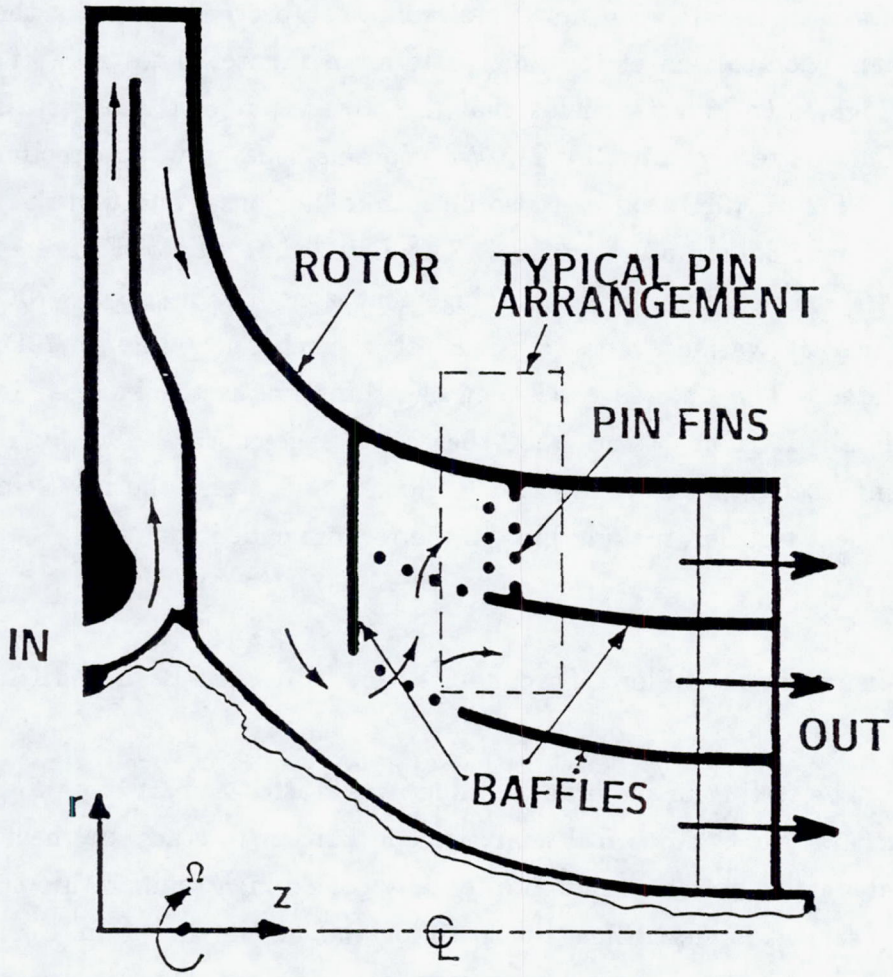



Figure 71: Typical Internally Cooled Turbine Blade

The purpose of this portion of the thesis is the qualitative and quantitative investigation of the flow field upstream and within the first two rows of pins. Many hours of investigation were spent determining the proper seed particle to use for this application (see Section 3.5 and Chapter 6) and two are discussed here. The flow field was surveyed from the central partition dividing the sides of the channel to the right side wall, including the areas around and between each pin located in the first and second rows. A composite image of the flow was obtained by digitizing smaller regions of the first few rows, obtaining the flow trajectories and velocities in each of these regions, and then assembling these images to obtain the final global image. The first seed particle used was Cabosil powder, and its composite digitized flow representation is illustrated in Figure 72.

As evidenced in the digitized global representation describing this flow (Figure 72), the unobstructed left side of the test section causes the flow direction to strongly deviate from the longitudinal axis of the channel, and become skewed in the region of the first row, particularly in the area of Pins 1-3. When compared with the first row, it appears that the skew of the flow in the second row has decreased due to the straightening effect produced by the first row of pins. The assembled images show that the unobstructed branch skews the flow and shifts the stagnation points of Pins 1, 2, 3, 6, and 7 to the right. The skew of the flow diminishes considerably towards the side wall, and in the regions around Pins 4, 5, and 9 the flow is practically parallel with the side wall. This change in flow direction can be observed in detail in Figure 73. The flow around Pins 1, 3, and 5 is presented with velocity vectors at a variety of cross sections in the longitudinal direction. Figure 73 has been obtained using the FFFT method and CIIQ programs discussed in Chapters 3 and 4. The axial vector components of these velocities can be seen at Sections A,B,C,D of each of the pins, and as in Figure 72, the straightening of the flow and the stagnation points from Pins 1-5 can again be clearly evidenced.

Thus far, the trajectories of both the particles that follow the flow, as well as those that are controlled by their own inertia and do not describe the flow, are shown as they pass through the first two rows of pins. Particles that impact and

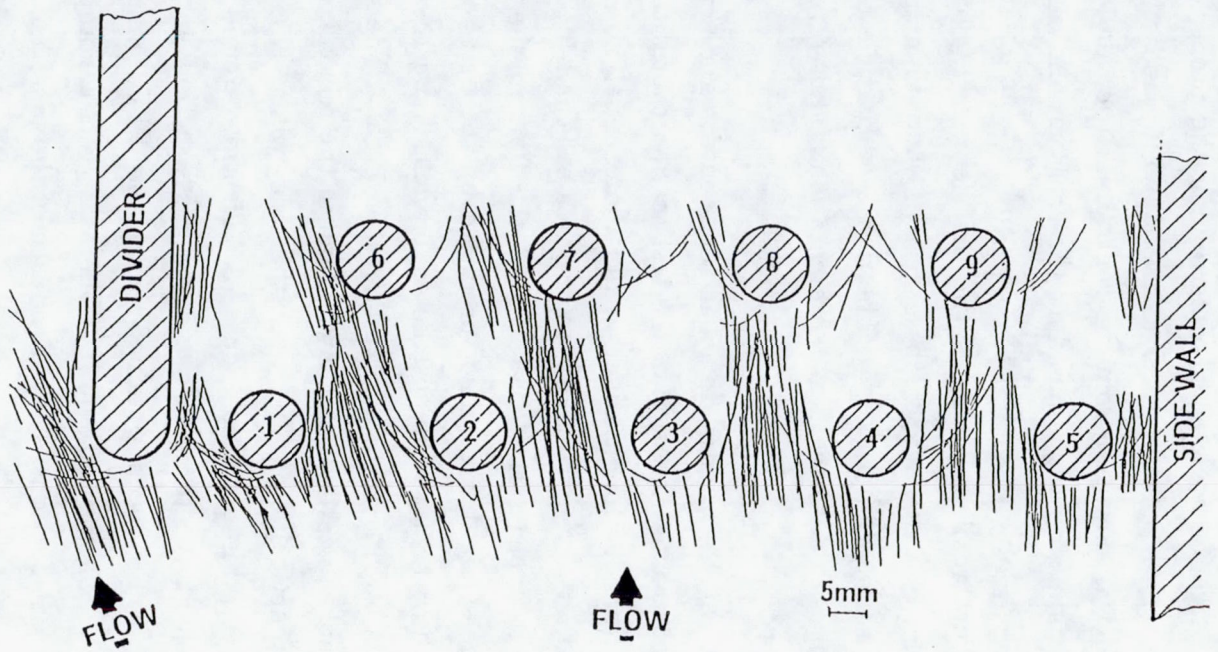



Figure 72: Digitized Flow Trajectories for First Two Rows of the Staggered Pin Geometry Using Cabosil as the Seed Particles

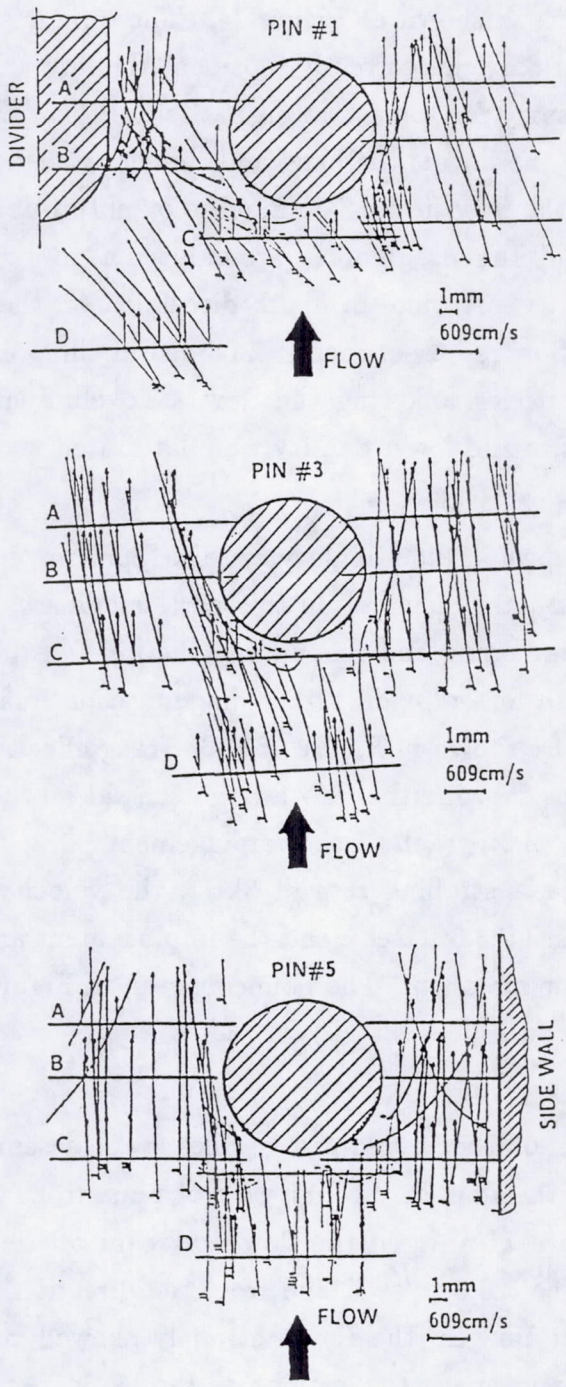



Figure 73: Quantified Trajectories and Velocities for Flow Around Pins 1,3, and 5 Using Cabosil as the Seed Particles

rebound are evidenced in the digitized representations of Figures 72 and 73, and again in the photograph shown as Figure 74. These figures raised the question of whether the Cabosil particles correctly represent the flow in the pinned area. The response time necessary for some Cabosil particles in this flow regime to properly react and represent the flow is too long, and therefore they crash into the pins and rebound back into the flow field. Too much momentum is created by the density of the particles and the drag forces around them to react quickly enough to changes in the airflow. A more in depth discussion on the principles of response time and accurate flow representation is included in Chapter 6 which discusses the accuracy of the particles following the flow. To eliminate this problem, latex spheres of smaller size and lower density were later used.

Figure 75 shows a wide angle view of a portion of the pin section of the channel seeded with latex spheres. In this particular view, there is no evidence of the latex spheres impacting and rebounding the pins. Additional extension rings added to the camera lens provide higher magnification images of the flow around the partition, and are shown in Figure 76. The magnification factors are 12.27 for the two photographs showing the flow around the sides of the partition (top), and 36 for the detailed photograph of the impingement point (bottom). The images were recorded using a strobing rate of 3kHz, the velocity of the flow for these images was 7.1 m/sec (23.3 ft/sec), and the impingement angle was approximately 45° off the main flow direction. The bouncing seen in Figure 74 is not apparent in either of these figures.

Photographs of the stored image files were assembled to yield a time-averaged image of the flow in the first row of pins, from the channel position to the side wall, Figure 77. Again the flow upstream of the pins was steady, at a velocity of 7.1 m/sec (23.3 ft/sec), and from the direction indicated in the figure. As with the earlier images, the flow's strongly skewed pattern in the partition region is evident, and spans the regions of Pins 1-3. As the distance from the partition increases, the flow gradually straightens, and the stagnation point moves clockwise from 25° for Pin 1 to 0° at Pins 4 and 5. The flow remained steady as it reached the pin area, and no fluctuations or oscillations were observed in front of

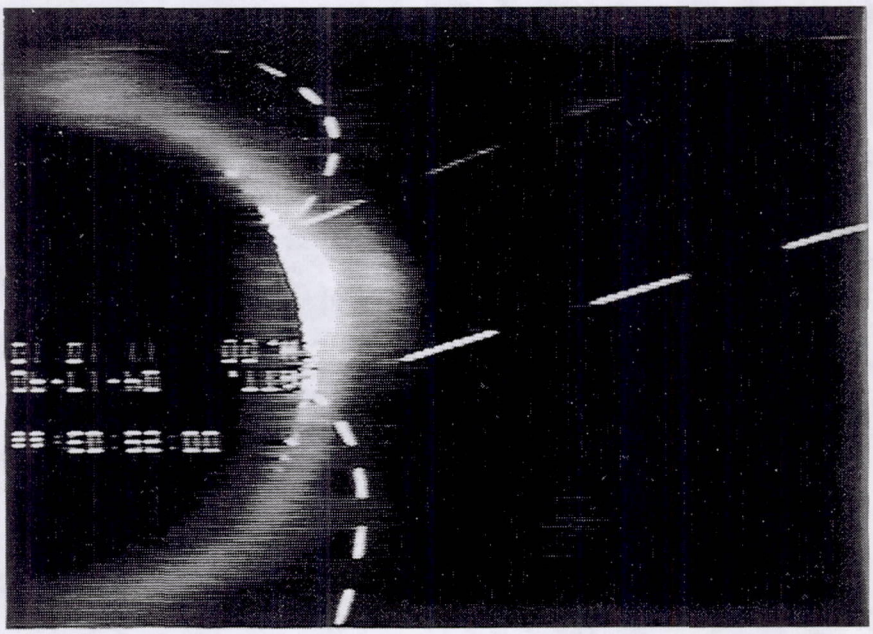


Figure 74: Photograph Illustrating Impacting and Rebounding Cabosil Particles

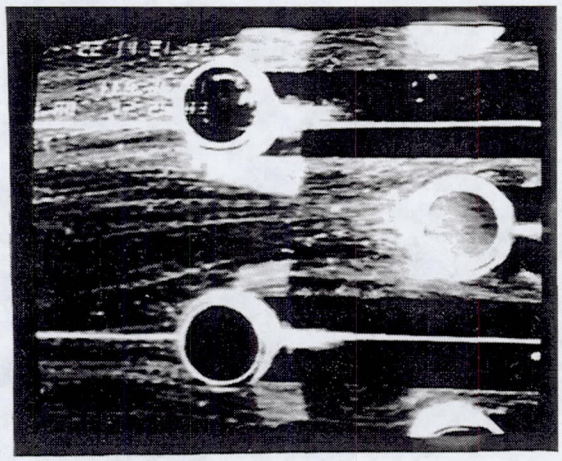


Figure 75: Photograph Illustrating Flow Through the Staggered Pin Geometry Using Latex Spheres as the Seed Particles

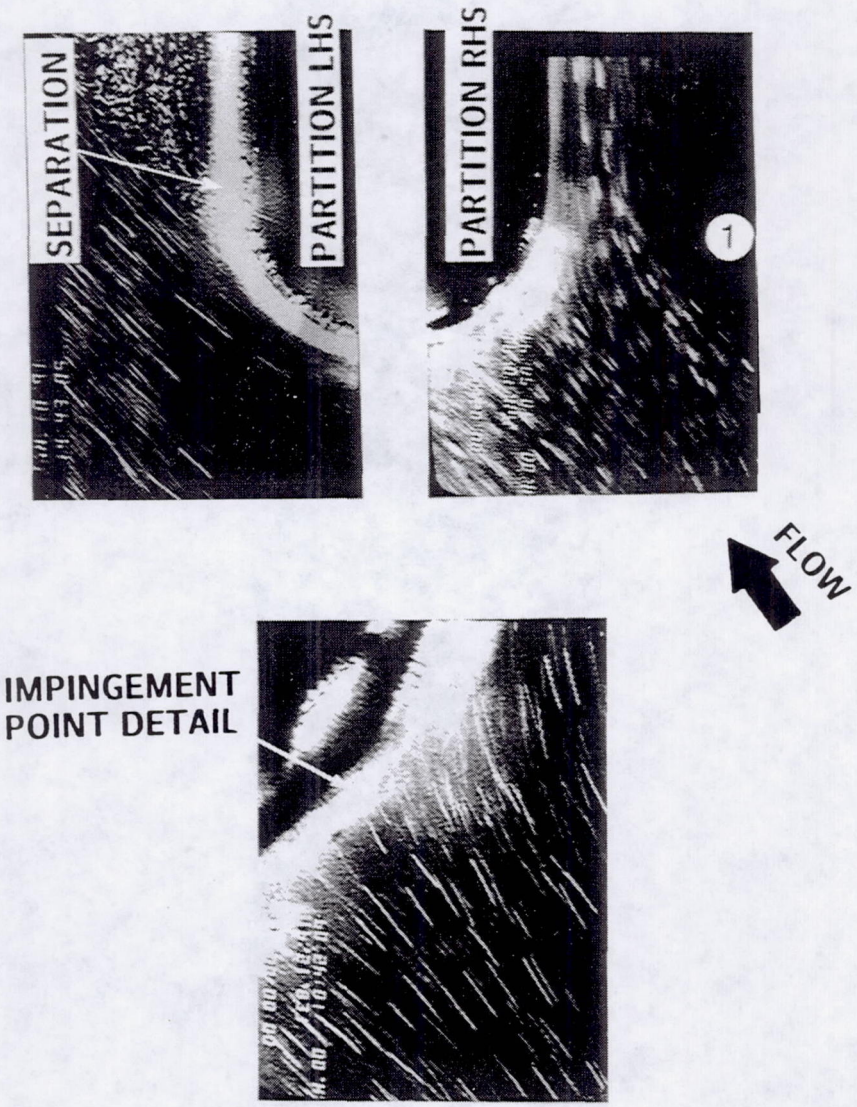



Figure 76: Photographs Illustrating Flow Around the Partition Using Latex Spheres as the Seed Particles (note lack of bouncing)

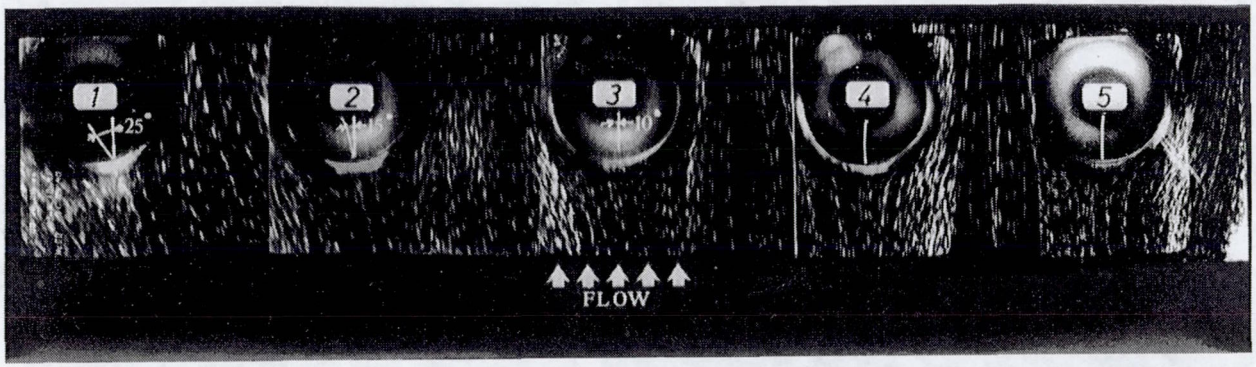



Figure 77: Photographic Montage of Flow Through the First Row of the Staggered Pin Geometry Using Latex Spheres as the Seed Particles

or between the pins. This photographic montage, as with Figure 76, shows no sign of the seed particle rebounding illustrated in Figure 74. This important point will be discussed in greater detail below, and again in Chapter 6.

The photographic composite flow pattern presented in Figure 77 has been digitized by means of the FFFT/CIIQ method (Chapter 4). The composite digitized image was obtained first by indexing the regions of the first row, obtaining flow trajectories and velocities in individually indexed windows, and then assembling these windows by means of a CAD package to obtain the final image. The final result is presented in Figure 78, and it offers a good look at the flow trajectories around the first and second rows of pins, around the partition, and upstream 38 mm (1.5 in.) of the first row. This offers a clear description of the flow approaching and passing through the pin area, without the presence of non-representative (bouncing) particles shown previously in Figure 72.

The velocities of the flow trajectories contained in the Windows A through F in Figure 78 are shown in Figure 79. The velocity magnitudes were obtained through the CIIQ algorithm (Chapter 4), and the components in the y-direction of the absolute velocity vectors are drawn at the indicated scale for all marked windows. The flow upstream of the pins is steady, and without fluctuations, and further inspection of the velocity vectors of Windows B, D, and F reveals that the upstream flow velocity is nearly constant in magnitude across the entire cross section. The magnitude of the flow velocities, as well as the projected point of impact with the pins, are visible from the details contained in the Windows A, C, and E of Figure 79. The skewing of the flow towards the partition is again shown, as the impingement angles are again illustrated. The flow between the pins takes the shape of a jet passing through a restricting inlet. These jets do not merge or become unstable between the first and second rows, and are separated by the wakes that form in the back of the cylinders (see Figure 80).

Illumination of the test section from the side of the channel (see Figure 9) allows imaging of the area between the rows, and enables the visualization and qualitative presentation of the wakes that are formed behind the pins. Figure 80

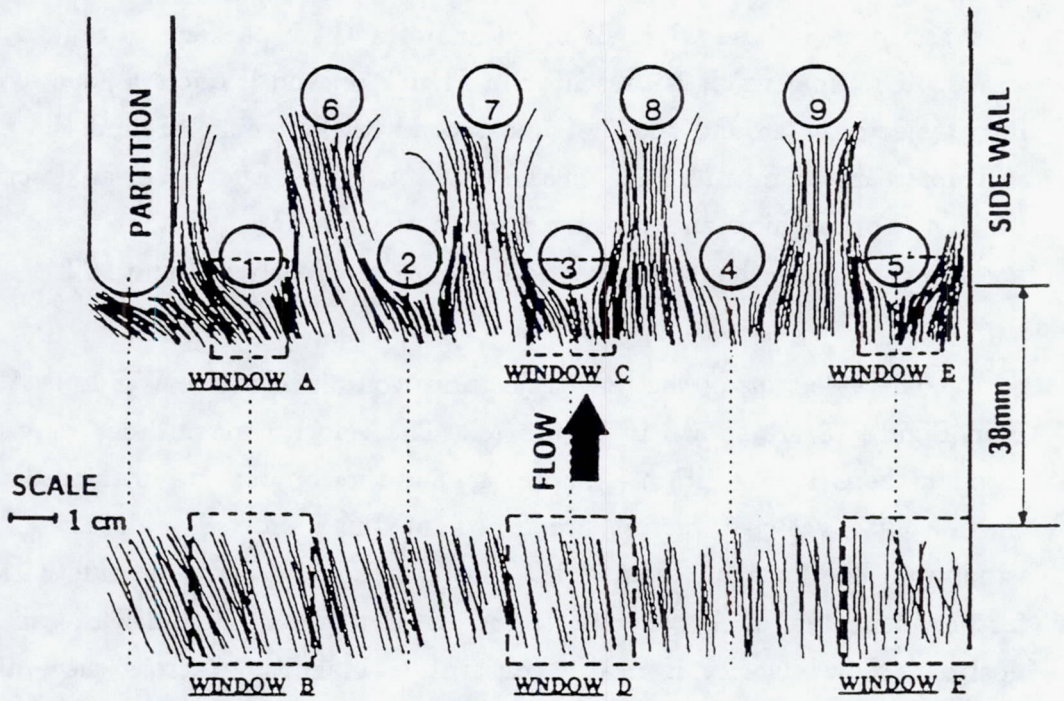



Figure 78: Digitized Flow Trajectories for First Two Rows and Upstream of the Staggered Pin Geometry Using Latex Spheres as the Seed Particles

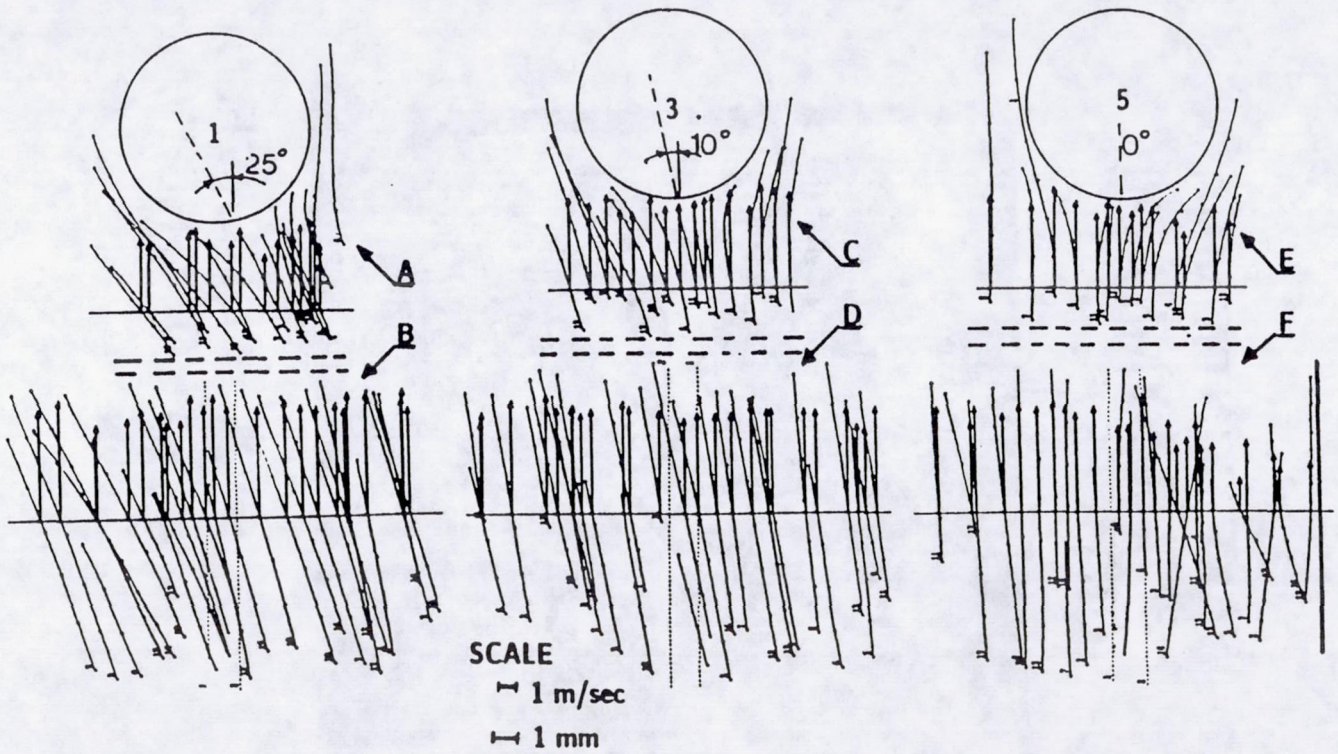



Figure 79: Quantified Trajectories and Velocities for Flow Around and Upstream of Pins 1,3, and 5 Using Latex Spheres as the Seed Particles

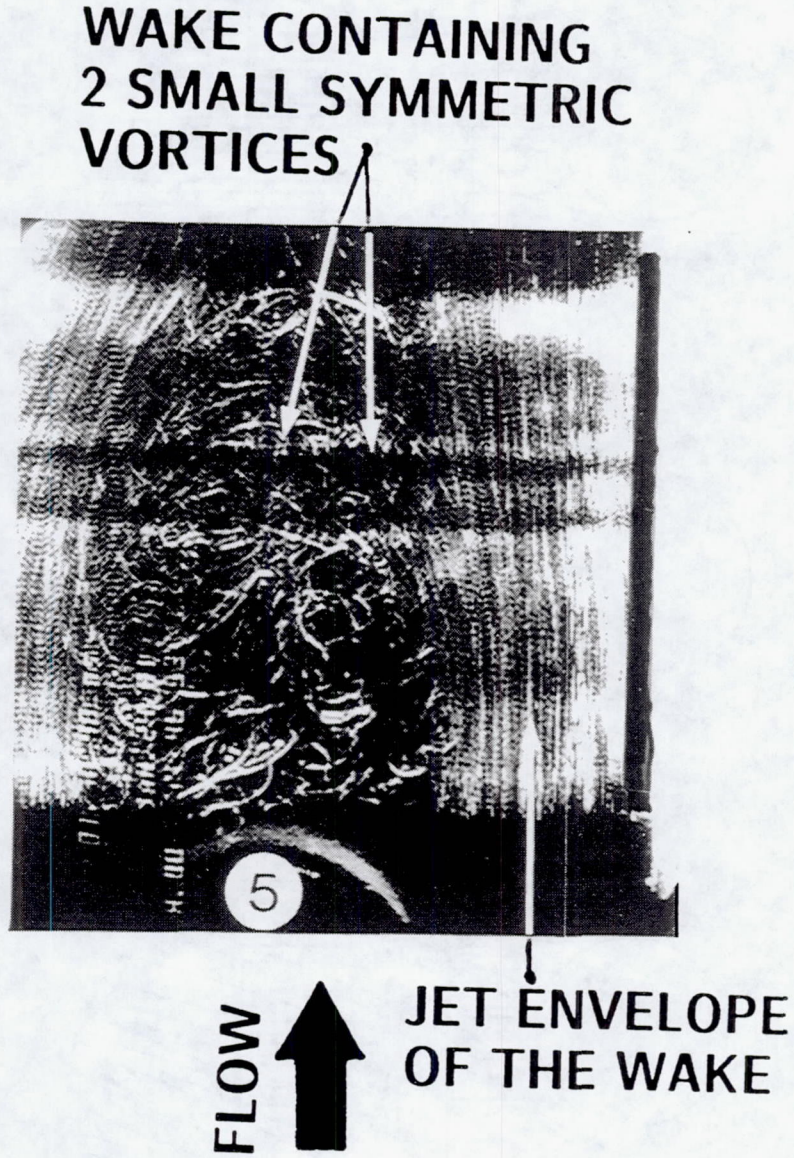



Figure 80: Visualization of the Flow Trajectories in the Wake of Pin 5 Using Latex Spheres as the Seed Particles

presents such a typical wake that consists of two stable small vortices bounded by the envelopes of the jet flow. The external flow envelope closes immediately behind these discrete vortices with no further evidence of turbulence in this area. The digitized flow patterns between the two rows (see Figure 78) indicates that the wakes behind the cylinders are of limited extent and actually close before reaching the second row allowing the reformation of the jets between the pins of the second row. A considerable straightening of the flow is also noticed as the flow emerges from the first row and reaches the second row of pins.

The results using the two seed particles were compared, yielding the following conclusions. The larger diameters (maximum sizes of 15 $\mu$m compared to 4 $\mu$m) and higher mass (1800 kg/m$^3$ compared to 1055 kg/m$^3$) of the Cabosil particles prohibit them from overcoming their inertial forces causing the characteristic bouncing shown in Figures 72-74. Alternately, in Figures 75-80, there is no evidence of the latex spheres bouncing. However, the latex particles **do** impact the staggered pins, but that their hollow nature and elastic material properties prohibit them from rebounding back into the flow. While the 'heavier' Cabosil particles impact and rebound, the lighter and generally smaller latex spheres also impinge but disintegrate on impact. This gives the **appearance** in the recorded images that they do not impact the pins. This phenomena can be assigned a value known as the Coefficient of Restitution (CoR), and the results shown above indicate that the CoR of the Cabosil is higher than that of the latex, as higher CoR's yield more bouncing. Comparison of Figures 72 and 78, and Figures 73 and 79 show that the flow patterns represented by both particles are generally the same, with the exception of the bouncing evident in Figures 72 and 73. Both representations indicate a strong skewing of the flow towards the partition, and the same general flow path through the pin array. Additional discussions regarding the comparison of the two particles, their sizes, and their effectiveness occur in Chapter 6.

# CHAPTER 6

# ERROR ANALYSIS

## 6.1 Introduction

The purpose of performing an error analysis on a quantitative flow visualization method can be divided into two categories. The first category concerns determining the accuracy with which the seed particles represent the true fluid flow. This is a function of both particle size and mass, and the methods for determining both are discussed below. The search for appropriate seed particles can sometimes be difficult, as the particles must reflect enough light to be measured by the image acquisition system (camera), while still being able to respond to quick changes in flow direction within a reasonable response time. Many times, as was the case with the Cabosil particles used for the pin array experiments (discussed in Section 5.6), the particles can be easily visualized, but questions lie in whether the particle trajectories visualized are accurate representations of the fluid flow. This question is addressed below in Sections 6.2-6.4. In Section 6.2, a drag-based response equation is used to determine the time necessary for entrained particles to respond to the changes in the flow direction. In Section 6.3, two methods of determining the size of seed particles added to the flow are discussed. Additional discussions based on the Coefficient of Restitution are found in Section 6.4.

The second concern regards the accuracy of the image analysis method (CIIQ programs, see Chapter 4) and its components. An initial accuracy can be determined by comparing the velocity results of the analyzed data (processed images) to those found by intrusive measurement devices. The velocity values determined by using the CIIQ programs are first compared to velocity values

derived from flow meters for the experiments performed in water and oils, and Pitot tubes for the experiments in the wind tunnel. These values determine if the results generated by the CIIQ programs are relatively close (well within an order of magnitude) to the experimentally measured values. Although the flow meter used in the water experiments determines a bulk flow rate, an average velocity can be determined for comparative purposes over specific cross-sectional areas. Additionally, the use of Pitot tubes at various locations can yield velocity values for easy comparison. While this type of comparison quickly shows that the CIIQ programs are accurate, it became necessary to quantify the accuracy of the system. An uncertainty evaluation and error analysis provides a better gauge of this accuracy, while a statistical analysis, based on the Standard Error Estimate (SEE), provides a percentage range that all values determined by the CIIQ programs fall within. These two error quantification methods are discussed below in Sections 6.5-6.6.

## 6.2 Particle Response Equation

The time it takes for a particle to respond to the sudden changes in the flow around it is desired. In the case of the FFFT/CIIQ Flow Visualization method discussed here, this time response must be faster than the time interval between contingous traces to guarantee accurate flow representation. To determine this time response, a study was performed based on the viscous drag force that acts on a particle in a turbulent fluid due to the relative motion between the particle and the surrounding fluid described by Drain [67]. If the particle is to follow a path that is truly representative of the flow, hte inertial forces of the particle must be negligible in comparison to these viscous drag forces. This viscous drag force acting on a spherical particle of a given radius is related to the relative velocity of the particle with respect to the fluid by Stoke's law:

$$\mathrm{F}_p = m_p \frac{\mathrm{d}v_p}{\mathrm{dt}} = 6\pi\eta\mathrm{r}(\mathrm{u}\text{-}v_p) \tag{5}$$

where r is the radius of seed particle, u is the velocity of the fluid, $v_p(t)$ is the velocity of the particle at discreet times, $\eta$ is the viscosity of the fluid, $m_p$ and $\rho_p$ are the mass and density of particle respectively. For a constant fluid velocity (u), the solution of Equation 5, and thus the equation of motion of the particle is:

$$v_p(t) = u + \{ v_p(0) - u \} e^{-\alpha} \tag{6A}$$

$$\text{where} \quad \alpha = \frac{t}{\tau_p} \quad \text{and} \quad \tau_p = \frac{m_p}{6\pi\eta r} = \frac{2\rho_p r^2}{9\eta} \tag{6B}$$

For the experiments performed, the worst case was assumed where the initial velocity of the particle was $v_p(0)=0$. Equation 6A was then rearranged so that the response time could be solved as a function of the particle velocity relative to the fluid velocity ($\beta=v_p/u$) and the time constant $\tau_p$:

$$t= -( \ln(1-\beta) )\tau_p \tag{7}$$

By varying the values of $\beta$ from 5 to 99 percent, response time curves can be generated for particles of various sizes, several of which are discussed below.

For both the water and oil tunnels, Magnesium Oxide ($MgO_2$) was used as the seed particles. The experiments were performed using a 10 $\mu$m filter to prohibit particles (or clumps of particles) larger than this size from entering the flow. The relative ratio the densities of the seed particles {$\rho(MgO_2)$=3,580 kg/m$^3$} and the working fluids {$\rho$(oil)=930 kg/m$^3$); $\rho$(water)=1000 kg/m$^3$} resulted in response times being almost instantaneous. For the combination of water and Magnesium Oxide particles (specific gravity=3.58), the time constant of Equation 6B was found to be Tp=22.015 microseconds for a 5 micron $MgO_2$ particle (the approximate mean). The solution of Equation 7 with this time constant was found to be 22 microseconds for a 90% particle response. Since the source video images were recorded at strobing frequencies of 120 and 240 Hz (8.333 and 4.167 milliseconds respectively), the particle time response was a full two orders of magnitude below the sampling rate ensuring that accurate flow

representations were recorded. This immediate time response is more effectively illustrated in a graphical format.

Figure 81 presents graphically results generated using Equation 7. The graph describes the time necessary for 1 and 10 $\mu$m size $MgO_2$ particles to reach the flow velocity if entrained from rest by constant velocity water flowing at a rate of 100 cm/sec. As the figure indicates, a 1 $\mu$m $MgO_2$ particle will reach the fluid velocity in approximately 2 $\mu$secs, while a 10 $\mu$m $MgO_2$ particle will reach this velocity in nearly 10 $\mu$secs. Both of these time responses are well below the the maximum allowable time response determined by the sampling rate (strobing frequency) of 4.167 milliseconds. As the density of the water and oil are within 10% of one another, it can be derived from Equations 6B and 7 that the time response of the particles will similarly vary within 10%. This simple calculation shows that the time response of the particles in the oil experiments are also well below (two orders of magnitude) the maximum driven by similar strobing frequencies, and insure that the strobed images of the flow recorded on video tape accurately represent the flow.

For the combination of air {$\rho$(20° C (68° F))=1.21 kg/m$^3$ (.0755 lbm/ft$^3$) with a dynamic viscosity: $\eta$=1.8&10$^{-5}$/sec-m (0.0179cP)}, and latex particles {specific gravity= 0.906, $\rho$(latex)=906 kg/m$^3$}, the time constant was found to vary between $\tau_p$=2.79 $\mu$secs for a 1 $\mu$m particle to 44.7 $\mu$secs for a 4 $\mu$m particle. Additionally, if a 1 $\mu$m particle starts at zero velocity {vp(t=0))=0}, it will reach 95% of the air velocity in 8.37 $\mu$secs while a 4 $\mu$m particle would need 134 $\mu$secs to reach the same velocity. For the Cabosil particles, the time constants ($\tau_p$) for the same sizes were found to be 5.55 and 88.89 $\mu$secs for 1 and 4 $\mu$m particles respectively, or about twice that of the latex particles. Also, the response time necessary for the particles to reach 95% of the air velocity increased to 16.64 and 226.29 $\mu$secs. These response times are both below the 333 $\mu$secs maximum allowable time response as determined by the strobing frequency this data was recorded with of 3000 Hz. Considering the issue of response times in non-constant, non-linearly accelerating flows, a graphical representation of a 1 $\mu$m particle's time response to an exponential decrease or increase in flow velocity is

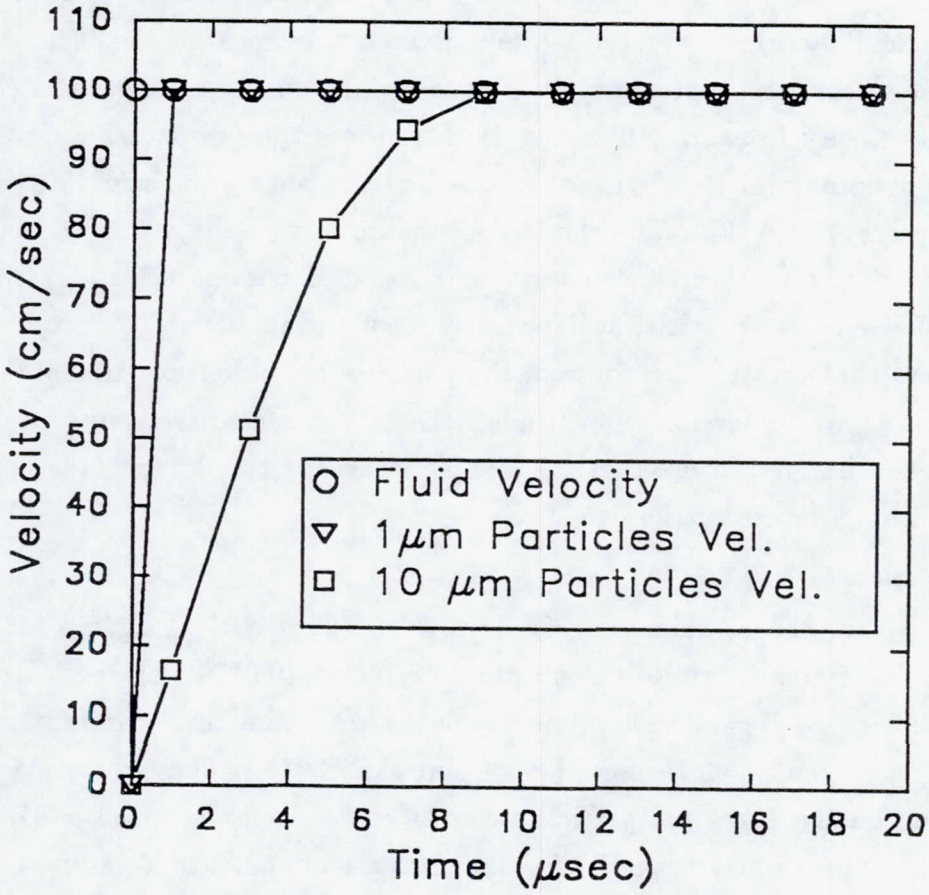



Figure 81: Time Response Curves for Seed Particles Entrained in Water

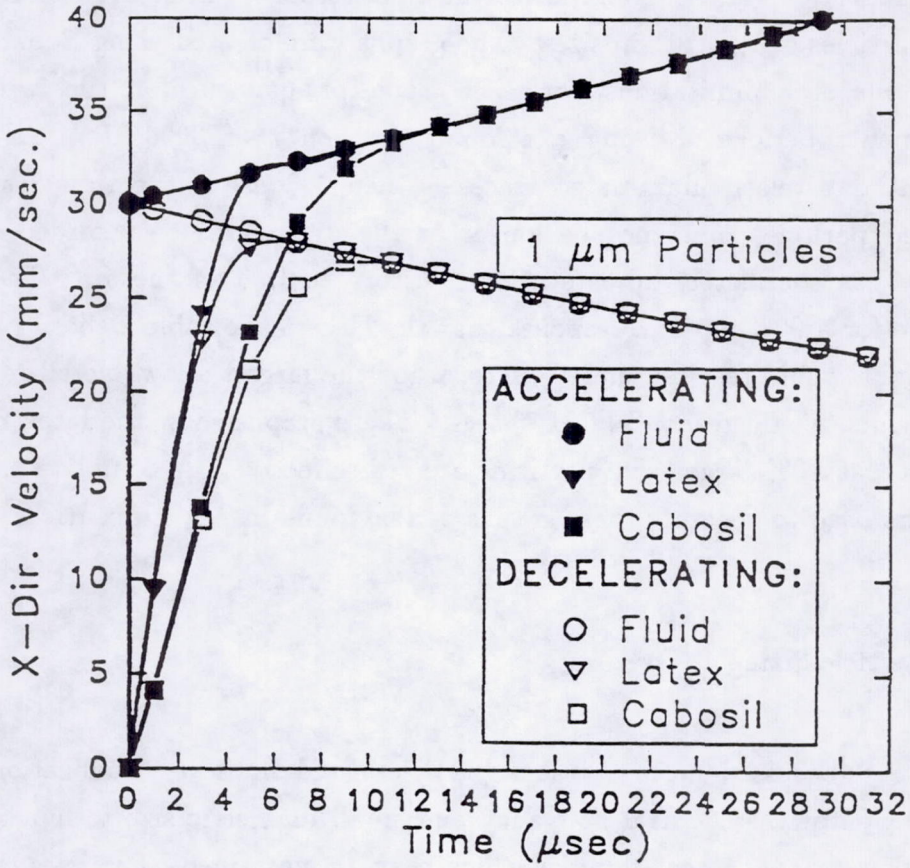



Figure 82: Time Response Curves for Particles Entrained in Air

shown in Figure 82. This figure illustrates that latex particles of the same size respond to the flow perturbations twice as fast as the Cabosil particles. This figure shows that the specific gravity (density) of a seed particle is equally important as the particle size in the determination of response times.

Figures 83 and 84 summarize the time responses in air flow of Cabosil and latex particles of 1 to 10 $\mu$m sizes. The graphs were created using Equation 7, and reveal the size limitations for each type of particle for the wind tunnel experiments performed using a strobing frequency of 3000 Hz. As the time differential between illuminated traces is then 333 $\mu$secs, the time responses for the seed particles must not be longer or the image will be recorded before the particle has completely adjusted its trajectory to that of the air. These graphs indicate for a 90% particle response that the largest allowable Cabosil particle is 5 $\mu$m, which would respond in 320 $\mu$secs, while the largest allowable latex particle is 7$\mu$m, which would respond in 315 $\mu$secs. These graphs show the latex to be more desirable as 40% larger size particles are still effective. A complete table of the numbers used to generate these graphs can be found in Appendix B.

## 6.3 Particle Sizing

As discussed earlier, tracer particles used in flow visualization methods must tend towards neutral bouyancy and small diametric size to quickly respond to sudden changes in the flow for which they are entrained. Particles that are too heavy or large cannot respond fast enough to these flow variations, and therefore follow a path that is nonrepresentative to that of the fluid flow. The time response discussion above explains the need for particles to be within a certain range if they are to be accurate seed particles. Here, the methods of determining the accurate sizes of the particles entrained in the fluids are discussed. For the experiments performed in the continuous loop water and oil tunnels, it was easy to determine that the particles were within the ranges that were required. In-line filters were installed that limited the sizes of the Magnesium Oxide ($MgO_2$) particles that traveled through the system to less than 10 $\mu$m, a size that was

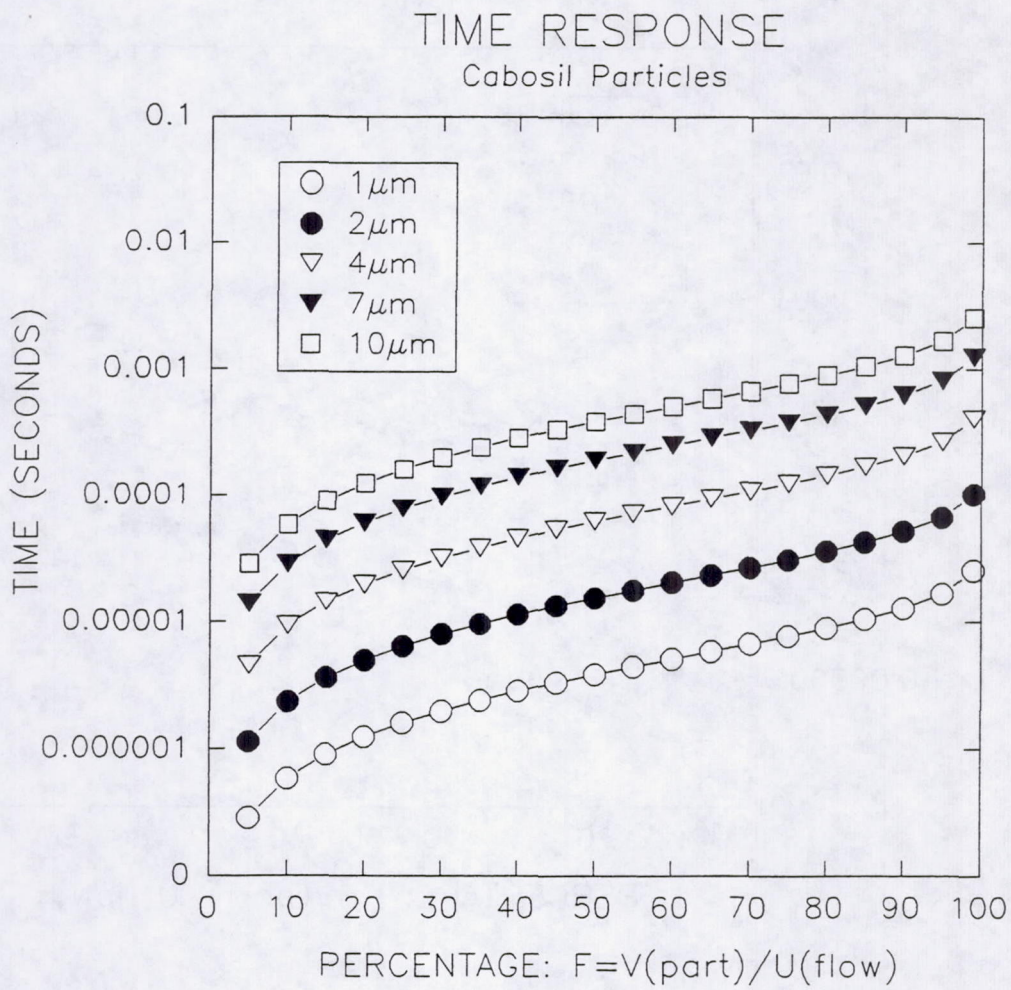



Figure 83: Time Response Curves for Cabosil Particles Entrained in Air

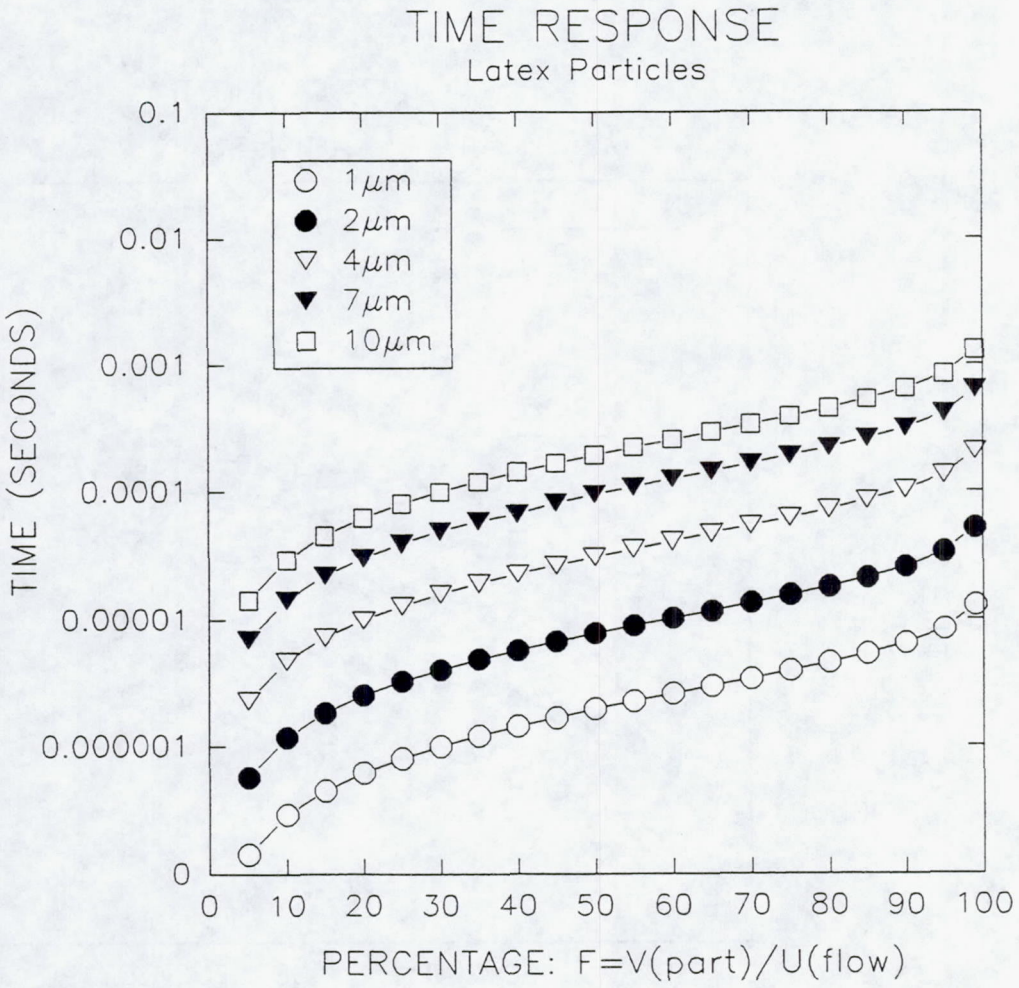



Figure 84: Time Response Curves for Latex Particles Entrained in Air

shown above (Section 6.2) to be acceptable. However, in the wind tunnel experiments, an in-line filter could not be used as it was an open loop system. The only place that a filter could be used was in the particle dispersion system (Section 3.6), and filters ranging in size from 1.0-2.5 $\mu$m were employed. Two probes were used to determine the actual particle sizes after dispersion.

The TSI Aerodynamic Particle Sizer (APS) [68] (Figure 85) measures the aerodynamic diameter, which is defined as the diameter of a unit density sphere with the same settling velocity. The machine functions as air containing particles is passed through an orifice into a chamber that contains a laser Doppler velocimetry (LDV) device. As particles of increased size possess a greater inertia, a lag in the particle velocity can be seen. As velocity is directly related to the particle's aerodynamic diameter, an entire particle spectrum can be determined. Diametric size spectrums of the Cabosil powder and the latex spheres were determined, and are shown in Figures 86 and 87 respectively. Measurements taken in the test section (Figure 7) with the TSI APS showed that the Cabosil particles spectrum (maximum recorded size reaching 15 $\mu$m) contained particles that were larger than that of the latex spheres (maximum recorded size of approximately 3.5 $\mu$m). While all of the latex particles measured by the APS were under the 7 $\mu$m maximum determined in Section 6.2, 3.8% of the Cabosil particles measured by the APS fell above the 5 $\mu$m maximum for 90% particle velocity time response. The larger diameters, coupled with the higher masses (1800 kg/m$^3$ compared to 1055 kg/m$^3$) contribute to the innability of some of the Cabosil particles' to follow the correct flow path.

As the APS device uses an inlet tube to ingest the particles for measurement, it was suggested by some experts in the field of particle tracking [66] that an alternative method of determining the sizes of the particles be employed to confirm these results. As the use of ethanol-floated latex particles appeared to be more successful, they were chosen to be examined using another probe. The sizes of the ethanol floated particles being dispersed by the air brush were measured a second time using an Aerometrics Phased Doppler Particle Analyzer (PDPA) [66,69] on two occasions. The PDPA performs its

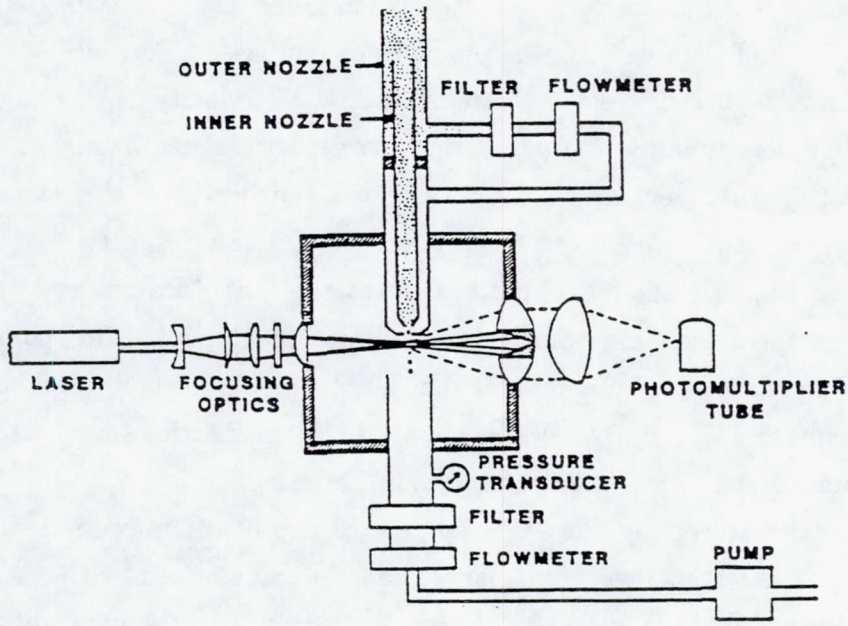



Figure 85: Schematic of TSI Aerodynamic Particle Sizing System

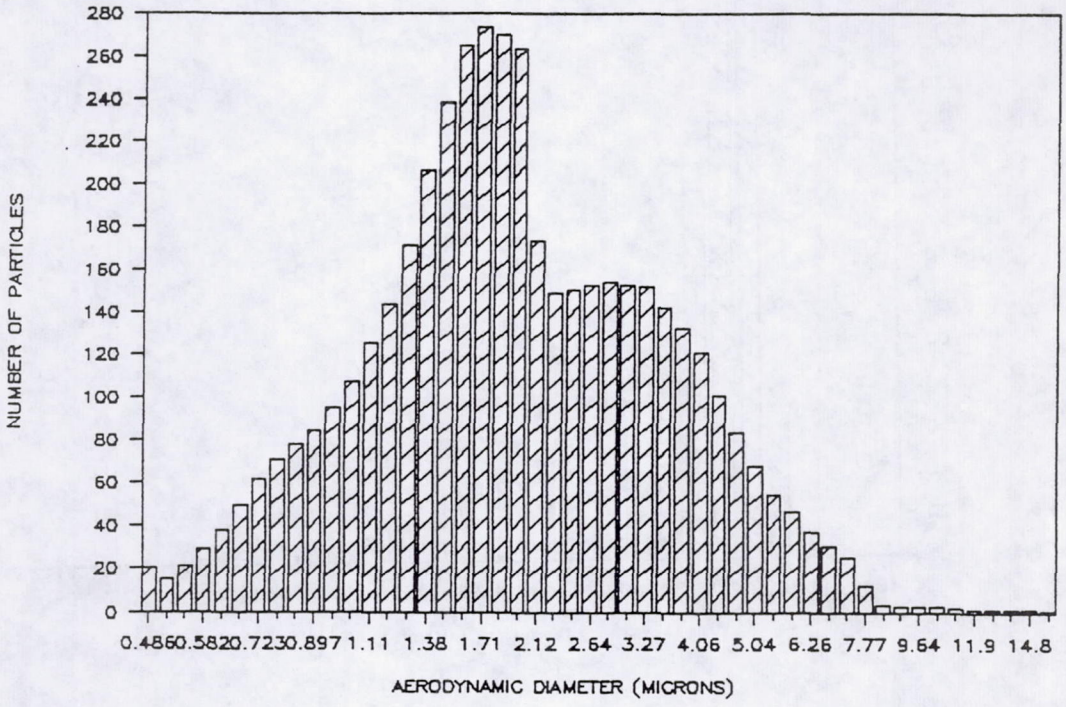



Figure 86: Diametric Size Spectrum (Distribution) for Cabosil Particles (APS)

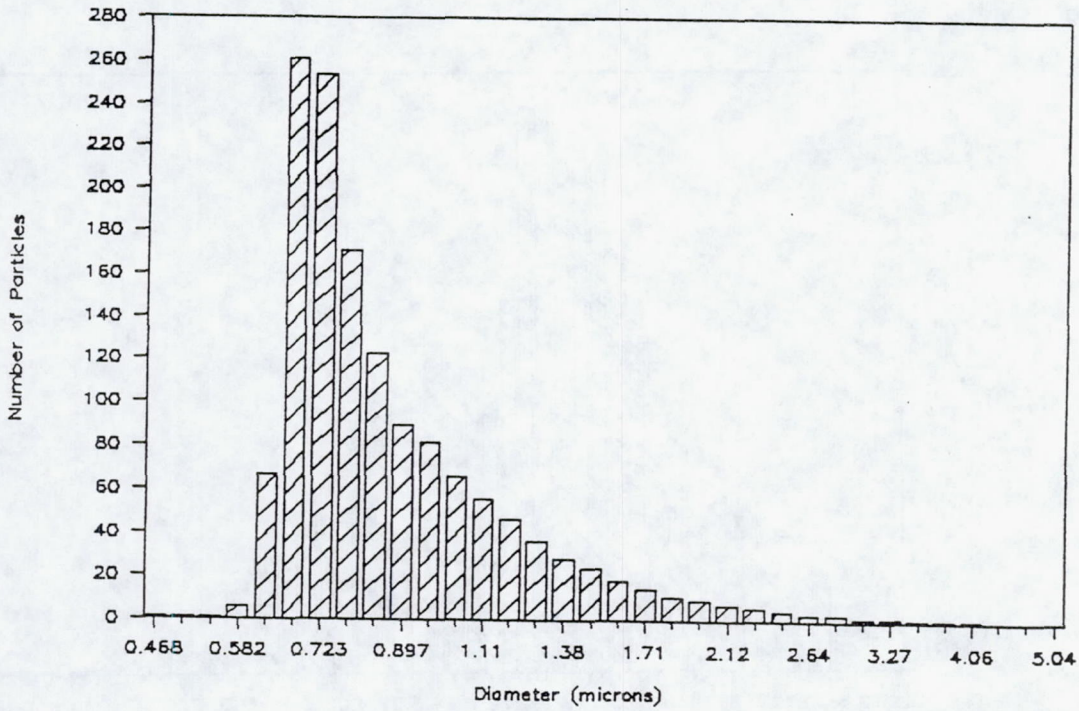



Figure 87: Diametric Size Spectrum (Distribution) for Latex Spheres (APS)

measurements by scanning a sample of particles that pass through the intersection of crossed laser beams. The PDPA is based on the LDV principle enabling the sizes of spherical droplets to be measured. As these particles pass through the intersection of two laser beams, they scatter light which produces a fringe pattern. This fringe pattern is then measured by three specifically spaced sensors that measure the frequencies of these patterns. The smaller diameter particles that possess greater curvatures will produce fringe patterns with lower frequencies, while the larger particles with smaller curvatures will produce higher frequencies. The calibration of the sensors with constant size particles will allow the sizes of any droplet to be measured very accurately. The PDPA could not be used to determine the particle sizes in the test section due to its size, so a particle spectrum was taken at the point of dispersion. Similarly, a direct comparative measurement at the point of disperion using the APS could not be performed as it does not accept liquid floated particles well due to its configuration, and it cannot measure sizes larger than 15 $\mu$m.

The droplets evaporate as the ethanol/latex mixture travels downstream, leaving only the latex particles to be mapped as they travel through the test section. To increase the evaporation rate, the ethanol/latex mixture was heated to 120° F. If all of the ethanol droplet envelope evaporates fully before reaching the test section, it would have no effect regarding the mapping of the flow field, as only the latex particles would be digitized. (The time responses determined in Section 6.2 for the latex particles ignored the presence of ethanol.) Using a computer code based on the evaporation rate of ethanol [66,70], the sizes of the ethanol/latex droplets in the test section were determined based on the air velocity and the initial particle size. This program revealed that for the particles to reach acceptable sizes in the test section, the latex/ethanol particles (droplets) must be smaller than 40 microns at the point of dispersion. Figure 88 illustrates these results in graphical form.

Two tests were performed, and it was found that the sizes of the ethanol and latex mixture particles were higher at the point of the dispersion than the sizes recorded by the APS in the test section, as Tables 6.1 and 6.2 indicate.

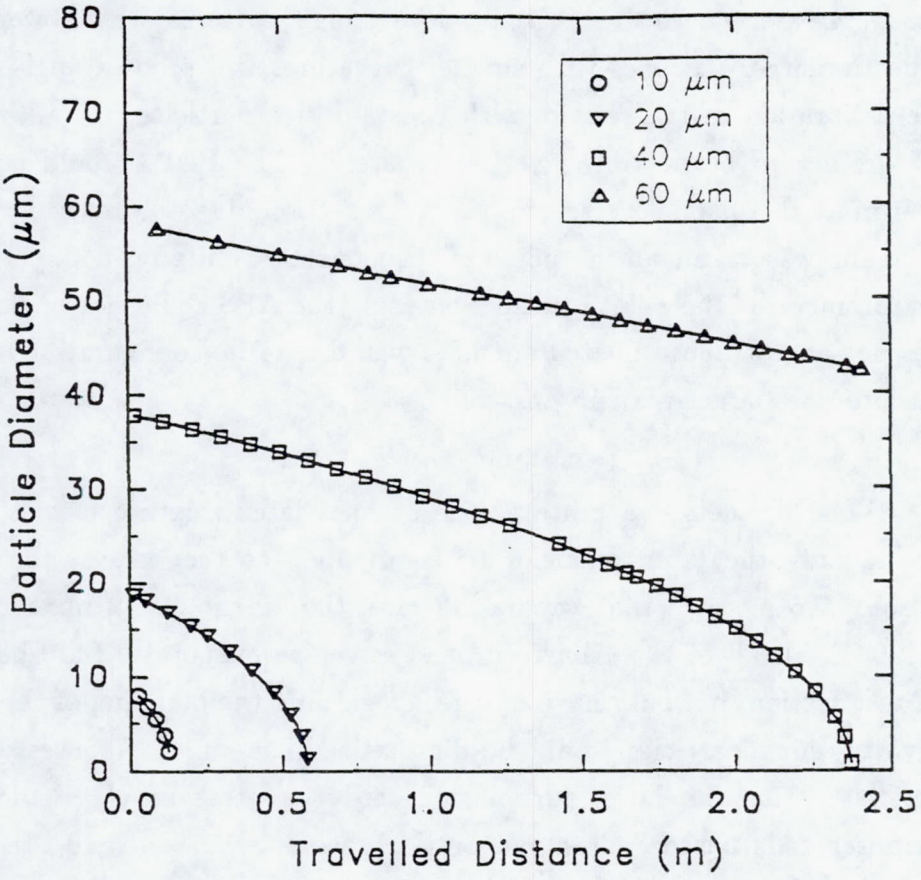



Figure 88: Ethanol-Latex Mixture Droplet Size vs. Distance Graph

| Bin | Diam. | Count | ΣCount | %Tot | Σ% |
|---|---|---|---|---|---|
| 0 | 2.86 | 6,892 | 6,892 | 31.2 | 31.2 |
| 1 | 4.84 | 4,468 | 11,360 | 20.2 | 51.5 |
| 2 | 6.82 | 2,912 | 14,272 | 13.2 | 64.6 |
| 3 | 8.80 | 1,991 | 16,263 | 9.02 | 73.7 |
| **4** | **10.79** | **1,452** | **17,715** | **6.58** | **80.2** |
| 5 | 12.77 | 986 | 18,701 | 4.47 | 84.7 |
| 6 | 14.75 | 758 | 19,459 | 3.43 | 88.1 |
| 7 | 16.73 | 502 | 19,961 | 2.27 | 89.1 |
| **8** | **18.72** | **371** | **20,332** | **1.68** | **92.1** |
| 9 | 20.70 | 292 | 20,624 | 1.32 | 93.4 |
| 10 | 22.68 | 208 | 20,832 | 0.94 | 94.4 |
| **11** | **24.66** | **194** | **21,026** | **0.88** | **95.2** |
| 12 | 26.65 | 118 | 21,144 | 0.53 | 95.8 |
| 13 | 28.63 | 106 | 21,250 | 0.48 | 96.3 |
| 14 | 30.61 | 84 | 21,334 | 0.38 | 96.6 |
| 15 | 32.59 | 79 | 21,413 | 0.36 | 97.0 |

| Bin | Diam. | Count | ΣCount | %Tot | Σ% |
|---|---|---|---|---|---|
| 16 | 34.58 | 54 | 21,467 | 0.24 | 97.2 |
| 17 | 36.56 | 54 | 21,521 | 0.24 | 97.5 |
| **18** | **38.54** | **45** | **21,566** | **0.20** | **97.7** |
| 19 | 40.52 | 25 | 21,591 | 0.11 | 97.8 |
| 20 | 42.51 | 21 | 21,612 | 0.10 | 97.9 |
| 21 | 44.49 | 22 | 21,634 | 0.10 | 98.0 |
| 22 | 46.47 | 22 | 21,656 | 0.10 | 98.1 |
| 23 | 48.45 | 20 | 21,676 | 0.09 | 98.2 |
| 24 | 50.44 | 13 | 21,689 | 0.06 | 98.2 |
| 25 | 52.42 | 14 | 21,703 | 0.06 | 98.3 |
| 26 | 54.40 | 8 | 21,711 | 0.04 | 98.3 |
| 27 | 56.38 | 8 | 21,719 | 0.04 | 98.4 |
| 28 | 58.37 | 14 | 21,733 | 0.06 | 98.4 |
| 29 | 60.35 | 9 | 21,742 | 0.04 | 98.5 |
| 30 | >61 | 335 | 22,077 | 1.50 | 100 |

Total Particles: 22,077

Table 6.1: Calculated Diametric Size Distribution for Heated Ethanol-Latex Mixture Droplets (Data Taken February 20, 1991)

| Bin | Diam. | Count | ΣCount | %Tot | Σ% |
|---|---|---|---|---|---|
| 0 | 3.14 | 1,015 | 1,015 | 60.9 | 60.9 |
| 1 | 5.32 | 264 | 1,279 | 15.8 | 76.8 |
| 2 | 7.50 | 152 | 1,431 | 9.12 | 85.9 |
| 3 | 9.68 | 66 | 1,497 | 3.96 | 89.9 |
| **4** | **11.86** | **37** | **1,534** | **2.22** | **92.1** |
| 5 | 14.04 | 9 | 1,543 | 0.54 | 92.6 |
| 6 | 16.22 | 21 | 1,564 | 1.26 | 93.9 |
| **7** | **18.40** | **7** | **1,571** | **0.42** | **94.3** |
| 8 | 20.58 | 4 | 1,575 | 0.24 | 94.5 |
| 9 | 22.76 | 3 | 1,578 | 0.18 | 94.7 |
| **10** | **24.94** | **3** | **1,581** | **0.18** | **94.9** |
| 11 | 27.12 | 2 | 1,583 | 0.12 | 95.0 |
| 12 | 29.30 | 4 | 1,587 | 0.24 | 95.3 |
| 13 | 31.48 | 0 | 1,587 | 0.00 | 95.3 |
| 14 | 33.66 | 1 | 1,588 | 0.06 | 95.3 |
| 15 | 35.84 | 0 | 1,588 | 0.00 | 95.3 |

| Bin | Diam. | Count | ΣCount | %Tot | Σ% |
|---|---|---|---|---|---|
| **16** | **38.02** | **2** | **1,590** | **0.12** | **95.4** |
| 17 | 40.20 | 1 | 1,591 | 0.06 | 95.5 |
| 18 | 42.38 | 3 | 1,594 | 0.18 | 95.7 |
| 19 | 44.56 | 1 | 1,595 | 0.06 | 95.7 |
| 20 | 46.74 | 3 | 1,598 | 0.18 | 95.9 |
| 21 | 48.92 | 5 | 1,603 | 0.30 | 96.2 |
| 22 | 51.10 | 1 | 1,604 | 0.06 | 96.3 |
| 23 | 53.28 | 5 | 1,609 | 0.30 | 96.6 |
| 24 | 55.46 | 3 | 1,612 | 0.18 | 96.8 |
| 25 | 57.64 | 4 | 1,616 | 0.24 | 97.0 |
| 26 | 59.82 | 4 | 1,620 | 0.24 | 97.2 |
| 27 | 62.00 | 0 | 1,620 | 0.00 | 97.2 |
| 28 | 64.18 | 0 | 1,620 | 0.00 | 97.2 |
| 29 | 66.36 | 1 | 1,621 | 0.06 | 97.3 |
| 30 | >67 | 45 | 1,666 | 2.70 | 100 |

Total Particles: 1,666

Table 6.2: Calculated Diametric Size Distribution for Heated Ethanol-Latex Mixture Droplets (Data Taken March 1, 1991)

Table 6.1 describes the sample measured on Feb. 20, 1991 possessing 89.9% of its particles less than 11.0 $\mu$m, 94.3% less than 19.0 $\mu$m, 94.9% less than 24.9 $\mu$m, and 95.4% less than 39.0 $\mu$m. For the sample measured on March 1, 1991 (Table 6.2), 80.2% were less than 11.0 $\mu$m, 92.1% were less than 19.0 $\mu$m, 95.0% were less than 24.9 $\mu$m, and 97.7% were less than 39.0 $\mu$m. Putting these numbers into perspective, the experimental sample taken in February measured over 21,000 particles in three seconds total time (90 frames of video tape), and found only 511 (or 2.3%) not within the required size range. This means that only 5 or 6 particles of incorrect size would appear on each frame compared to 230 particles that do meet the size requirements. For the sample taken in March, only 46 particles (4.6%) out of the 1,666 taken over a time of 10.5 seconds were larger than desired. This corresponds to an average of one oversized particle appearing every seventh frame over the 300 frames sequence. Both of the above calculations assumed that each particle stayed in the field of view for only one frame, which was usually the case.

The variance in the two samples discussed above was attributed to experimental error, such as misalignment of the beams, the sensors, the directional trajectory of the particle spray, and the amount of particles being released into the probe. Even accounting for the variance, it was shown that at least 95.4% of the particles measured at the point of dispersion measured less than 39 $\mu$m. The importance of this measurement is that according to calculations performed using a computer code [70,71], a distance of approximately 2.5 meters (8.125 feet) is needed for the 40 $\mu$m size droplets to evaporate to the acceptable sizes (see Section 6.2) of less than 7 $\mu$m in the test section. As the dispersion of the particles during the experiments took place at approximately this distance, it shows that the majority of the ethanol 'carrier fluid' had indeed evaporated, leaving a latex particle of proper size in the test section area to follow the flow. With the combined weighted average of the two sets of data showing only 2.3% of the two samples larger than 40 $\mu$m, it is safe to say that the TSI analyzer results were fairly accurate, and that for the most part, the smaller acceptable size latex particles were indeed all that remained when reaching the test section.

This remaining 2.3% that was measured by the PDPA, but not in the test section by the TSI APS, were considered particles too large to be measured by the TSI APS. According to the data taken by the PDPA and entered into the evaporation code, some particles should have been larger than 15 microns when reaching the test section. The PDPA is considered a more accurate measure of size due to the fact that larger wet particles may not be able to pass through the entrance tube of the APS to the enclosed LDV device. Still, according to the PDPA measurements and the evaporation code calculations discussed, the vast majority of the latex particles were within the required range.

The PDPA has been used to demonstrate that the TSI APS data was reasonably accurate, and the analysis in Sections 6.2-6.3 have also shown both the Cabosil and the latex to be viable seed particles. Both the size and density were shown to affect the time response of seed particles entering into flow paths. Additionally, the existence of latex and Cabosil particles too large to accurately follow flow paths was shown to exist, however, only the Cabosil particles in Section 5.5 were shown following obviously non-representative flow paths (impacting the pins.) These results indicate the existence of another factor besides the density and diametric size affecting time response.

## 6.4 Coefficient of Restitution

The other factor besides particle size and density discovered when performing the wind tunnel experiments was the Coefficient of Restitution (CoR). This characteristic determines whether a particle heading directly for a leading edge rebounds away from it, or disintegrates on impact. As previously mentioned in Section 5.6, the Coefficient of Restitution is an important factor contributing to the characteristic bouncing of the Cabosil particles. The denser Cabosil particles are more rigid than the hollow latex spheres, so they rebound and re-enter the flow after impact with the pins. Although the images derived from the experiments using the latex give the impression that no particles impact, some of the particles in streamlines that end at a stagnation point do impact the pins.

Rather than rebounding into the freestream as the Cabosil particles have been shown to do, the latex particles shatter or disintegrate on impact in a large loss of energy. This is a direct result of the the hollow nature and elastic material properties of the latex spheres. This is not meant to imply that the latex particles do not follow the flow, but that some particles entrained in a fast moving flow that is in-line with a stagnation point will impact the leading edge. In the case of the latex, a lesser number of these particles impact due to their lower density and smaller sizes. Finally, as the differences between the Cabosil and latex particles have been shown to be similar and discussed in detail, it can be concluded that the flow visualization performed with the Cabosil particles is acceptable, although not as accurate as the results using the latex.

## 6.5 Operator Introduced Uncertainty Analysis

The chance exists that the digitization process of determining particle location could contain errors. Based on the uncertainty analysis described in the classical paper by Kline and McClintock [72], a general error can be discussed regarding the process of particle tracking. During the digitization process, the worst operator error was measured to be 2 pixels (in any direction) per digitized point, regardless of the length between two consecutive such points. For a portion of a trajectory that is 100 pixels long, the maximum error will be 4%, as this length could be digitized as long as 104 pixels, and as short as 96 pixels. Since this worst possible digitization error remains fairly constant at less than two (<2) pixels, it becomes evident that the shorter the trajectory length, the larger the potential error. Shorter distances between points on a trajectory occur when the tracked images were recorded using high strobing frequencies, or when slower flows are being studied. For the experiments discussed in this thesis that used monitors with pixel spacings of 756 x 581, and having a spatial resolution of 0.0187 in. (0.476 mm), a minimum length of 50 pixels between digitized points was observed. This practice kept this operator induced error below 8%, if the digitized length was off 2 pixels at each point in opposite directions. The user must be cautious that the interval between two consecutive positions ensures a

reasonable distance, to keep the digitization error within these limits. These results were found by repeating the same operation numerous times, and determining the variance, as was the case in Chapter 4 when the magnification factors were determined.

## 6.6 Statistical Analysis

As was discussed earlier, the fitting of the experimental data points trajectories was accomplished well with third order polynomials. The precision of these polynomial curve fits was estimated by means of the standard error estimate (SEE) [73]

$$\text{SEE}=\left\{ \sum_{i=1}^{N} [\ Y_i-(aX_i^2 + bX_i + c)^2\ ] \ / \ [\ \text{N-3}]\right\} \tag{8}$$

where N is the number of data points in a trajectory, and $X_i$ and $Y_i$ are the points for the two data sets. $Y_i$ indicates the actual digitized point, while the equation in the parenthesis $(aX_i^2 + bX_i + c)$ indicates the fitted point determined by the curve fitting subroutine in VADT (see Chapter 4). The '3' in the equation arises from the fact that three degrees of freedom are lost from the set of N data pairs when the constants a-c are determined. Figure 89 shows that the SEE for the trajectories fitting procedure varied between $\pm 4.92$ for the water experiments. The same figure presents the propagation of the SEE from the position fitting polynomials obtained by means of Equations 1 and 2 to the velocity predicting polynomials obtained by means of Equations 3 and 4. It can be seen that no new error was introduced in the estimation of the velocities, and that a range has been found that all of the values fall within. It was found that the SEE for the trajectories used in the wind tunnel/staggered pin array experiments varied between $\pm 5.46$, as can be seen in Figure 90. The same figure shows the propagation of error from the trajectory fitting polynomials, Equations 1 and 2, to the velocity fitting polynomials obtained by Equations 3 and 4.

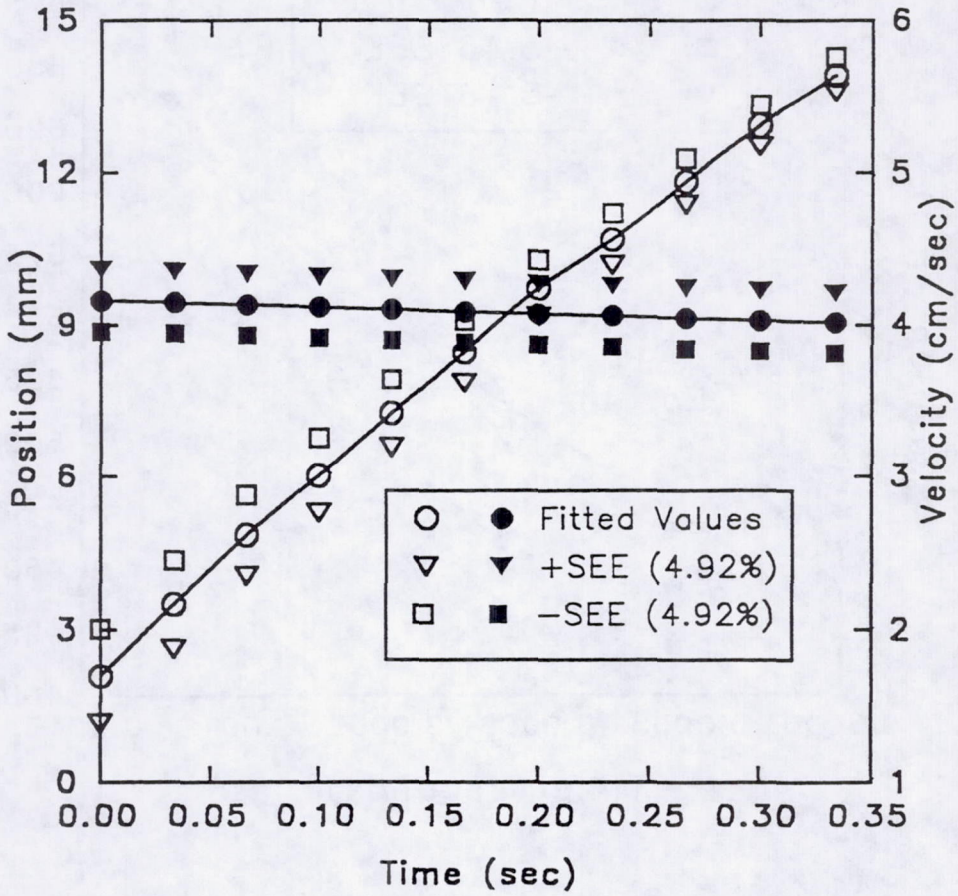



Figure 89: Standard Error Estimate (SEE) Curves for a Typical Trajectory Polynomial Fit and Respective Velocities (in Water)

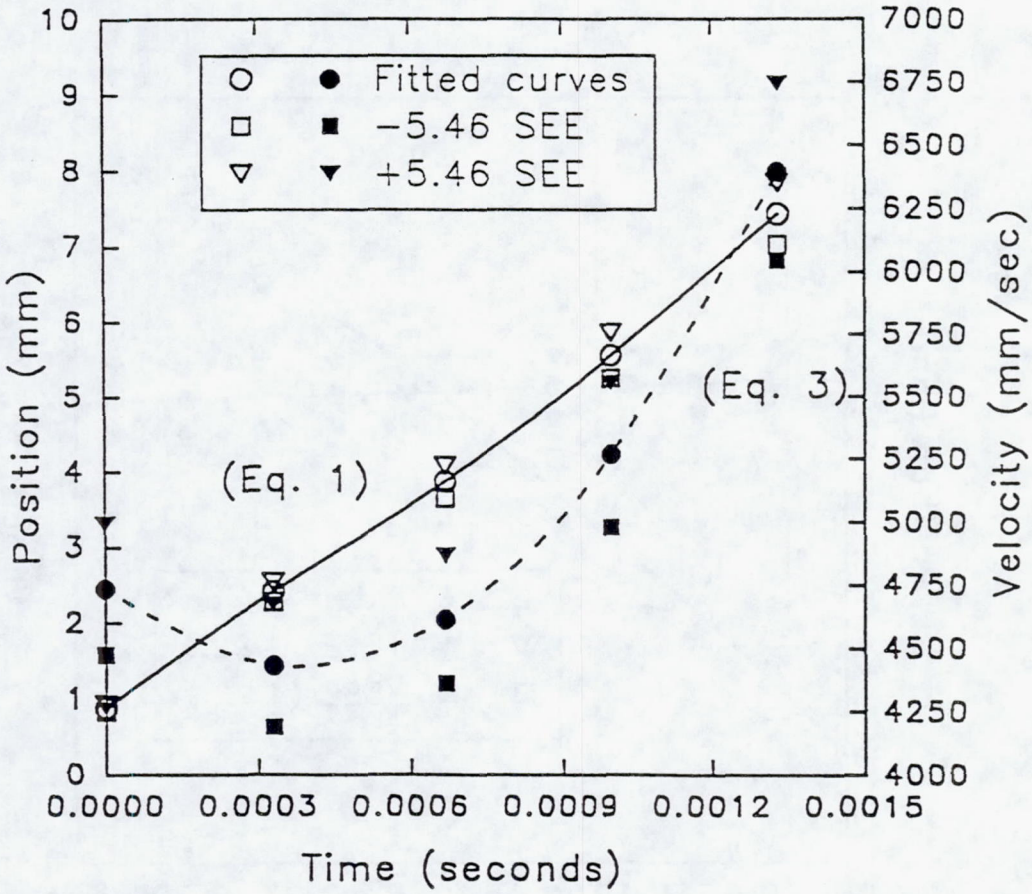



Figure 90: Standard Error Estimate (SEE) Curves for a Typical Trajectory Polynomial Fit and Respective Velocities (in Air)

Again, the error associated with the position of the trajectories did not propagate into the calculation of the velocities. It should also be noted that many of the fitted coordinates had errors in the range of 0-3% as shown in Figure 26, and that the SEE values indicated here are for worst case situations.

## 6.7 Total Error in the System

The propagation of individual sources of error throughout the system can be determined. These errors have been divided into three main sources which are the particle's response time, the accuracy of the image digitizing, and the accuracy of the curve fitting done by the computer algorithm. The seed particle's ability to follow the flow was shown to be a function of its size and density, and this issue was addressed in Sections 6.2 and 6.3. These results show that the majority of the seed particles used throughout the previously described research efforts reached at least 90% of the fluid flow within the required response time. The accuracy of the digitizing procedure was analyzed in Section 6.5 and was found to be a function of the distance between two digitized points. The accuracy of the curve fitting was addressed in Section 6.6 and was determined for both the cowl lip 180° cooling passages and the staggered pin array experiments. The determination of the total error, and thus the accuracy of the system, is performed for the experiments in these two geometries.

### 6.7.1 Total Error for the Cowl Lip 180° Cooling Passage Experiments

The time responses for the $MgO_2$ particles used in the cowl lip experiments were found to be two orders of magnitude less than necessary, as discussed in Section 6.2. It was shown that a 5 $\mu$m particle responded to 90% of the change in fluid velocity in 22 $\mu$secs. Note that in this case, the time interval determined by the strobing frequency was 4.2 milliseconds. It was concluded from these very fast response times that all of the $MgO_2$ particles properly followed the flow path in the cowl lip experiments.

The error due to digitizing the stored images was shown in Section 6.5 to be 4-8%. These numbers derive from the fact that the operator could incorrectly digitize two points over a distance of 50-100 pixels by two pixels in opposite directions. Additionally the curve fitting error, which was determined by comparing the actual points to those generated by the curve fitting algorithm using the Standard Error Estimate (SEE), was found to be 4.92% for the cowl lip experiments. The SEE establishes a window in which all the fitted points fall within relative to a digitized trajectory. Taking to account all of the errors discussed above, it was determined that the accuracy of the system for the cowl lip experiments was 87.5%. This figure was determined by multiplying the accuracy of each using the highest percentage errors for the SEE and the digitizing mentioned above.

Although the accuracy determined above is very acceptable considering the advantages of the FFFT/CIIQ system, it assumes the worst cases for both the SEE and the digitizing error. As the worst case is not the most common, the accuracy of the system is usually higher. If the reasonable assumption is made that the digitized points are off by only one pixel in any direction over a distance of 50 pixels, the digitizing error reduces to 4%. Additionally, many of the curve fits are extremely accurate, as shown in Figure 26, with the difference between the digitized and fitted points being approximately 1%. Considering this fact, even if the SEE determined above of 4.92% was lowed in half to 2.46%, it would still be a conservative figure for the majority of the points. If these lower error values are used, the accuracy of the system becomes 93.6%.

### 6.7.2 Total Error for the Staggered Pin Array Experiments

For the wind tunnel experiments, the PDPA and the TSI APS (see Section 6.3) were used to determine the sizes of both the latex and Cabosil particles. The sizes of the latex particles in the test section were determined using the PDPA and the code based on the evaporation rate of ethanol. The conclusion described in Sections 6.2 and 6.3 was that 2.3% of the latex particles were larger than

desired in the test section, meaning they were unable to accurately respond to the changes in the flow path. Using the APS, the percentage of unacceptable Cabosil particles was determined to be 3.8%. The particles in these percentages do not respond quickly enough to the changes in the fluid flow, and therefore follow a non-representative trajectory. These larger particles were not considered in the digitization process, as they appear nonhomogeneous on the video tapes in comparison to the majority of the seed particles due to their significantly larger size and brighter intensity. The total system error calculation only considers those particles deemed acceptable during the digitization process, and ignores these obviously oversized particles.

The values for the digitizing error (4-8%) do not change, while the SEE was recalculated to be 5.46% for the staggered pin experiments. Using the worst case values, the accuracy of the system was found to be 87.1% using the latex or Cabosil particles. Again more common values can be used in the calculations for the digitizing error (4%) and the fitting error (2.73%). Using these numbers in the calculations, the accuracy of the system for the wind tunnel experiments using latex spheres or Cabosil particles increases to 93.4%.

# CHAPTER 7

# RECOMMENDATIONS FOR FUTURE EXPERIMENTAL WORK

The work presented in this thesis describes the methodology of the FFFT/CIIQ flow visualization and quantification system, and the experimental results derived from its application. Although the technique described has been shown to be a viable method, some of its aspects could be improved to increase the system's capabilities. The recommendations presented here are a direct result of the experiences gained by performing the experiments previously discussed, and analyzing the images with the software package. Recommendations are also presented regarding future experimental work that should be performed.

## 7.1 Recommendations for Future Experimental Work

It is recommended that studies involving flow through staggered pins in a branched duct be extended to study higher velocities, and different geometries. Pin arrays could be varied by both the number of pins, the diameter of the pins, the spacing between the pins, and the alignment of the pin rows. The results found by comparing the different geometries could be used to improve the designs of internal cooling passages in turbine blades. Also, it is recommended that a geometry that more exactly represents a blade cooling passage be studied.

Further studies in cowl lip cooling passages could be performed with the addition of bristles in the curved portion, as indicated by Figure 91. Some preliminary work has shown that the addition of bristles increases the fluid turbulence and heat transfer in that area. Also, it is recommended that studies

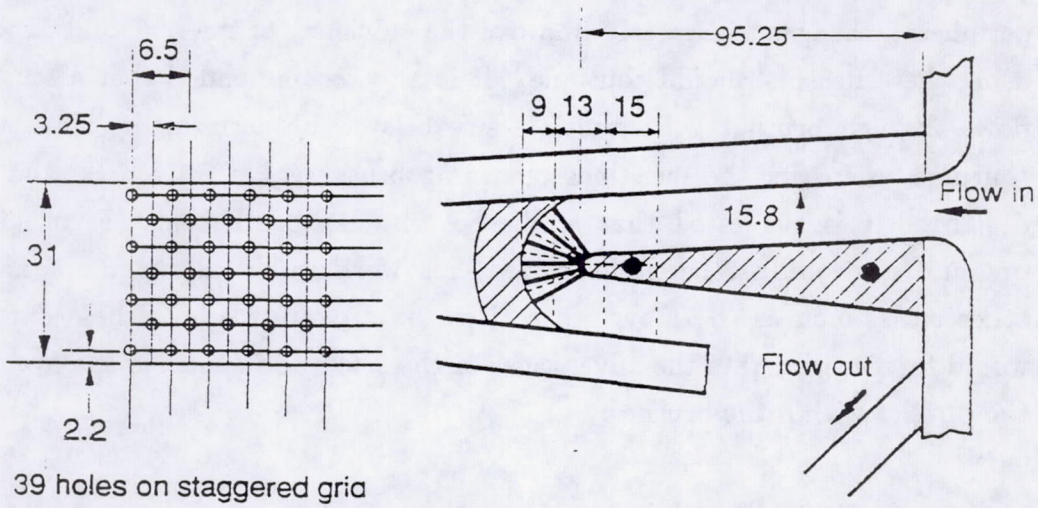



Figure 91: Schematic of Cowl Lip Cooling Passage with Brush Insert

in these cooling channels be extended to experiments in air, as that may be the coolant eventually used. Finally, experiments using thermocromatic liquid crystals are recommended to quantify the temperature changes thus determining the effectiveness of the various cooling passages. These could be performed by coating the surface of the channels with the crystals, and by floating them in the fluid.

Additional studies are recommended using linear brush seals with canopy tops and bottoms as shown in Figure 92. These brushes significantly reduce peripheral leakages and greatly improve the efficiency of the seal, and experiments using these brushes should continue. It is also recommended that a study of the flows through brushes with multiple size bristles be performed. This work will continue to answer the questions regarding brush seal effectiveness, and optimal designs. It is suggested that studies of circular brush seals (Figure 93) in a pressure environment be performed. This work would allow comparisons with other seals, such as the labyrinth seal, to be directly made. These experiments would further illustrate the advantages of the seals, and continue the evaluation of the physics within the brushes.

## 7.2 Recommendations for Improvements to the CIIQ System

This section describes recommended changes to the FFFT/CIIQ system that would increase its effectiveness as a flow visualization and quantification tool. These suggestions are divided into software modifications, and equipment upgrades. Advances could be made to automate various functions of the CIIQ process to decrease the time needed for image analysis, such as automatic image digitization. Although this automation would only be applicable in certain flow situations, it is still an improvement worth consideration. For the occasions in which point by point digitization would still be necessary, improvements to the digitization process could be made. The first advancement would be to modify the digitizing cross-hairs that appear on the grabbed image during the tracking of trajectories. The accuracy of this tracking would be improved by replacing the cross-hairs with a cursor that will determine the center of gravity of the pixels

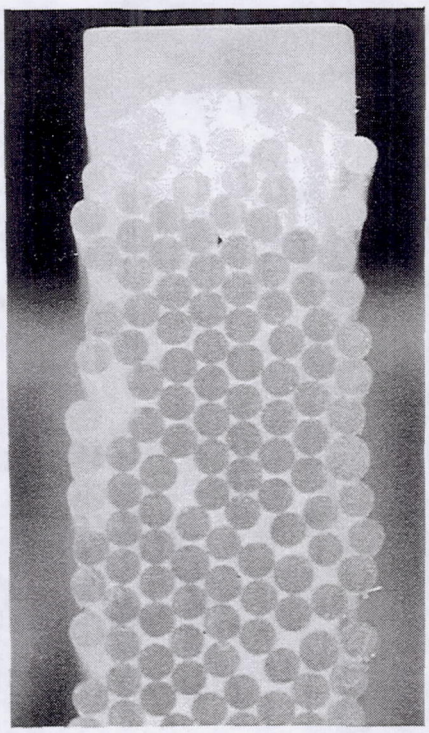


Figure 92: Photograph of a Linear Lucite Brush Seal with a Canopy Top

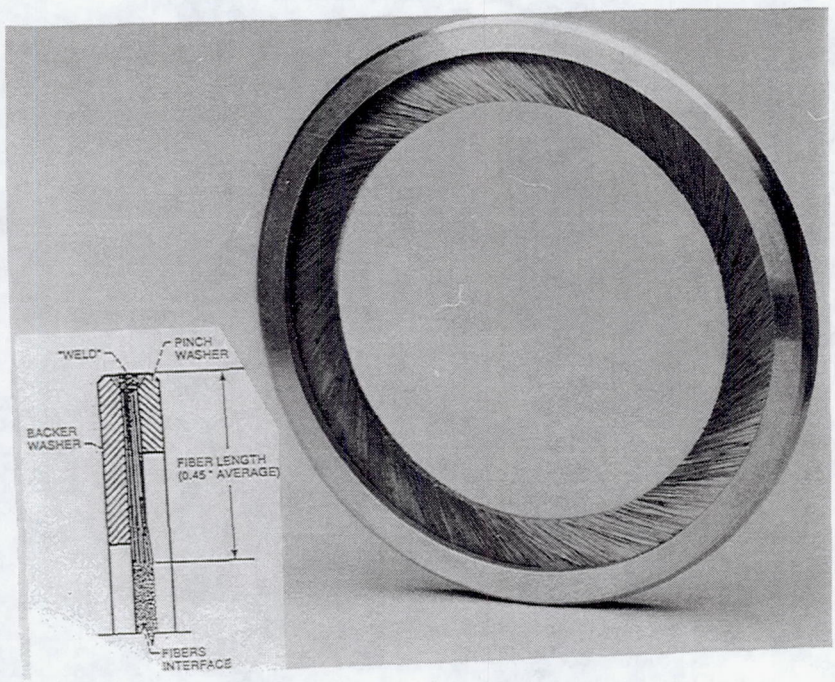



Figure 93: Photograph of Circular Brush Seal

illuminated due to the presence of a particle trace. The program would then mark the pixel nearest the center of gravity as the digitized point, eliminating the errors spoke of in Section 6.5.

Other suggested modifications to various sections of the programs would make them more user-friendly. These include the addition of on-line help screens, and the ability to transfer information between programs (such as the scale factors from FACT to SNAP). Additionally, some functions within the code are not reversible, meaning mistakes made when entering the data cannot be corrected. Improvements could also be easily made in the image assembly process that uses the Drafix CAD package. Currently, the files produced by VADT must be renamed and rescaled before being accepted into Drafix. Small changes to the codes would eliminate the need to modify these import files at all.

In addition to changes in the programs that make up the CIIQ package, equipment upgrades which would allow faster flows of nearly Mach 1 to be studied are recommended. To successfully image high speed flows, the particle size must be decreased while the strobing frequency must be increased. An investigation to determine the seed particles for these higher speed applications is recommended. It is suspected that seed particles of 1 $\mu$m or less must be used to study these higher velocity flows due to the very high response times required for accurate flow representation. Additionally, an acousto-optic modulator that is capable of generating strobing frequencies of up to 100 kHz would have to be added to the system. As discussed earlier (Section 3.5), smaller particles do not reflect as much light as larger ones, so an image intensifier mounted to the optical train would need to be added to the system to improve the ability to see the dimmer light reflecting particles. These upgrades should allow the system to examine flows at speeds approaching Mach 1.

Finally, it is recommended that a three-dimensional (3-D) method be developed. It is suggested that this method use multiple synchronized cameras, and orthogonally intersecting laser sheets to determine the three components of velocity. This method would be a natural extension of the FFFT/CIIQ method

that has been described. The recommended manner to process 3-D flows includes the use of two lasers to generate intersecting light sheets, creating a laser volume. Also, it is suggested that three cameras be used to observe the flow in the laser volume from three vantage points. The recommended positions of the cameras are to place two of them normal to the laser sheets, and a third either oblique to the volume, or parallel with a laser sheet. These cameras would generate three synchronous images of the flow from three perspectives, allowing the three components of velocity, and thus the resultant velocity to be determined.

# CHAPTER 8

# SUMMARY AND CONCLUSIONS

## 8.1 The FFFT/CIIQ Method

The experimental approach presented here offers a nonintrusive, qualitative and quantitative method of flow evaluation applicable to various geometries using a variety of fluids. This Full Flow Field Tracking (FFFT) technique makes obtainable the flow patterns themselves, and allows the determination of the velocities, accelerations, and mass flows of an entire flow field. The method utilizes a Computer Integrated Image Quantification (CIIQ) system that can study areas of interest at magnification factors of up to 100. These enlarged regions can be assembled to form an overall representation of a flow path both qualitatively and quantitatively. This system was shown to have substantial advantages over commonly used systems such as Laser Doppler Velocimetry, and Hot Wire/Film Anemometry.

Specific descriptions of the experimental facilities and hardware were discussed, and the operation of the computer-based image quantification system was thoroughly detailed. An extensive error analysis of the system was performed, and the overall accuracy of the system was shown to vary from 87.1% to 93.6%. The method was applied to three specific programs, and the results of these experiments were discussed, and are summarized below. Finally, recommendations were made as to how to improve the system, and what experiments to purform next using the method.

## 8.2 Applications

Specific applications of the system were presented in which the flow patterns and velocities were observed and evaluated in three distinct geometries, with three different working fluids. The first study involved the pressure and flow analysis of a brush seal in oil. The pressure profiles of various brush seal configurations were presented, and the characteristic flows that exist within a brush seal were determined. The benefits of using brush seals in series was demonstrated as pressure drops were increased, and flow rates were reduced. Additionally, the movement of bristles within the brush matrix due to changes in pressure and flow rate was documented. Examples of the self sealing characteristics the brushes possess, as well as a summary of the flows present within a brush seal were presented.

The next application involved studying the velocity and flow patterns in a cowl lip cooling passage of an air breathing aircraft engine using water as the working fluid. Three geometries were presented and compared, and a recommendation was made based on the flow patterns as to which would perform most efficiently. Also, images were assembled to yield the total flow patterns around the various geometries. Finally, the method was extended to a study in air to examine the flows in a staggered pin arrangement located on one side of a branched duct.

# REFERENCES


[1] Dally, J.W., Riley, W.F., McConnell, K.G., "Instrumentation for Engineering Measurements", Chapter 9 "Fluid Flow Measurements", John Wiley & Sons, 1984

[2] TSI Incorporated, "Hot Film & Hot Wire Anemometry: Theory & Application", TSI Technical Bulletin TB5, 1968

[3] Nelson, E., "Hot Wire and Hot Film Anemometry", Sensors (magazine), Sept. 1984, pp. 17-21

[4] TSI Incorporated, "Laser Velocimeter Techniques", TSI Technical Bulletin 25a, Appendix I, Laser Velocimetry System Catalog, 1979

[5] Rae, Jr., W.H., Pope, A., "Low-Speed Wind Tunnel Testing", 2nd Edition, John Wiley & Sons, 1984

[6] Veret, C., "Flow Visualization by Light Sheet", Third International Symposium on Flow Visualization (Flow Viz. III), Ann Arbor, Michigan, Sept. 1983, pp. 83-87

[7] Gennero, C., Mathe, J.M., "Real Time Edge Extraction Application to the Study of Vortices Cores", Flow Viz. III, Ann Arbor, Michigan, Sept. 1983, pp. 418-423

[8] Hiller, W.J., Kowalewski, T.A., "Application of the Frame-Transfer Charge-Coupled Device for High Speed Imaging", SPIE Vol. 1032-High Speed Photography & Photonics, Bejing, China, Oct. 1988, pp. 763-765

[9] Garcia, J.C.A., Hesselink, L., "3-D Reconstruction of Fluid Flow Visualization Images", Fourth International Symposium on Flow Visualization (Flow Viz. IV), Paris, France, Aug. 1986, pp. 235-240

[10] Safi, M.J., "Visualization of the Recirculation Flow in Enclosures", Flow Viz. IV, Paris, France, Aug. 1986, pp. 679-683

[11] Jezek, J., Resnicek, R., "Visualization of a Backward-Facing Step", Flow Viz. IV, Paris, France, Aug. 1986, pp. 365-370

[12] Ohnari, H., Saga, T., Watanabe K., Saitou, T., "Combined Simultaneous Flow Visualization/LDV Measurement in the Near Wall Region of Turbulent Channel Flow", Flow Viz. IV, Paris, France, Aug. 1986, pp. 395-400

[13] Porcar, R., Prenel J., Diemunsch, G., Hamelin, P., "Visualization by Means of Coherent Light Sheets", Flow Viz. III, Ann Arbor, Michigan, Sept. 1983, pp. 163-167

[14] Falco, R.E., "Visualization of Inner/Outer Layer Interaction Producing Turbulence Near Walls", Flow Viz. IV, Paris, France, Aug. 1986, pp. 327-332

[15] Werle, H., "Hydrodynamic Visualization of the Flow Phenomena Charecterizing Air Intakes", Flow Viz. IV., Paris, France, Aug. 1986, pp. 76-82

[16] Hentschel, W., Stoffregen, B., "Flow Visualization With Laser Light Sheet Techniques in Automotive Research", Flow Viz. IV, Paris, France, Aug. 1986, pp. 839-846

[17] Adrian, R., "Multipoint Optical Measurements of Simultaneous Vectors in Unsteady Flow- A Review", Int'l Journal of Heat and Fluid Flow-Vol. 7 No. 2, 1986, pp. 127-145

[18] Vysogorets, M.V., Platonov, V.N., Chulkin, A.D., "Personal Computer Oriented Software for the Pulsed Image Readout System", SPIE Vol. 1032-High Speed Photography & Photonics, Bejing, China, Oct. 1988, pp. 782-785

[19] Goss, L.P., Post, M.E., Trump, D.D., Sarka, B., MacArthur, C.D., Dunning, G.E., "A Novel Technique for Blade to Blade Velocity Measurements in a Turbine Cascade", AIAA/ASME/SAE/ASEE 25th Joint Propulsion Conference, Monterey, California, July 1989, AIAA-89-2691

[20] Gharib, M., Willert, C., "Particle Tracing: Revisited", AIAA/ASME/SIAM/APS 1st National Fluid Dynamics Congress , Vol. 3, Cincinnati, Ohio, July 1988, pp. 1935-1943

[21] Walter, J.A., Chen, C.J., "Flow Visualization of Particle Streaks in Offset Channel Flow by a Direct CCD Imaging Process", ASME Winter Annual Meeting (WAM), Flow Visualization Symposium: FED-Vol. 85, San Francisco, California, Dec. 1989, pp. 115-120

[22] Khalighi, B., Lee, Y.H., "Particle Tracking Velocimetry: An Automatic Image Processing Algorithm", Applied Optics Vol. 28, No. 20, 1989, pp. 4328-4332

[23] Khalighi, B., "Study of the Intake Swirl Process in an Engine Using Flow Visualization and Particle Tracking Velocimetry", ASME WAM, Flow Visualization Symposium: FED-Vol. 85, San Francisco, CA, Dec. 1989, pp. 37-48

[24] Chang, T.P., Tatterson, G.B., "An Automated Analysis Method for Complex Three Dimensional Mean Flow Fields", Flow Viz. III, Ann Arbor, Michigan, Sept. 1983, pp. 266-271

[25] Sheu, Y.H.E., Chang, T.P., Tatterson, G.B., Dickey, D.S., "A Three-Dimensional Measurement Technique for Turbulent Flows", Chem. Eng. Comm., Vol. 17, pp. 67-83, 1982

[26] Doi, J., Miyake, T., "hree-Dimensional Flow Analysis By On-Line Particle Tracking", Flow Viz. III, Ann Arbor, Michigan, Sept. 1983, pp. 83-87

[27] Hassan, Y., Blanchat, T., "Two Phase Flow Velocity Measurements Using Automated Based Imaging Pulsed Laser Velocimetry", Fifth International Symposium on Flow Visualization (Flow Viz. V), Lisbon, Portugal, July 1990, paper 12.5

[28] Schaffer, F.D., Ekmann, J., Ramer, E.R., "Development of Pulsed Laser Velocimetry Systems Utilizing Photoelectric Image Sensors", AIAA/ASME/ASCE/SIAM/APS 1st Fluid Dynamics Congress, Cincinnati, Ohio, July, 1988, paper AIAA-88-3777

[29] Cenedese, A., Palmieri, G., Romano, G.P., "Turbulent Intensity Evaluation With PIV", Flow Viz. V, Lisbon, Portugal, July 1990, paper 15.5

[30] Adrian, R., Offutt, W., Landreth, C.C., "Studies of Liquid Turbulence Using Double-Pulsed Particle Correlation", Flow Viz. V, Lisbon, Portugal, July 1990, paper 15.4

[31] Braun, M.J., Batur, C., Ida, N., Rose, B., Hendricks, R.C., Mullen, R.L., "Noninvasive Laser Based Method in Flow Visualization and Evaluation in Bearings", Intsitution of Mechanical Engineers Proceedings Vol. 1, 1987, paper C 188/87

[32] Braun, M.J., Batur, C., Karavelakis, G., "Digital Image Processing for Quantification through Full Field Flow Tracing (FFFT) in Narrow Geometries at Low Reynolds Numbers", AIAA/ASME/SIAM/APS 1st Fluid Dynamic Congress-Vol. 3, Cincinnati, Ohio, July 1988, pp. 1965-1975/paper AIAA-88-3781-CP

[33] Prandtl, L., Tietsens, O.G., "Applied Hydro- and Aeromechanics", McGraw-Hill, 1934, Translated from German Edition, Springer, 1931

[34] Batchelor, F.E., "An Introduciton to Fluid Dynamics", Cambridge University Press, 1967

[35] Kobayashi, T., Ishihara, T., Sasaki, N., "Automatic Analysis of Photographs of Trace Particles by Microcomputer System", Flow Viz. III, Ann Arbor, Michigan, Sept. 1983, pp. 261-265

[36] Kimura, I., Takamori, T., "Image Processing of Flow Around a Circular Cylinder by Using Correlation Technique", Flow Viz. IV, Paris, France, Aug. 1986, pp. 221-226

[37] Coutanceau, M., Menard, C., "Visualization of the Flow Development Around a Circular Cylinder Impulsively Subjected to a Combined Motion of Rotation and Translation", Flow Viz. III, Ann Arbor, Michigan, Sept. 1983, pp. 54-58

[38] Monnet, P., Coutanceau, M., "The Use of Visualization as a Guide in the Numerical Determination of the FLow Around An Abruptly Accelerated Elliptic Cylinder or Airfoil", Flow Viz. III, Ann Arbor, Michigan, Sept. 1983, pp. 135-140

[39] Fergusson, J.G., "Brushes as High Performance Gas Turbine Seals", ASME Gas Turbine and Aeroengine Congress, Amsterdam, Netherlands, June, 1988, paper 88-GT-182

[40] Flower, R., "Brush Seal Development System", Cross Mfg. Co. Ltd., Wiltshire, England, Private Communication, 1988

[41] Gorelov, G.M., Reznik, V.E., Tsibizov, V.I., "An Experimental Study of the Rate Characteristics of Brush Seals in Comparison with Labyrinth Seals", Soviet Aeronautics: Vol. 31, No. 4, 1988, pp. 43-46

[42] Chupp, R.E., Nelson, Lt. P., "Evaluation of Brush Seals for Limited Life Engines", Wright Patterson Air Force Base, Dayton, Ohio, Private Communication, 1990

[43] Ergun, S., "Fluid Flow Through Packed Columns", Chemical Eng. Progress-Vol. 48, 1952, pp. 89-94

[44] Poulikakos, D., Kazmierczak, M., "Forced Convection in a Duct Filled with a Porous Medium", ASME Journal of Heat Transfer-Vol. 109, 1987,pp. 653-662

[45] Renkin, K.J., Poulikakos, D., "Experiment and Analysis of Forced Convective Heat Transfer in a Packed Bed of Spheres", Int'l Journal of Heat and Mass Transfer-Vol. 31, 1988, pp. 1309-1408

[46] Vafai, K., Alkire, R.L., Tien, C.L., "An Experimental Investigation of Heat Transfer in Variable Porosity Media", Journal of Heat Transfer-Vol. 107, 1985, pp. 642-647

[47] Braun, M.J., Canacci, V.A., Hendricks, R.C., "Flow Visualization and Quantitative Velocity and Pressure Measurements in Simulated Single and Double Brush Seals", STLE 45th Annual Meeting, Denver, Colorado, May 1990, paper 90-AM-7F-2

[48] Braun, M.J., Canacci, V.A., Hendricks, R.C., "Flow Visualization and Motion Analysis for a Series of Four Sequential Brush Seals", AIAA/SAE/ASME/ASEE 26th Joint Propulsion Conference, Orlando, Florida, July 1990, paper AIAA 90-2482

[49] Braun, M.J., Hendricks, R.C., Canacci, V.A., "Flow Visualization in a Simulated Brush Seal", 35th ASME International Gas Turbine and Aeroengine Congress and Exposition, Brussels, Belgium, June, 1990, paper 90-GT-217

[50] Braun, M.J., Hendricks, R.C., Canacci, V.A., "Non-Intrusive Qualitative and Quantitative Flow Characteristization and Bulk Flow Model For Brush Seals", Japan International Tribology Conference Proceedings , Nagoya, Japan, Oct. 1990, pp. 1611-1616, paper 3D1-3

[51] Gladden, H.J., Melis, M.E., Mockler, T.T., Tong, M., "Thermal/Structural Analysis of Several Hydrogen-Cooled Leading-Edge Concepts for Hypersonic Flight Vehicles", 28th Aerospace Sciences Meeting, Reno, Nevada, Jan. 1990, paper AIAA-90-0053

[52] Gladden, H.J., Melis, M.E., Mockler, T.T., Tong, M. "hermal/Structural Analyses and Testing of a Hydrogen Cooled Strut Leading Edge", 8th National Aerospace Plane Technology Symposium, March 1990, paper 73

[53] Braun, M.J., Canacci, V.A., Russell, L.M., Hendricks, R.C., "Laser Based Computer Aided Non-Intrusive Technique for Full Flow Field Characterization in Macroscopic Curved Channels", ASME WAM, Flow Visualization Symposium: FED-Vol. 85, San Francisco, California, Dec. 1989, pp. 15-22

[54] Schaffer, F.D., Ramer, E.R., "Pulsed-Laser Imaging of Particle-Wall Collisions", Proceedings of Int'l Conference on Mechanics of Two-Phase Flows, Taipei, Japan, June 1989

[55] Treider, B., Humphrey, J.A.C., Carey, V.P., "On the Flow Past an Array of Staggered Ribs in a Channel", Flow Viz. V, Lisbon, Portugal, July 1990, paper 4.3

[56] Kawaguchi, Y., Suzuki, K., Sato, T., "Heat Transfer Promotion with a Cylinder Array Located Near the Wall", Int'l Journal of Heat and Fluid Flow-Vol. 6 No. 4, 1985, pp. 256-264

[57] Kamemoto, K., Oda, Y., Aizawa, M., "Characteristics of the Flow Around a Bluff Body Near a Plane Surface", JSME (Japan), Vol. 27, No. 230, pp. 1637-1643, 1984

[58] Yao, M., Nakatani, M., Suzuki, K., "Flow Visualization and Heat Transfer Experiments in a duct with a Staggered Array of Cylinders", Experimental Thermal and Fluid Science-Vol. 2, 1989, pp. 193-200

[59] White, F.M., "Heat & Mass Transfer", Addison-Wesley Publishing, 1988

[60] Chapman, A.J., "Fundamentals of Heat Transfer", Macmillan Publishing, 1987

[61] Zhukauskas, A., "Heat Transfer for Tubes in Crossflow", Advances in Heat Transfer, New York, Academic Press, 1972, p. 93

[62] Snyder, P.H., Roelke, R.J., "The Design of an Air-Cooled Metallic High Temperature Radial Turbine", AIAA/ASME/SAE/ASEE 24th Joint Propulsion Conference, Boston, Massachusetts, July, 1988, paper AIAA-88-2872

[63] Kumar, G.N., Roelke, R.J., Meitner, P.L., "A Generalized One Dimensional Computer Code for Turbomachinery Cooling Passage Flow Calculations", AIAA/ASME/SAE/ASEE 25th Joint Propulsion Conference, Monterey, California, July 1989, NASA Tech. Mem. 102079

[64] Braun, M.J., Canacci, V.A., Russell, L.M., "Non-Intrusive Laser Based Computer Aided High Speed Flow Visualization in an Air Tunnel", Flow Viz. V, Lisbon, Portugal, July 1990, paper 6.1

[65] Diemunsch, G., Prenel, J.P., "A Compact Light Sheet Generator For Flow Visualizations", Optics and Laser Technology, Vol. 19, No. 3, June 1987

[66] Bulzan, D., Hippensteele, S., Russell, L., Thurman, D., "Particle Size Spectrums", Private Communications, 1990-1991

[67] Drain, D.L., "The Laser Doppler Technique", Wiley International, 1982

[68] Remiarz, R.J., Agarwal, J.K., Quant, F.R., Sem, G.J. (TSI Incorporated), "APS 33 Aerodynamic Particle Sizer Instruction Manual", Jan. 1983, Revision A

[69] Rudoff, R.C. & Bachalo, W.D., "Seed Particle Response and Size Characterization in High Speed Flows", Laser Anemometry Advances & Applications, Cleveland, 1991

[70] Sheun, J-S., Solomon, A.S.P., Faeth, G.M., "The Structure of Dilute Combusting Sprays", NASA Contractor Report N85-15728, 1985

[71] Bulzan, D., Thurman, D., "Droplet Sizing Calculations"; Private Communications, 1991

[72] Kline, McClintock, "Uncertainty Error Analysis"

[73] Coleman, H.W., Steele, W.G., "Experimentation and Uncertainty Analysis for Engineers", John Wiley & Sons, 1989

[74] Braun (Negraunu), M.J. & Naraghi, M.H.N., "Prediction of Droplet Entrainment in a Flow Field With Irregular Boundaries", I. Mech. Eng. Proceedings of Conference on Gas Borne Particles, Paper C66/81, pp. 47-58, June 30-July 2, 1981, St. Catherine's College, Oxford, England

[75] Aggarwal, S.K. & Chitre, S., "Computations of Turbulent Evaporating Sprays", AIAA/ASME/SAE/ ASEE 25th Joint Propulsion Conference, Monterey, CA, July 10-12, 1989, Paper No. AIAA 89-2433

[76] Zaman, K.B., Potapczuk, M.G., "The Low Frequency Oscillation in the Flow over a NACA 0012 Airfoil With an Iced Leading Edge", NASA TM-102018, Low Reynolds Number Aerodynamics, University of Notre Dame, June 5-7, 1989

[77] Beer, F.B., Johnston, Jr., E.R., "Vector Mechanics for Engineers: Dynamics", 4th Edition, McGraw Hill, 1984

[78] Rudoff, R.C., Bachalo, E.J., Bacholo, W.D., Oldenburg, J.R., "Performance of the Phase Doppler Particle Analyzer Icing Cloud Droplet Sizing Probe in the NASA Lewis Icing Research Tunnel", 30th AIAA Aerospace Sciences Meeting, Reno, Nevada, January 6-9, 1992

# APPENDICES

# APPENDIX A

## EXAMPLES OF THE FILES CREATED BY THE COMPUTER PROGRAMS

The following pages document the information contained in each of the four files created by the CIIQ computer programs discussed in Chapter 4. Example files are shown for the files .bnd, .tra, .rsl, and .inp.

EXAMPLE .bnd FILE:

Columns A and B are the digitized X and Y coordinates in pixels. Column C is a flag that indicates what points are related and form continuous lines. In the .bnd files, these continuous lines are boundaries. Columns D and E are modified X and Y coordinates respectively for use in the other programs.

| A | B | C | D | E |
|---|---|---|---|---|
| 463 | 77 | 1 | 904.30 | 837.50 |
| 17 | 78 | 1 | 33.20 | 835.42 |
| 15 | 120 | 2 | 29.30 | 747.92 |
| 466 | 126 | 2 | 910.16 | 735.42 |

EXAMPLE .tra FILE

As was the case for the .bnd files, the columns A and B refer to the digitized X and Y coordinates in pixels. Column C is a flag that indicates which trajectory the coordinates belong to. Again, columns D and E are modified X and Y coordinates.

| A | B | C | D | E |
|---|---|---|---|---|
| 23 | 174 | 3 | 44.92 | 635.42 |
| 76 | 163 | 3 | 148.44 | 658.33 |
| 134 | 152 | 3 | 261.72 | 681.25 |
| 191 | 141 | 3 | 373.05 | 704.17 |
| 248 | 128 | 3 | 484.38 | 731.25 |
| 302 | 116 | 3 | 589.84 | 756.25 |
| 364 | 99 | 3 | 710.94 | 791.67 |
| 418 | 86 | 3 | 816.41 | 818.75 |
| 161 | 437 | 4 | 314.45 | 87.50 |
| 212 | 425 | 4 | 414.06 | 112.50 |
| 266 | 415 | 4 | 519.53 | 133.33 |
| 316 | 405 | 4 | 617.19 | 154.17 |
| 357 | 397 | 4 | 697.27 | 170.83 |
| 416 | 383 | 4 | 812.50 | 200.00 |
| 51 | 423 | 5 | 99.61 | 116.67 |
| 102 | 418 | 5 | 199.22 | 127.08 |
| 160 | 414 | 5 | 312.50 | 135.42 |
| 210 | 408 | 5 | 410.16 | 147.92 |
| 262 | 402 | 5 | 511.72 | 160.42 |
| 307 | 398 | 5 | 599.61 | 168.75 |
| 363 | 395 | 5 | 708.98 | 175.00 |
| 37 | 369 | 6 | 72.27 | 229.17 |
| 88 | 357 | 6 | 171.88 | 254.17 |
| 149 | 348 | 6 | 291.02 | 272.92 |
| 210 | 339 | 6 | 410.16 | 291.67 |
| 269 | 329 | 6 | 525.39 | 312.50 |
| 325 | 318 | 6 | 634.77 | 335.42 |
| 91 | 206 | 7 | 177.73 | 568.75 |
| 151 | 199 | 7 | 294.92 | 583.33 |
| 207 | 191 | 7 | 404.30 | 600.00 |
| 262 | 184 | 7 | 511.72 | 614.58 |
| 326 | 176 | 7 | 636.72 | 631.25 |
| 375 | 167 | 7 | 732.42 | 650.00 |
| 431 | 160 | 7 | 841.80 | 664.58 |
| 86 | 329 | 8 | 167.97 | 312.50 |
| 150 | 324 | 8 | 292.97 | 322.92 |
| 215 | 316 | 8 | 419.92 | 339.58 |
| 274 | 308 | 8 | 535.16 | 356.25 |
| 334 | 305 | 8 | 652.34 | 362.50 |
| 393 | 300 | 8 | 767.58 | 372.92 |
| 454 | 293 | 8 | 886.72 | 387.50 |
| 64 | 293 | 9 | 125.00 | 387.50 |
| 122 | 280 | 9 | 238.28 | 414.58 |
| 182 | 269 | 9 | 355.47 | 437.50 |
| 242 | 259 | 9 | 472.66 | 458.33 |
| 304 | 246 | 9 | 593.75 | 485.42 |
| 360 | 235 | 9 | 703.13 | 508.33 |
| 422 | 222 | 9 | 824.22 | 535.42 |

| A | B | C | D | E |
|---|---|---|---|---|
| 130 | 453 | 11 | 253.91 | 54.17 |
| 187 | 445 | 11 | 365.23 | 70.83 |
| 250 | 436 | 11 | 488.28 | 89.58 |
| 309 | 427 | 11 | 603.52 | 108.33 |
| 369 | 419 | 11 | 720.70 | 125.00 |
| 428 | 408 | 11 | 835.94 | 147.92 |
| 48 | 258 | 12 | 93.75 | 460.42 |
| 112 | 247 | 12 | 218.75 | 483.33 |
| 177 | 234 | 12 | 345.70 | 510.42 |
| 239 | 222 | 12 | 466.80 | 535.42 |
| 303 | 211 | 12 | 591.80 | 558.33 |
| 364 | 200 | 12 | 710.94 | 581.25 |
| 431 | 184 | 12 | 841.80 | 614.58 |
| 54 | 284 | 13 | 105.47 | 406.25 |
| 118 | 271 | 13 | 230.47 | 433.33 |
| 182 | 260 | 13 | 355.47 | 456.25 |
| 242 | 249 | 13 | 472.66 | 479.17 |
| 303 | 240 | 13 | 591.80 | 497.92 |
| 360 | 228 | 13 | 703.13 | 522.92 |
| 420 | 215 | 13 | 820.31 | 550.00 |
| 110 | 406 | 15 | 214.84 | 152.08 |
| 172 | 398 | 15 | 335.94 | 168.75 |
| 234 | 388 | 15 | 457.03 | 189.58 |
| 293 | 379 | 15 | 572.27 | 208.33 |
| 354 | 373 | 15 | 691.41 | 220.83 |
| 412 | 360 | 15 | 804.69 | 247.92 |
| 469 | 351 | 15 | 916.02 | 266.67 |
| 86 | 183 | 16 | 167.97 | 616.67 |
| 143 | 175 | 16 | 279.30 | 633.33 |
| 201 | 166 | 16 | 392.58 | 652.08 |
| 261 | 159 | 16 | 509.77 | 666.67 |
| 313 | 149 | 16 | 611.33 | 687.50 |
| 372 | 140 | 16 | 726.56 | 706.25 |
| 423 | 130 | 16 | 826.17 | 727.08 |

A - "X" Coordinate of Pixels
B - "Y" Coordinate of Pixels
C - Trajectory Flag or Label
D - "X" Coordinate Modified (1-1000)
E - "Y" Coordinate Modified (1-1000)

## EXAMPLE .rsl FILE

The .rsl file contains all the points that make up each of the trajectories, as well as the velocities and accelerations at each of those points. These velocities and accelerations provide both the X and Y direction component, and well as the resultants. The example shown for 15 trajectories is average in size, and spans pages 175-178.

BOUNDARY FILE: vcupst3a.bnd  TRAJECTORY FILE: vcupst3a.tra

OUTPUT FILE: vcupst3a.rsl

Magnification ratio = 12.27:1  (screen:actual)

(device=tv)

| x | y | traj | x (mm) | y (mm) | |
|---|---|---|---|---|---|
| 463 | 77 | 1 | 17.739 | 12.875 | boundary point |
| 17 | 78 | 1 | 0.651 | 12.843 | boundary point |
| 15 | 120 | 2 | 0.575 | 11.502 | boundary point |
| 466 | 126 | 2 | 17.854 | 11.310 | boundary point |

(device=tv)

| x | y | traj | x (mm) | y (mm) | vx (cm/s)<br>vy (cm/s) | v (cm/s) | ax (cm/s2)<br>ay (cm/s2) | a (cm/s2) |
|---|---|---|---|---|---|---|---|---|
| 23 | 174 | 3 | 0.881 | 9.776 | 6.231<br>0.972 | 6.306 | 5.020<br>1.529 | 5.248 |
| 76 | 163 | 3 | 2.912 | 10.128 | 6.379<br>1.026 | 6.461 | 3.867<br>1.747 | 4.244 |
| 134 | 152 | 3 | 5.134 | 10.479 | 6.488<br>1.088 | 6.579 | 2.715<br>1.966 | 3.352 |
| 191 | 141 | 3 | 7.318 | 10.831 | 6.560<br>1.158 | 6.661 | 1.562<br>2.185 | 2.686 |
| 248 | 128 | 3 | 9.502 | 11.246 | 6.592<br>1.234 | 6.707 | 0.409<br>2.403 | 2.438 |
| 302 | 116 | 3 | 11.571 | 11.629 | 6.587<br>1.318 | 6.717 | -0.743<br>2.622 | 2.725 |
| 364 | 99 | 3 | 13.946 | 12.173 | 6.543<br>1.409 | 6.693 | -1.896<br>2.841 | 3.415 |
| 418 | 86 | 3 | 16.015 | 12.588 | 6.461<br>1.507 | 6.634 | -3.049<br>3.059 | 4.319 |
| 161 | 437 | 4 | 6.169 | 1.374 | 6.778<br>1.393 | 6.919 | -30.200<br>-13.367 | 33.026 |
| 212 | 425 | 4 | 8.123 | 1.757 | 5.962<br>1.038 | 6.052 | -18.711<br>-7.939 | 20.325 |
| 266 | 415 | 4 | 10.192 | 2.077 | 5.530<br>0.864 | 5.597 | -7.222<br>-2.510 | 7.646 |
| 316 | 405 | 4 | 12.107 | 2.396 | 5.481<br>0.871 | 5.550 | 4.266<br>2.918 | 5.169 |

# EXAMPLE .rsl FILE (continued)

| (device=tv) x | y | traj | x (mm) | y (mm) | vx (cm/s) vy (cm/s) | v (cm/s) | ax (cm/s2) ay (cm/s2) | a (cm/s2) |
|---|---|---|---|---|---|---|---|---|
| 357 | 397 | 4 | 13.678 | 2.652 | 5.815<br>1.058 | 5.910 | 15.755<br>8.346 | 17.829 |
| 416 | 383 | 4 | 15.939 | 3.099 | 6.531<br>1.427 | 6.685 | 27.244<br>13.774 | 30.528 |
| 51 | 423 | 5 | 1.954 | 1.821 | 6.559<br>0.321 | 6.567 | -11.566<br>5.068 | 12.628 |
| 102 | 418 | 5 | 3.908 | 1.981 | 6.221<br>0.458 | 6.238 | -8.696<br>3.151 | 9.250 |
| 160 | 414 | 5 | 6.130 | 2.109 | 5.979<br>0.531 | 6.002 | -5.826<br>1.234 | 5.955 |
| 210 | 408 | 5 | 8.046 | 2.300 | 5.833<br>0.540 | 5.858 | -2.956<br>-0.684 | 3.034 |
| 262 | 402 | 5 | 10.038 | 2.492 | 5.782<br>0.485 | 5.802 | -0.087<br>-2.601 | 2.602 |
| 307 | 398 | 5 | 11.762 | 2.620 | 5.827<br>0.367 | 5.838 | 2.783<br>-4.518 | 5.307 |
| 363 | 395 | 5 | 13.908 | 2.716 | 5.967<br>0.184 | 5.970 | 5.653<br>-6.435 | 8.566 |
| 37 | 369 | 6 | 1.418 | 3.546 | 5.503<br>1.241 | 5.641 | 36.107<br>-9.287 | 37.283 |
| 88 | 357 | 6 | 3.372 | 3.930 | 6.479<br>0.993 | 6.555 | 22.502<br>-5.614 | 23.192 |
| 149 | 348 | 6 | 5.709 | 4.217 | 7.003<br>0.867 | 7.056 | 8.896<br>-1.941 | 9.105 |
| 210 | 339 | 6 | 8.046 | 4.505 | 7.073<br>0.864 | 7.125 | -4.710<br>1.733 | 5.018 |
| 269 | 329 | 6 | 10.307 | 4.824 | 6.689<br>0.982 | 6.761 | -18.315<br>5.406 | 19.096 |
| 325 | 318 | 6 | 12.452 | 5.176 | 5.852<br>1.224 | 5.978 | -31.921<br>9.079 | 33.187 |
| 91 | 206 | 7 | 3.487 | 8.754 | 6.626<br>0.641 | 6.657 | 2.148<br>1.924 | 2.883 |
| 151 | 199 | 7 | 5.785 | 8.978 | 6.669<br>0.698 | 6.706 | 0.420<br>1.442 | 1.502 |
| 207 | 191 | 7 | 7.931 | 9.233 | 6.654<br>0.738 | 6.695 | -1.309<br>0.960 | 1.623 |
| 262 | 184 | 7 | 10.038 | 9.457 | 6.582<br>0.762 | 6.626 | -3.037<br>0.479 | 3.074 |
| 326 | 176 | 7 | 12.490 | 9.712 | 6.452<br>0.769 | 6.498 | -4.765<br>-0.003 | 4.765 |

EXAMPLE .rsl FILE (continued)

| device=tv) x | y | traj | x (mm) | y (mm) | vx (cm/s) vy (cm/s) | v (cm/s) | ax (cm/s2) ay (cm/s2) | a (cm/s2) |
|---|---|---|---|---|---|---|---|---|
| 375 | 167 | 7 | 14.368 | 10.000 | 6.264<br>0.761 | 6.310 | -6.493<br>-0.485 | 6.511 |
| 431 | 160 | 7 | 16.513 | 10.224 | 6.019<br>0.737 | 6.064 | -8.222<br>-0.966 | 8.278 |
| 86 | 329 | 8 | 3.295 | 4.824 | 7.751<br>0.727 | 7.786 | -13.867<br>-2.459 | 14.084 |
| 150 | 324 | 8 | 5.747 | 4.984 | 7.347<br>0.653 | 7.376 | -10.422<br>-1.982 | 10.608 |
| 215 | 316 | 8 | 8.238 | 5.240 | 7.057<br>0.595 | 7.082 | -6.976<br>-1.505 | 7.136 |
| 274 | 308 | 8 | 10.498 | 5.495 | 6.882<br>0.553 | 6.904 | -3.530<br>-1.027 | 3.677 |
| 334 | 305 | 8 | 12.797 | 5.591 | 6.821<br>0.527 | 6.842 | -0.084<br>-0.550 | 0.556 |
| 393 | 300 | 8 | 15.057 | 5.751 | 6.876<br>0.516 | 6.895 | 3.361<br>-0.073 | 3.362 |
| 454 | 293 | 8 | 17.395 | 5.974 | 7.045<br>0.522 | 7.065 | 6.807<br>0.405 | 6.819 |
| 64 | 293 | 9 | 2.452 | 5.974 | 6.703<br>1.235 | 6.816 | 3.784<br>-3.900 | 5.434 |
| 122 | 280 | 9 | 4.674 | 6.390 | 6.810<br>1.128 | 6.903 | 2.632<br>-2.463 | 3.605 |
| 182 | 269 | 9 | 6.973 | 6.741 | 6.878<br>1.070 | 6.961 | 1.481<br>-1.026 | 1.802 |
| 242 | 259 | 9 | 9.272 | 7.061 | 6.909<br>1.060 | 6.989 | 0.329<br>0.411 | 0.526 |
| 304 | 246 | 9 | 11.648 | 7.476 | 6.900<br>1.098 | 6.987 | -0.823<br>1.848 | 2.023 |
| 360 | 235 | 9 | 13.793 | 7.827 | 6.854<br>1.183 | 6.955 | -1.974<br>3.285 | 3.833 |
| 422 | 222 | 9 | 16.169 | 8.243 | 6.769<br>1.317 | 6.896 | -3.126<br>4.722 | 5.663 |
| 130 | 453 | 11 | 4.981 | 0.863 | 6.609<br>0.845 | 6.663 | 9.329<br>-1.666 | 9.477 |
| 187 | 445 | 11 | 7.165 | 1.118 | 6.856<br>0.809 | 6.904 | 5.499<br>-0.548 | 5.527 |
| 250 | 436 | 11 | 9.579 | 1.406 | 6.976<br>0.809 | 7.022 | 1.669<br>0.569 | 1.763 |
| 309 | 427 | 11 | 11.839 | 1.693 | 6.968<br>0.847 | 7.019 | -2.161<br>1.687 | 2.742 |

EXAMPLE .rsl FILE (continued)

| device=tv) x | y | traj | x (mm) | y (mm) | vx (cm/s) vy (cm/s) | v (cm/s) | ax (cm/s2) ay (cm/s2) | a (cm/s2) |
|---|---|---|---|---|---|---|---|---|
| 369 | 419 | 11 | 14.138 | 1.949 | 6.832<br>0.921 | 6.894 | -5.991<br>2.805 | 6.615 |
| 428 | 408 | 11 | 16.398 | 2.300 | 6.568<br>1.033 | 6.649 | -9.822<br>3.923 | 10.576 |
| 48 | 258 | 12 | 1.839 | 7.093 | 7.630<br>1.284 | 7.737 | -8.691<br>-4.860 | 9.958 |
| 112 | 247 | 12 | 4.291 | 7.444 | 7.388<br>1.154 | 7.478 | -5.821<br>-2.943 | 6.523 |
| 177 | 234 | 12 | 6.782 | 7.859 | 7.242<br>1.088 | 7.323 | -2.951<br>-1.026 | 3.125 |
| 239 | 222 | 12 | 9.157 | 8.243 | 7.191<br>1.086 | 7.273 | -0.082<br>0.892 | 0.895 |
| 303 | 211 | 12 | 11.609 | 8.594 | 7.236<br>1.148 | 7.327 | 2.788<br>2.809 | 3.958 |
| 364 | 200 | 12 | 13.946 | 8.946 | 7.377<br>1.273 | 7.486 | 5.658<br>4.726 | 7.372 |
| 431 | 184 | 12 | 16.513 | 9.457 | 7.614<br>1.463 | 7.753 | 8.528<br>6.643 | 10.810 |
| 54 | 284 | 13 | 2.069 | 6.262 | 7.617<br>1.384 | 7.742 | -9.516<br>-8.558 | 12.798 |
| 118 | 271 | 13 | 4.521 | 6.677 | 7.329<br>1.147 | 7.418 | -7.794<br>-5.682 | 9.646 |
| 182 | 260 | 13 | 6.973 | 7.029 | 7.098<br>1.005 | 7.169 | -6.072<br>-2.807 | 6.689 |
| 242 | 249 | 13 | 9.272 | 7.380 | 6.924<br>0.960 | 6.990 | -4.350<br>0.069 | 4.351 |
| 303 | 240 | 13 | 11.609 | 7.668 | 6.808<br>1.010 | 6.882 | -2.628<br>2.945 | 3.947 |
| 360 | 228 | 13 | 13.793 | 8.051 | 6.749<br>1.156 | 6.847 | -0.906<br>5.821 | 5.891 |
| 420 | 215 | 13 | 16.092 | 8.466 | 6.747<br>1.398 | 6.891 | 0.816<br>8.697 | 8.735 |
| 110 | 406 | 15 | 4.215 | 2.364 | 7.157<br>0.887 | 7.211 | -1.631<br>-1.916 | 2.516 |
| 172 | 398 | 15 | 6.590 | 2.620 | 7.093<br>0.839 | 7.142 | -2.209<br>-0.958 | 2.408 |
| 234 | 388 | 15 | 8.966 | 2.939 | 7.009<br>0.823 | 7.057 | -2.788<br>0.001 | 2.788 |
| 293 | 379 | 15 | 11.226 | 3.227 | 6.907<br>0.839 | 6.957 | -3.366<br>0.959 | 3.500 |

EXAMPLE .inp FILE

This is a portion of a file that is imported into the Drafix CAD package where the entire flow field can be assembled. Each line of text shown describes one drawn line that appears on the screen, and is in the format of the CAD software.

```
     0     1     0   10.307    4.824   12.452    5.176
line
     0     1     0    3.487    8.754    5.785    8.978
line
     0     1     0    5.785    8.978    7.931    9.233
line
     0     1     0    7.931    9.233   10.038    9.457
line
     0     1     0   10.038    9.457   12.490    9.712
line
     0     1     0   12.490    9.712   14.368   10.000
line
     0     1     0   14.368   10.000   16.513   10.224
line
     0     1     0    3.295    4.824    5.747    4.984
line
     0     1     0    5.747    4.984    8.238    5.240
line
     0     1     0    8.238    5.240   10.498    5.495
line
     0     1     0   10.498    5.495   12.797    5.591
line
     0     1     0   12.797    5.591   15.057    5.751
line
     0     1     0   15.057    5.751   17.395    5.974
line
     0     1     0    2.452    5.974    4.674    6.390
line
     0     1     0    4.674    6.390    6.973    6.741
line
     0     1     0    6.973    6.741    9.272    7.061
line
     0     1     0    9.272    7.061   11.648    7.476
line
     0     1     0   11.648    7.476   13.793    7.827
line
     0     1     0   13.793    7.827   16.169    8.243
line
     0     1     0    4.981    0.863    7.165    1.118
line
     0     1     0    7.165    1.118    9.579    1.406
line
     0     1     0    9.579    1.406   11.839    1.693
line
     0     1     0   11.839    1.693   14.138    1.949
line
     0     1     0   14.138    1.949   16.398    2.300
line
     0     1     0    1.839    7.093    4.291    7.444
line
     0     1     0    4.291    7.444    6.782    7.859
line
     0     1     0    6.782    7.859    9.157    8.243
line
```

# APPENDIX B

## TIME CONSTANTS AND RESPONSE TIMES FOR CABOSIL AND LATEX PARTICLES

The following tables have been generated using the equations in Section 6.2. These tables contain the raw data used to produce Figures 83 and 84. The time constants and response times for latex and Cabosil particles in air are shown for various values of $\beta$ (see Section 6.2).

$\mu$= 18*10e-6 Dynamic Viscosity of Air

Rho= 1800 kg/m^3 Density of Cabosil Particles
Rho= 906 kg/m^3 Density of Latex Particles

Velocity of Particle=5% Velocity of Fluid

| (V=5%*U) | CABOSIL PARTS. | | LATEX PARTICLES | |
|---|---|---|---|---|
| DIAM ($\mu$m) | TIME CONSTANT ($\mu$sec) | TIME RESPONSE ($\mu$sec) | TIME CONSTANT ($\mu$sec) | TIME RESPONSE ($\mu$sec) |
| 1 | 5.55 | 0.28496 | 2.80 | 0.14343 |
| 2 | 22.22 | 1.13985 | 11.18 | 0.57372 |
| 3 | 50.00 | 2.56466 | 25.17 | 1.29088 |
| 4 | 88.89 | 4.55940 | 44.74 | 2.29490 |
| 5 | 138.89 | 7.12407 | 69.91 | 3.58578 |
| 6 | 200.00 | 10.25866 | 100.67 | 5.16352 |
| 7 | 272.22 | 13.96317 | 137.02 | 7.02813 |
| 8 | 355.55 | 18.23761 | 178.96 | 9.17960 |
| 9 | 450.00 | 23.08198 | 226.50 | 11.61793 |
| 10 | 555.55 | 28.49627 | 279.63 | 14.34312 |

Velocity of Particle=10%*Velocity of Fluid

| (V=10%*U) | CABOSIL PARTS. | | LATEX PARTICLES | |
|---|---|---|---|---|
| DIAM ($\mu$m) | TIME CONSTANT ($\mu$sec) | TIME RESPONSE ($\mu$sec) | TIME CONSTANT ($\mu$sec) | TIME RESPONSE ($\mu$sec) |
| 1 | 5.55 | 0.58534 | 2.80 | 0.29462 |
| 2 | 22.22 | 2.34135 | 11.18 | 1.17848 |
| 3 | 50.00 | 5.26803 | 25.17 | 2.65157 |
| 4 | 88.89 | 9.36538 | 44.74 | 4.71391 |
| 5 | 138.89 | 14.63341 | 69.91 | 7.36548 |
| 6 | 200.00 | 21.07211 | 100.67 | 10.60630 |
| 7 | 272.22 | 28.68149 | 137.02 | 14.43635 |
| 8 | 355.55 | 37.46154 | 178.96 | 18.85564 |
| 9 | 450.00 | 47.41226 | 226.50 | 23.86417 |
| 10 | 555.55 | 58.53364 | 279.63 | 29.46193 |

Velocity of Particle=15% Velocity of Fluid

| (V=15%*U) | CABOSIL PARTS. | | LATEX PARTICLES | |
|---|---|---|---|---|
| DIAM ($\mu$m) | TIME CONSTANT ($\mu$sec) | TIME RESPONSE ($\mu$sec) | TIME CONSTANT ($\mu$sec) | TIME RESPONSE ($\mu$sec) |
| 1 | 5.55 | 0.90288 | 2.80 | 0.45445 |
| 2 | 22.22 | 3.61153 | 11.18 | 1.81780 |
| 3 | 50.00 | 8.12595 | 25.17 | 4.09006 |
| 4 | 88.89 | 14.44612 | 44.74 | 7.27122 |
| 5 | 138.89 | 22.57207 | 69.91 | 11.36127 |
| 6 | 200.00 | 32.50378 | 100.67 | 16.36024 |
| 7 | 272.22 | 44.24126 | 137.02 | 22.26810 |
| 8 | 355.55 | 57.78450 | 178.96 | 29.08486 |
| 9 | 450.00 | 73.13351 | 226.50 | 36.81053 |
| 10 | 555.55 | 90.28826 | 279.63 | 45.44510 |

Velocity of Particle=20%*Velocity of Fluid

| (V=20%*U) | CABOSIL PARTS. | | LATEX PARTICLES | |
|---|---|---|---|---|
| DIAM ($\mu$m) | TIME CONSTANT ($\mu$sec) | TIME RESPONSE ($\mu$sec) | TIME CONSTANT ($\mu$sec) | TIME RESPONSE ($\mu$sec) |
| 1 | 5.55 | 1.23969 | 2.80 | 0.62397 |
| 2 | 22.22 | 4.95874 | 11.18 | 2.49590 |
| 3 | 50.00 | 11.15718 | 25.17 | 5.61578 |
| 4 | 88.89 | 19.83498 | 44.74 | 9.98361 |
| 5 | 138.89 | 30.99215 | 69.91 | 15.59939 |
| 6 | 200.00 | 44.62871 | 100.67 | 22.46312 |
| 7 | 272.22 | 60.74463 | 137.02 | 30.57480 |
| 8 | 355.55 | 79.33993 | 178.96 | 39.93443 |
| 9 | 450.00 | 100.4146 | 226.50 | 50.54201 |
| 10 | 555.55 | 123.9686 | 279.63 | 62.39755 |

Velocity of Particle=25% Velocity of Fluid

| (V=25%*U) | CABOSIL PARTS. | | LATEX PARTICLES | |
|---|---|---|---|---|
| DIAM ($\mu$m) | TIME CONSTANT ($\mu$sec) | TIME RESPONSE ($\mu$sec) | TIME CONSTANT ($\mu$sec) | TIME RESPONSE ($\mu$sec) |
| 1 | 5.55 | 1.5982 | 2.80 | 0.80444 |
| 2 | 22.22 | 6.3929 | 11.18 | 3.21778 |
| 3 | 50.00 | 14.3841 | 25.17 | 7.24000 |
| 4 | 88.89 | 25.5717 | 44.74 | 12.87111 |
| 5 | 138.89 | 39.9558 | 69.91 | 20.11111 |
| 6 | 200.00 | 57.5364 | 100.67 | 28.96000 |
| 7 | 272.22 | 78.3134 | 137.02 | 39.41777 |
| 8 | 355.55 | 102.2287 | 178.96 | 51.48443 |
| 9 | 450.00 | 129.4570 | 226.50 | 65.16000 |
| 10 | 555.55 | 159.8234 | 279.63 | 80.44443 |

Velocity of Particle=30%*Velocity of Fluid

| (V=30%*U) | CABOSIL PARTS. | | LATEX PARTICLES | |
|---|---|---|---|---|
| DIAM ($\mu$m) | TIME CONSTANT ($\mu$sec) | TIME RESPONSE ($\mu$sec) | TIME CONSTANT ($\mu$sec) | TIME RESPONSE ($\mu$sec) |
| 1 | 5.55 | 1.98152 | 2.80 | 0.99737 |
| 2 | 22.22 | 7.92611 | 11.18 | 3.98947 |
| 3 | 50.00 | 17.83375 | 25.17 | 8.97632 |
| 4 | 88.89 | 31.70444 | 44.74 | 15.95790 |
| 5 | 138.89 | 49.53818 | 69.91 | 24.93422 |
| 6 | 200.00 | 71.33499 | 100.67 | 35.90528 |
| 7 | 272.22 | 97.09484 | 137.02 | 48.87107 |
| 8 | 355.55 | 126.8178 | 178.96 | 63.83160 |
| 9 | 450.00 | 160.5037 | 226.50 | 80.78687 |
| 10 | 555.55 | 198.1527 | 279.63 | 99.73687 |

Velocity of Particle=35% Velocity of Fluid

| (V=35%*U) | CABOSIL PARTS. | | LATEX PARTICLES | |
|---|---|---|---|---|
| DIAM ($\mu$m) | TIME CONSTANT ($\mu$sec) | TIME RESPONSE ($\mu$sec) | TIME CONSTANT ($\mu$sec) | TIME RESPONSE ($\mu$sec) |
| 1 | 5.55 | 2.3932 | 2.80 | 1.20460 |
| 2 | 22.22 | 9.5730 | 11.18 | 4.81839 |
| 3 | 50.00 | 21.5391 | 25.17 | 10.84137 |
| 4 | 88.89 | 38.2918 | 44.74 | 19.27355 |
| 5 | 138.89 | 59.8310 | 69.91 | 30.11492 |
| 6 | 200.00 | 86.1566 | 100.67 | 43.36549 |
| 7 | 272.22 | 117.2687 | 137.02 | 59.02524 |
| 8 | 355.55 | 153.1673 | 178.96 | 77.09420 |
| 9 | 450.00 | 193.8524 | 226.50 | 97.57234 |
| 10 | 555.55 | 239.3239 | 279.63 | 120.4597 |

Velocity of Particle=40%*Velocity of Fluid

| (V=40%*U) | CABOSIL PARTS. | | LATEX PARTICLES | |
|---|---|---|---|---|
| DIAM ($\mu$m) | TIME CONSTANT ($\mu$sec) | TIME RESPONSE ($\mu$sec) | TIME CONSTANT ($\mu$sec) | TIME RESPONSE ($\mu$sec) |
| 1 | 5.55 | 2.8379 | 2.80 | 1.4284 |
| 2 | 22.22 | 11.3517 | 11.18 | 5.7137 |
| 3 | 50.00 | 25.5413 | 25.17 | 12.8558 |
| 4 | 88.89 | 45.4067 | 44.74 | 22.8547 |
| 5 | 138.89 | 70.9480 | 69.91 | 35.7105 |
| 6 | 200.00 | 102.1651 | 100.67 | 51.4231 |
| 7 | 272.22 | 139.0581 | 137.02 | 69.9926 |
| 8 | 355.55 | 181.6269 | 178.96 | 91.4189 |
| 9 | 450.00 | 229.8716 | 226.50 | 115.7020 |
| 10 | 555.55 | 283.7920 | 279.63 | 142.8420 |

Velocity of Particle=45% Velocity of Fluid

| (V=45%*U) | CABOSIL PARTS. | | LATEX PARTICLES | |
|---|---|---|---|---|
| DIAM (μm) | TIME CONSTANT (μsec) | TIME RESPONSE (μsec) | TIME CONSTANT (μsec) | TIME RESPONSE (μsec) |
| 1 | 5.55 | 3.3213 | 2.80 | 1.67173 |
| 2 | 22.22 | 13.2853 | 11.18 | 6.68692 |
| 3 | 50.00 | 29.8919 | 25.17 | 15.04557 |
| 4 | 88.89 | 53.1411 | 44.74 | 26.74767 |
| 5 | 138.89 | 83.0329 | 69.91 | 41.79323 |
| 6 | 200.00 | 119.5674 | 100.67 | 60.18227 |
| 7 | 272.22 | 162.7445 | 137.02 | 81.91474 |
| 8 | 355.55 | 212.5643 | 178.96 | 106.9907 |
| 9 | 450.00 | 269.0267 | 226.50 | 135.4101 |
| 10 | 555.55 | 332.1316 | 279.63 | 167.1729 |

Velocity of Particle=50%*Velocity of Fluid

| (V=50%*U) | CABOSIL PARTS. | | LATEX PARTICLES | |
|---|---|---|---|---|
| DIAM (μm) | TIME CONSTANT (μsec) | TIME RESPONSE (μsec) | TIME CONSTANT (μsec) | TIME RESPONSE (μsec) |
| 1 | 5.55 | 3.3213 | 2.80 | 1.9382 |
| 2 | 22.22 | 15.4033 | 11.18 | 7.7530 |
| 3 | 50.00 | 34.6574 | 25.17 | 17.4442 |
| 4 | 88.89 | 61.6131 | 44.74 | 31.0119 |
| 5 | 138.89 | 96.2704 | 69.91 | 48.4561 |
| 6 | 200.00 | 138.6295 | 100.67 | 69.7768 |
| 7 | 272.22 | 188.6901 | 137.02 | 94.9740 |
| 8 | 355.55 | 246.4524 | 178.96 | 124.0477 |
| 9 | 450.00 | 311.9163 | 226.50 | 156.9979 |
| 10 | 555.55 | 385.0817 | 279.63 | 193.8245 |

Velocity of Particle=55% Velocity of Fluid

| (V=55%*U) | CABOSIL PARTS. | | LATEX PARTICLES | |
|---|---|---|---|---|
| DIAM ($\mu$m) | TIME CONSTANT ($\mu$sec) | TIME RESPONSE ($\mu$sec) | TIME CONSTANT ($\mu$sec) | TIME RESPONSE ($\mu$sec) |
| 1 | 5.55 | 4.4361 | 2.80 | 2.2329 |
| 2 | 22.22 | 17.7446 | 11.18 | 8.9315 |
| 3 | 50.00 | 39.9254 | 25.17 | 20.0958 |
| 4 | 88.89 | 70.9784 | 44.74 | 35.7258 |
| 5 | 138.89 | 110.9038 | 69.91 | 55.8216 |
| 6 | 200.00 | 159.7015 | 100.67 | 80.3831 |
| 7 | 272.22 | 217.3715 | 137.02 | 109.4103 |
| 8 | 355.55 | 283.9138 | 178.96 | 142.9033 |
| 9 | 450.00 | **359.3284** | 226.50 | 180.8062 |
| 10 | 555.55 | **443.6152** | 279.63 | 223.2864 |

Velocity of Particle=60%*Velocity of Fluid

| (V=60%*U) | CABOSIL PARTS. | | LATEX PARTICLES | |
|---|---|---|---|---|
| DIAM ($\mu$m) | TIME CONSTANT ($\mu$sec) | TIME RESPONSE ($\mu$sec) | TIME CONSTANT ($\mu$sec) | TIME RESPONSE ($\mu$sec) |
| 1 | 5.55 | 5.0905 | 2.80 | 2.5622 |
| 2 | 22.22 | 20.3602 | 11.18 | 10.2489 |
| 3 | 50.00 | 45.8145 | 25.17 | 23.0600 |
| 4 | 88.89 | 81.4481 | 44.74 | 40.9955 |
| 5 | 138.89 | 127.2626 | 69.91 | 64.0555 |
| 6 | 200.00 | 183.2582 | 100.67 | 92.2399 |
| 7 | 272.22 | 249.4347 | 137.02 | 125.5488 |
| 8 | 355.55 | 325.7922 | 178.96 | 163.9821 |
| 9 | 450.00 | **412.3309** | 226.50 | 207.5398 |
| 10 | 555.55 | **509.0503** | 279.63 | 256.2220 |

Velocity of Particle=65% Velocity of Fluid

| (V=65%*U) | CABOSIL PARTS. | | LATEX PARTICLES | |
|---|---|---|---|---|
| DIAM (μm) | TIME CONSTANT (μsec) | TIME RESPONSE (μsec) | TIME CONSTANT (μsec) | TIME RESPONSE (μsec) |
| 1 | 5.55 | 5.8323 | 2.80 | 2.9356 |
| 2 | 22.22 | 23.3294 | 11.18 | 11.7424 |
| 3 | 50.00 | 52.4911 | 25.17 | 26.4205 |
| 4 | 88.89 | 93.9175 | 44.74 | 46.9698 |
| 5 | 138.89 | 145.8086 | 69.91 | 73.3903 |
| 6 | 200.00 | 209.9644 | 100.67 | 105.6821 |
| 7 | 272.22 | 285.7849 | 137.02 | 143.8451 |
| 8 | 355.55 | **373.2701** | 178.96 | 187.8793 |
| 9 | 450.00 | **472.4200** | 226.50 | 237.7847 |
| 10 | 555.55 | **583.2344** | 279.63 | 293.5614 |

Velocity of Particle=70%*Velocity of Fluid

| (V=70%*U) | CABOSIL PARTS. | | LATEX PARTICLES | |
|---|---|---|---|---|
| DIAM (μm) | TIME CONSTANT (μsec) | TIME RESPONSE (μsec) | TIME CONSTANT (μsec) | TIME RESPONSE (μsec) |
| 1 | 5.55 | 6.6887 | 2.80 | 3.3667 |
| 2 | 22.22 | 26.7550 | 11.18 | 13.4667 |
| 3 | 50.00 | 60.1987 | 25.17 | 30.3000 |
| 4 | 88.89 | 107.0198 | 44.74 | 53.8667 |
| 5 | 138.89 | 167.2184 | 69.91 | 84.1667 |
| 6 | 200.00 | 240.7946 | 100.67 | 121.1999 |
| 7 | 272.22 | 327.7481 | 137.02 | 164.9666 |
| 8 | 355.55 | **428.0792** | 178.96 | 215.4665 |
| 9 | 450.00 | **541.7878** | 226.50 | 272.6998 |
| 10 | 555.55 | **668.8737** | 279.63 | **336.6665** |

Velocity of Particle=75% Velocity of Fluid

| (V=75%*U) | CABOSIL PARTS. | | LATEX PARTICLES | |
|---|---|---|---|---|
| DIAM ($\mu$m) | TIME CONSTANT ($\mu$sec) | TIME RESPONSE ($\mu$sec) | TIME CONSTANT ($\mu$sec) | TIME RESPONSE ($\mu$sec) |
| 1 | 5.55 | 7.7016 | 2.80 | 3.8765 |
| 2 | 22.22 | 30.8065 | 11.18 | 15.5060 |
| 3 | 50.00 | 69.3147 | 25.17 | 34.8884 |
| 4 | 88.89 | 123.2262 | 44.74 | 62.0238 |
| 5 | 138.89 | 192.5408 | 69.91 | 96.9122 |
| 6 | 200.00 | 277.2589 | 100.67 | 139.5536 |
| 7 | 272.22 | **377.3801** | 137.02 | 189.9480 |
| 8 | 355.55 | **492.9047** | 178.96 | 248.0953 |
| 9 | 450.00 | **623.8325** | 226.50 | 313.9957 |
| 10 | 555.55 | **770.1634** | 279.63 | **387.6489** |

Velocity of Particle=80%*Velocity of Fluid

| (V=80%*U) | CABOSIL PARTS. | | LATEX PARTICLES | |
|---|---|---|---|---|
| DIAM ($\mu$m) | TIME CONSTANT ($\mu$sec) | TIME RESPONSE ($\mu$sec) | TIME CONSTANT ($\mu$sec) | TIME RESPONSE ($\mu$sec) |
| 1 | 5.55 | 8.9413 | 2.80 | 4.5005 |
| 2 | 22.22 | 35.7653 | 11.18 | 18.0019 |
| 3 | 50.00 | 80.4719 | 25.17 | 40.5042 |
| 4 | 88.89 | 143.0611 | 44.74 | 72.0074 |
| 5 | 138.89 | 223.5330 | 69.91 | 112.5116 |
| 6 | 200.00 | 321.8876 | 100.67 | 162.0167 |
| 7 | 272.22 | **438.1247** | 137.02 | 220.5228 |
| 8 | 355.55 | **572.2445** | 178.96 | 288.0297 |
| 9 | 450.00 | **724.2470** | 226.50 | **364.5377** |
| 10 | 555.55 | **894.1319** | 279.63 | **450.0464** |

Velocity of Particle=85% Velocity of Fluid

| (V=85%*U) | CABOSIL PARTS. | | LATEX PARTICLES | |
|---|---|---|---|---|
| DIAM ($\mu$m) | TIME CONSTANT ($\mu$sec) | TIME RESPONSE ($\mu$sec) | TIME CONSTANT ($\mu$sec) | TIME RESPONSE ($\mu$sec) |
| 1 | 5.55 | 10.540 | 2.80 | 5.3049 |
| 2 | 22.22 | 42.158 | 11.18 | 21.2196 |
| 3 | 50.00 | 94.856 | 25.17 | 47.7442 |
| 4 | 88.89 | 168.633 | 44.74 | 84.8785 |
| 5 | 138.89 | 263.489 | 69.91 | 132.6227 |
| 6 | 200.00 | 379.424 | 100.67 | 190.9768 |
| 7 | 272.22 | 516.438 | 137.02 | 259.9405 |
| 8 | 355.55 | 674.532 | 178.96 | 339.5142 |
| 9 | 450.00 | 853.704 | 226.50 | 429.6977 |
| 10 | 555.55 | 1053.955 | 279.63 | 530.4909 |

Velocity of Particle=90%*Velocity of Fluid

| (V=90%*U) | CABOSIL PARTS. | | LATEX PARTICLES | |
|---|---|---|---|---|
| DIAM ($\mu$m) | TIME CONSTANT ($\mu$sec) | TIME RESPONSE ($\mu$sec) | TIME CONSTANT ($\mu$sec) | TIME RESPONSE ($\mu$sec) |
| 1 | 5.55 | 12.792 | 2.80 | 6.4387 |
| 2 | 22.22 | 51.169 | 11.18 | 25.7548 |
| 3 | 50.00 | 115.129 | 25.17 | 57.9484 |
| 4 | 88.89 | 204.674 | 44.74 | 103.0193 |
| 5 | 138.89 | 319.803 | 69.91 | 160.9677 |
| 6 | 200.00 | 460.517 | 100.67 | 231.1794 |
| 7 | 272.22 | 626.815 | 137.02 | 315.4967 |
| 8 | 355.55 | 818.697 | 178.96 | 412.0774 |
| 9 | 450.00 | 1036.163 | 226.50 | 521.5355 |
| 10 | 555.55 | 1279.214 | 279.63 | 643.8709 |

Velocity of Particle=95% Velocity of Fluid

| (V=95%*U) | CABOSIL PARTS. | | LATEX PARTICLES | |
|---|---|---|---|---|
| DIAM (μm) | TIME CONSTANT (μsec) | TIME RESPONSE (μsec) | TIME CONSTANT (μsec) | TIME RESPONSE (μsec) |
| 1 | 5.55 | 16.643 | 2.80 | 8.3770 |
| 2 | 22.22 | 66.572 | 11.18 | 33.5078 |
| 3 | 50.00 | 149.787 | 25.17 | 75.3926 |
| 4 | 88.89 | 266.287 | 44.74 | 134.0313 |
| 5 | 138.89 | 416.074 | 69.91 | 209.4239 |
| 6 | 200.00 | 599.146 | 100.67 | 301.5704 |
| 7 | 272.22 | 815.505 | 137.02 | 410.4708 |
| 8 | 355.55 | 1065.149 | 178.96 | 536.1251 |
| 9 | 450.00 | 1348.080 | 226.50 | 678.5334 |
| 10 | 555.55 | 1664.296 | 279.63 | 837.6955 |

Velocity of Particle=99%*Velocity of Fluid

| (V=99%*U) | CABOSIL PARTS. | | LATEX PARTICLES | |
|---|---|---|---|---|
| DIAM (μm) | TIME CONSTANT (μsec) | TIME RESPONSE (μsec) | TIME CONSTANT (μsec) | TIME RESPONSE (μsec) |
| 1 | 5.55 | 25.584 | 2.80 | 12.877 |
| 2 | 22.22 | 102.337 | 11.18 | 51.510 |
| 3 | 50.00 | 230.258 | 25.17 | 115.897 |
| 4 | 88.89 | 409.348 | 44.74 | 206.039 |
| 5 | 138.89 | 639.606 | 69.91 | 321.935 |
| 6 | 200.00 | 921.033 | 100.67 | 463.587 |
| 7 | 272.22 | 1253.628 | 137.02 | 630.993 |
| 8 | 355.55 | 1637.392 | 178.96 | 824.154 |
| 9 | 450.00 | 2072.324 | 226.50 | 1043.070 |
| 10 | 555.55 | 2558.425 | 279.63 | 1287.740 |

# REPORT DOCUMENTATION PAGE

Form Approved
OMB No. 0704-0188

Public reporting burden for this collection of information is estimated to average 1 hour per response, including the time for reviewing instructions, searching existing data sources, gathering and maintaining the data needed, and completing and reviewing the collection of information. Send comments regarding this burden estimate or any other aspect of this collection of information, including suggestions for reducing this burden, to Washington Headquarters Services, Directorate for Information Operations and Reports, 1215 Jefferson Davis Highway, Suite 1204, Arlington, VA 22202-4302, and to the Office of Management and Budget, Paperwork Reduction Project (0704-0188), Washington, DC 20503.

| 1. AGENCY USE ONLY (Leave blank) | 2. REPORT DATE | 3. REPORT TYPE AND DATES COVERED |
|---|---|---|
| | May 1994 | Final Contractor Report |

**4. TITLE AND SUBTITLE**

A Qualitative and Quantitative Laser-Based Computer-Aided Flow Visualization Method

**5. FUNDING NUMBERS**

WU–505–62–52
NCC3–93
NCC3–165

**6. AUTHOR(S)**

Victor A. Canacci and M. Jack Braun

**7. PERFORMING ORGANIZATION NAME(S) AND ADDRESS(ES)**

University of Akron
Department of Mechanical Engineering
Akron, Ohio 44325

**8. PERFORMING ORGANIZATION REPORT NUMBER**

E–8692

**9. SPONSORING/MONITORING AGENCY NAME(S) AND ADDRESS(ES)**

National Aeronautics and Space Administration
Lewis Research Center
Cleveland, Ohio 44135–3191

**10. SPONSORING/MONITORING AGENCY REPORT NUMBER**

NASA CR–195300

**11. SUPPLEMENTARY NOTES**

This report was submitted by Victor A. Canacci as a thesis in partial fulfillment of the requirements for the degree Master of Science in Mechanical Engineering to The University of Akron in 1992. Project Manager, Steven A. Hippensteele, Internal Fluid Mechanics Division, organization code 2630, NASA Lewis Research Center, (216) 433–5897.

**12a. DISTRIBUTION/AVAILABILITY STATEMENT**

Unclassified - Unlimited
Subject Category 02

**12b. DISTRIBUTION CODE**

**13. ABSTRACT** ***(Maximum 200 words)***

The experimental approach presented here offers a nonintrusive, qualitative and quantitative evaluation of full field flow patterns applicable in various geometries in a variety of fluids. This Full Flow Field Tracking (FFFT) Particle Image Velocimetry (PIV) technique, by means of particle tracers illuminated by a laser light sheet, offers an alternative to Laser Doppler Velocimetry (LDV), and intrusive systems such as Hot Wire/Film Anemometry. The method makes obtainable the flow patterns, and allows quantitative determination of the velocities, accelerations, and mass flows of an entire flow field. The method uses a computer based digitizing system attached through an imaging board to a low luminosity camera. A customized optical train allows the system to become a long distance microscope (LDM), allowing magnifications of areas of interest ranging up to 100 times. Presented in addition to the method itself, are studies in which the flow patterns and velocities were observed and evaluated in three distinct geometries, with three different working fluids. The first study involved pressure and flow analysis of a brush seal in oil. The next application involved studying the velocity and flow patterns in a cowl lip cooling passage of an air breathing aircraft engine using water as the working fluid. Finally, the method was extended to a study in air to examine the flows in a staggered pin arrangement located on one side of a branched duct.

**14. SUBJECT TERMS**

Flow visualization; PIV; Pin fins; Bruh seals; Cowl lips; Seed particles

**15. NUMBER OF PAGES**
205

**16. PRICE CODE**
A10

| 17. SECURITY CLASSIFICATION OF REPORT | 18. SECURITY CLASSIFICATION OF THIS PAGE | 19. SECURITY CLASSIFICATION OF ABSTRACT | 20. LIMITATION OF ABSTRACT |
|---|---|---|---|
| Unclassified | Unclassified | Unclassified | |